DESIGN OF A HIGHLY-EXTENSIBLE PNEUMATIC ACTUATOR FOR SOFT ROBOTIC APPLICATIONS

by

Bora Alp Baydere

B.S., Mechanical Engineering, Stanford University, 2014

Submitted to the Institute for Graduate Studies in
Science and Engineering in partial fulfillment of
the requirements for the degree of
Master of Science

Graduate Program in Mechanical Engineering

Boğaziçi University

2019

ACKNOWLEDGEMENTS

It would not be possible to complete my thesis without the help of my advisor, Prof. Evren Samur. I sincerely thank him for his valuable guidance and support. I would also like to thank Prof. Çetin Yılmaz and Prof. Onur Özcan who accepted to be jury members of my master's thesis despite their busy schedule.

I am especially grateful to my friends in the RoboCol project for their continued help throughout my thesis, including Şeref for preparing the necessary electronic hardware and control system of the final robot, Timur for his ideas and help on manufacturing, and Cem for his contributions to the design. I would also like to thank my friends from the Haptics and Robotics lab, Taylan and Onur for their help and insights on design, Kübra for her help with the workspace experiments, and Serhat and Burcu for their support and camaraderie.

Finally, my special thanks go to my family for their everlasting love and support in every decision I have made.

This project is supported by the Scientific and Technological Research Council of Turkey (TÜBITAK #115E717).

ABSTRACT

DESIGN OF A HIGHLY-EXTENSIBLE PNEUMATIC ACTUATOR FOR SOFT ROBOTIC APPLICATIONS

Soft continuum robots have been an expanding research topic due to their inherent compliance and flexibility. However, most of the conventional continuum robots still lack the ability to significantly change size and length. In this study, a novel highly-extensible pneumatic actuator is developed that can help overcome the limited extension capabilities of soft continuum robots. The main advantage of the actuator is that extension is directly controlled by an external motor, independent from pressure. First, models are given to calculate actuator force, speed and stiffness. A prototype of the actuator is manufactured, and experiments are performed to validate the model. Second, a soft robot is designed using the proposed actuator that can achieve controlled extension and active steering of the tip. Two prototypes are developed; one that can move on a plane and one that can move in 3D space. Finally, the robots are tested to explore their mechanical characteristics and navigation capabilities in free space, through obstacles and in enclosed environments. The results indicate that multiple actuators can be used to successfully navigate a tip-extending soft continuum robot. Speed test results show that controlling actuator speed independent from pressure is possible with the proposed actuator.

ÖZET

YUMUŞAK ROBOT UYGULAMALARI İÇİN YÜKSEK MİKTARDA UZAYABİLEN BİR PNÖMATİK EYLEYİCİ TASARIMI

Farklı ortamlara uyum sağlayabilme özellikleri nedeniyle yumuşak sürem robotların kullanımı gittikçe yaygınlaşmaktadır. Ancak, bu avantajlarına rağmen geliştirilen yumuşak sürem robotların büyük bir çoğunluğu yüksek miktarda uzama ya da büyüme kabiliyetine sahip değildir. Bu çalışmada, yumuşak robotlarda kullanılabilecek uzayabilen pnömatik bir eyleyici tasarımı sunulmuştur. Tasarlanan eyleyicinin özgün yönü, eyleyici hızının basınçtan bağımsız olarak, harici motorlar tarafından kontrol edilmesidir. Öncelikle eyleyici kuvveti, hız ve katılığı hesaplamak için modeller sunulmuştur. Eyleyici prototipi üretilmiş, üretilen prototip üzerinde performans testleri yapılmış ve sonuçlar model ile karşılaştırılmıştır. Daha sonra tasarlanan eyleyici kullanılarak biri düzlemsel yüzey, diğeri ise serbest uzayda hareket edebilen iki yumuşak robot geliştirilmiştir. Son olarak, robotlar mekanik özelliklerini belirlemek amacıyla belirli testlere tabi tutulmuştur. Aynı zamanda robotlar serbest uzayda, engeller arasında ve kapalı alanlarda çeşitli hareket testlerine tabi tutulmuştur. Sonuçlar tasarlanan eyleyicinin uçtan uzayan yumuşak sürem bir robotta kullanılabileceğini göstermiştir. Eyleyici hızının basınçtan bağımsız olarak kontrol edilebildiği doğrulanmıştır.

TABLE OF CONTENTS

LIST OF FIGURES

LIST OF TABLES

LIST OF SYMBOLS

A_o	Cross-sectional area of the tubing before inflation
E	Elastic (Young's) modulus of the tubing material in MPa
E_{rel}	Relative positioning error of the robot in percentage (%)
F_b	Critical bending load of the tubing
F_c	Critical buckling load of the tubing
F_f	Friction force acting at the pinch point between the rollers
F_{FS}	Actuator output force with full slip at the roller-tubing interface
F_m	Tension force acting on the roller due to the slack section being pulled by the motor
F_{MS}	Actuator output force with mixed slip at the roller-tubing interface
F_{NS}	Actuator output force with no slip at the roller-tubing interface
F_P	Resultant pressure force acting on the roller surface
F_t	Tension force acting on the roller in tangential direction due to axial stress on the inflated tubing
F_x	Reaction force acting on the roller in the x-direction
F_y	Reaction force acting on the roller in the y-direction
G	Shear modulus of the tubing material in MPa
I	Second moment of area of the tubing
K_{max}	Maximum curvature of the robot backbone
l_o	Natural length of the tubing before inflation
L	Current length of the tubing in mm
L_b	Current length of the robot backbone in mm
L_{max}	Maximum length of the robot backbone in mm
L_{min}	Minimum length of the robot backbone in mm
P	Pressure of the tubing in MPa
r	Radius of the roller in mm
r_{sp}	Radius of the spool in mm

R	Current inner radius of the rubber tubing layer dependent on pressure in mm
R_{min}	Minimum radius of curvature of the robot backbone in mm
R_n	Inner radius of the outer tubing layer in mm
R_o	Natural inner radius of the rubber tubing layer in mm
t	Current wall thickness of the rubber tubing layer dependent on pressure in mm
t_n	Thickness of the outer tubing layer in mm
t_o	Natural thickness of the rubber tubing layer in mm
v_{tip}	Velocity of the actuator tip in mm/s
w	Speed of the motor in rpm
x	Axis on the pinch-roller mechanism along the tubing neutral axis
y	Axis on the pinch-roller mechanism passing through the roller centers
X	Axis of fixed frame of the soft robot
Y	Axis of fixed frame of the soft robot
Z	Axis of fixed frame of the soft robot
α	Angle between the pinch point and the point at which slack section leaves the roller surface
δ	Deflection of the tubing in mm
κ	Angle of the continuous arc formed at the intersection of the roller and tubing surfaces
μ	Friction coefficient between the tubing outer layer and roller surface
ν	Poisson's ratio
ω	Angle of rotation of inflated beam around the z-axis in rad
σ_o	Tensile strength of the tubing material in MPa

LIST OF ACRONYMS/ABBREVIATIONS

2D	Two Dimensional
3D	Three Dimensional
ACU	Air Control Unit
CAD	Computer-Aided Design
CC	Constant Curvature
DoF	Degrees of Freedom
FU	Feed Unit
FPGA	Field Programmable Gate Array
FS	Full Slip
FDM	Fused Deposition Modeling
HDPE	High Density Polyethylene
HSA	Hollow Shaft Actuator
IPAM	Inverse Pneumatic Artificial Muscle
L	Latex Rubber
LDPE	Low Density Polyethylene
MRI	Magnetic Resonance Imaging
MAE	Mean Absolute Error
MS	Mixed Slip
NS	No Slip
OD	Outer Diameter
PA 12	Polyamide 12
PAM	Pneumatic Artificial Muscle
PB	Pebax
PEL	Pellethane
PLA	Polylactide
PRA	Pneumatic Reel Actuator
PTFE	Polytetrafluoroethylene
PVC	Polyvinyl Chloride

PWM	Pulse Width Modulation
RTOS	Real-Time Operation System
RMSE	Root Mean Square Error
SLS	Selective Laser Sintering
sPAM	Series Pneumatic Artificial Muscle
SMA	Shape Memory Alloy
SPA	Soft Pneumatic Actuator
UI	User Interface

1. INTRODUCTION

This chapter provides background information for the research presented in this thesis. In addition, the motivation behind this study and its main aims are explained.

1.1. Background

1.1.1. Soft Robots

Rigidity in robotics has long been associated with high precision and repeatability which has contributed to the prevalence of stiff robots with discrete, rigid links in the industry [1]. However, as the field of robotics continues to expand beyond industrial automation and into the domains of healthcare, human assistance and field exploration, robots must become increasingly less rigid and specialized, and instead approach the versatility of materials and organisms found in nature [2]. This requirement for flexibility; versatility and lighter weight has made soft robots a significant research interest in recent years.

Although various definitions have been given to soft robots based on material, geometry and method of locomotion, the one given by Cianchetti *et al.* is generally acknowledged as the most inclusive by the research community. According to Cianchetti *et al.* soft robots are robots that "can actively interact with the environment and can undergo large deformations relying on inherent or structural compliance" [3]. In contrast to conventional robots, soft robots contain little to no rigid material and are characterized by their continuously deformable nature (see Figure 1.1) [4]. This means they have desirable properties such as compliance to the environment ingrained in their mechanical structures.

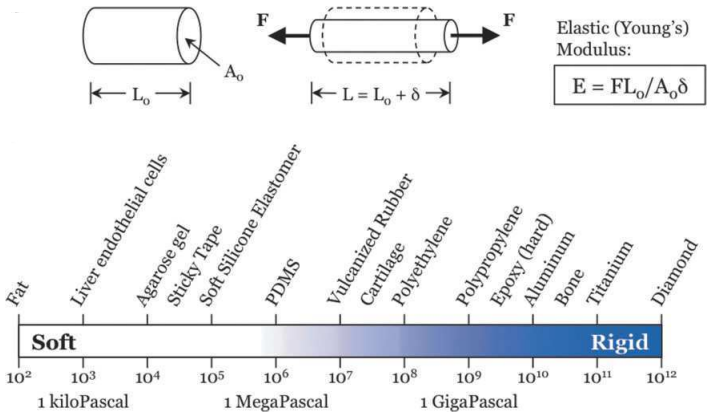

Figure 1.1. Soft robots are composed primarily of materials that have an elastic (Young's) modulus of less than around 1 gigapascal (GPa). Reprinted from [2].

1.1.2. Continuum Robots

Another category of robots that closely intersects the realm of soft robots is *continuum robots*. In its most basic definition, continuum robots are invertebrate actuatable structures whose constitutive material forms continuous tangent vectors. Conceptually, continuum robots are hyper-redundant robots taken to the extreme, with number of joints tending to infinity and their link lengths tending to zero [5]. They consist of a *backbone* that can bend continuously along its length via elastic deformation and produce motion by generating smooth curves [6]. Similar to soft robots, continuum robots are usually inspired by biological structures such as the body of a snake [7] or tentacles of an octopus (see Figure 1.2) [8].

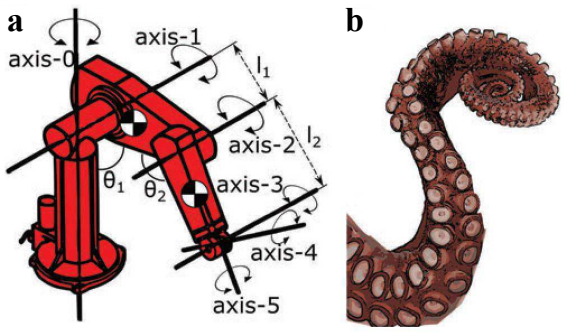

Figure 1.2. (a) A simple rigid-bodied system (PUMA robot) and (b) soft continuum system. Reprinted from [9].

Since by definition, the term *continuum* pertains to the shape of the robot while *soft* pertains to its material, not all continuum robots can be categorized as soft robots and vice versa. Hence, these two terms are not interchangeable. Numerous continuum robot designs have been proposed where the main backbone comprises hard components such as shells, springs and cables, including remotely tendon-driven robots [10], concentric tube (or active cannula) robots [11] and certain pneumatically actuated robots [5, 7]. If a robot exhibits both continuum characteristics and is primarily made of soft, flexible material, it can be categorized as a soft continuum robot. Some well-known examples of soft continuum robots with pneumatic actuators are the OctArm [8], the Bionic Handling Assistant [12] and the STIFF-FLOP manipulator [13].

1.1.3. Design Flow for Soft Robots

The design flow for soft robots differs greatly from that of rigid robots because soft robots have elements that cross multiple domains and are often made using materials capable of very large deformations. All soft robots convert stored energy into task-oriented work using systems that integrate complex pneumatic, hydraulic, chemical, mechanical or electrical actuators. This complexity makes it difficult to analyze the overall system and identify main sources of energy loss.

Rigid-link robots are built using standardized and well-defined components. They can be controlled through a predictive model, which is usually based on defining the Jacobian of the system and applying well-established methodologies using inverse kinematics. For this reason, modeling and simulation is paramount for rigid-link robots, whereas testing the physical robot is usually the last step in the design flow. In stark contrast, soft robotic systems are often built using complex and multi-domain blocks that are not completely characterized. Due to the complexity of simulating soft actuators and their strong dependence on interaction with the environment, building and testing remain as key iterations in the design loop for soft robots (see Figure 1.3).

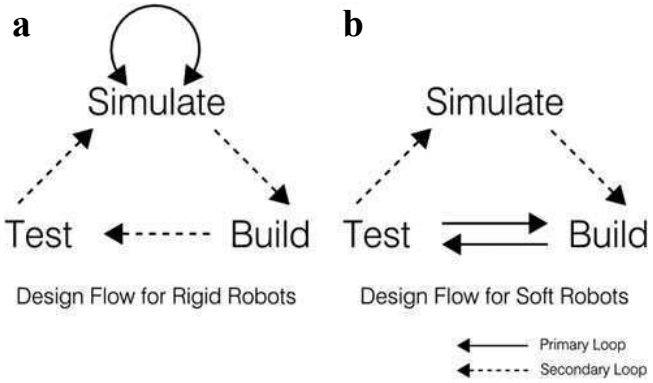

Figure 1.3. Typical design flow for (a) rigid robots and (b) soft robots. Reprinted from [9].

The main elements for modeling of soft structural elements and actuators are (a) characterizing soft robots in terms of energy transformation and calculating sources of energy loss and (b) analyzing, modeling and simulating the whole-body mechanics of large-scale deformations. These remain as the most challenging steps in the design loop [9].

1.2. Motivation

Soft continuum robots are advantageous in the sense that they offer little resistance to compressive forces, and hence can conform to obstacles in the environment due to their deformable backbones [14]. Rigid robots do not have this advantage as they must track their environment and change shape accordingly. This property has made soft continuum robots an ideal candidate for exploratory operations in unstructured, substantially-long and narrow environments especially in the medical field as well as for disaster-relief and pipe inspection [2]. However, a major issue with many soft continuum robots is that they introduce a new body into the environment without a substantial change in size or length which leads to challenges especially in control [14]. In particular, the lack of position and speed feedback due to the strains on the robot body, and contact with the environment can drastically affect the robot's motion and dynamics [9].

Most soft continuum robots in literature are limited in extension by axial strain capability of the backbone material. In addition, since both radial and axial strain of the backbone are dependent on the actuation pressure, it remains a challenge to limit radial forces while retaining high axial elastic strains. This is especially crucial for medical applications such as minimally invasive surgery, where contact forces with the environment must be minimized. The typical axial elastic strains attained in the literature for soft pneumatic actuators (SPAs) are in the order of 40%, 200%, 300% and up to 450% [13,15–17]. However, axial strains surpassing 1000% may be necessary in cases where the robot must navigate through substantially long and narrow environments, which remains an open challenge for locally actuated soft continuum robots.

Without the ability to extend continuously from the tip, the workspace of a soft robot remains constrained by its elastic structure (see Figure 1.4). Therefore, developing an actuation mechanism that can be used to extend the robot backbone from the tip with increased stability during motion and diminished effects of friction would be exceptionally useful for navigation in such environments.

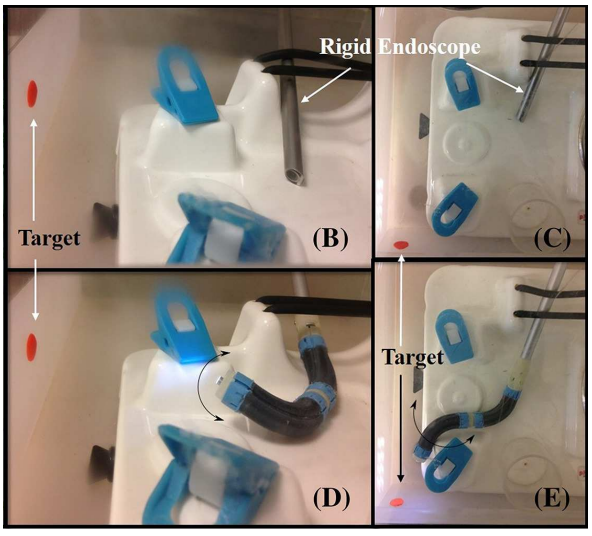

Figure 1.4. A highly dexterous soft continuum robot for laparoscopic surgery. Although the robot provides significant improvement in terms of maneuverability over the rigid endoscope, it still has to be inserted manually to the target site due to a lack of extension capability. Reprinted from [18].

1.3. Aims of the Study

In this study, a highly extensible pneumatic actuator is proposed that can help overcome the limited extension capabilities of soft continuum robots. Multiple actuators are then incorporated in a soft robot that can achieve controlled extension and active steering of the tip in free space and through closed, cluttered environments. To this end, the study can be considered to have two main aims and is therefore divided into two main sections to ease presentation.

Aim 1: Design, modeling and development of a highly-extensible actuator for proof of concept. The developed prototype is used to evaluate mechanical characteristics of the actuator and verify the model.

Aim 2: Design, development and testing of a working soft continuum robot using the proposed actuator. Two prototypes are developed, a preliminary prototype with two actuators in parallel that can achieve planar motion, and a final prototype with three actuators that can achieve motion in three-dimensional (3D) space.

1.4. The Pinch-Roller Drive

The proposed actuator uses a simple drive principle called the "pinch-roller drive" shown in Figure 1.5. The basic pinch-roller drive consists of two frictionless rollers anchored on a moving base. A thin-walled inflatable tubing is squeezed between the rollers, and the uninflated part, called the slack section, is connected to a motor from the other end. When the tubing is pressurized, the buildup of pressure energy leads to a cumulative axial force applied on the roller surface in x-direction. Extension is achieved by releasing the slack section using the motor. Conversely, contraction is achieved by retracting the slack section using the motor while releasing the air in the tubing through an exhaust valve.

Conceptually, the mechanism extends by adding more tubing material at the tip with minimal axial and radial strain, depending on the chosen tubing material. This makes it possible to reach extension ratios much higher than the ones given in Section 1.2. Although there are some actuators similar to the pinch-roller drive (see Section 2.3), the main advantage of this design is the decoupling of tubing pressure and actuation. While tubing pressure gives stiffness to the actuator and provides the driving force, the motor is used to control the speed of extension or contraction. Another advantage is that the extension ratio can be modified depending on the application simply by changing tubing length. Since tubing material is stored on the spool and not on the actuator itself, increasing tubing length does not affect the size or weight of the actuator.

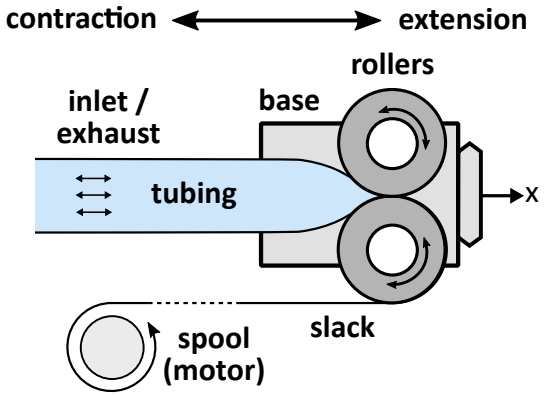

Figure 1.5. Diagram of the proposed actuator using the pinch-roller drive. The main advantage of this design is the decoupling of tubing pressure and extension/contraction speed.

2. LITERATURE REVIEW

In this chapter, actuation methods commonly used in soft continuum robots are explained with examples from literature. Then, different soft pneumatic actuator designs in literature are presented. Finally, actuators with high extension capabilities similar to the pinch-roller drive are listed, and compared to the proposed actuator.

2.1. Actuation Methods in Continuum Robots

Actuators in continuum robots are categorized as either intrinsic or extrinsic depending on where the actuation occurs. The actuator is labeled *intrinsic* if actuation occurs within the moving manipulator structure, whereas it is labeled *extrinsic* if actuation occurs outside of the main structure with forces transmitted to the structure through some mechanical transmission [19].

To date, various types of actuators have been demonstrated for use in continuum robots. Transmission mechanisms for extrinsic actuation include tendon/cable driven mechanisms and multi-backbone structures such as concentric-tube transmissions that are driven by axial rotations and translations of the tube bases. Intrinsic actuation strategies include hydraulic chambers, soft pneumatic actuators (SPAs), shape memory polymers, shape memory alloy (SMA) actuators, fluidic fiber-reinforced elastomers, embedded micro-motors and chemical reaction based actuators [19]. Robotic catheters actuated by magnetic fields generated through magnetic resonance imaging (MRI) machine [20] have also been developed. These actuators can be considered intrinsic as power conversion occurs within the embedded magnets on the manipulator. There have also been cases where intrinsic pneumatic actuation was combined with extrinsically actuated structures to induce active stiffening of the robot backbone through particle jamming [21].

Although material selection in these actuators is not critical for conventional continuum robots, it is very important for soft continuum robots. Actuators used in soft continuum robots are mainly made of compliant materials such as silicones, soft polymers and hydrogels [22–24]. Among the actuation methods listed above, pneumatic actuators are encountered more frequently in soft robots due to their inherent compliance, ease of manufacturing, high fabrication efficiency, low cost and weight [4].

2.2. Soft Pneumatic Actuators

SPAs are a category of intrinsically compliant and readily manufacturable actuators that are widely used in soft robotics. Although the precise construction of SPAs can vary, they are commonly found in the form of slender, thin-walled and hollow structures externally constrained by inextensible fibers. The actuators are activated by applying positive relative pressure to the hollow internal cavity, and can be designed to produce linear, bending, torsion forces and even combinations thereof through modifying the approach angles of the constraining fibers relative to the direction of motion [25].

The most common type of SPAs are Pneumatic Artificial Muscles (PAMs), which follow the same actuation principles mentioned above. The McKibben muscle, one of the oldest variants of PAMs has been widely adopted in robotics and automation due to its high force to weight ratio, high speeds and compliance. It features an inflatable elastomer core surrounded by braided fiber outer sheath which expands radially and contracts axially when activated (see Figure 2.1). Despite their widespread use, PAMs are only effective in tension, and are limited to less than 100% axial strain [1] [26].

[1] Axial strain is defined as the change in length compared to the initial length $\left(\frac{\Delta L}{L_o}\right)$ expressed in percent form (i.e. $\epsilon = 1 \Rightarrow 100\%$).

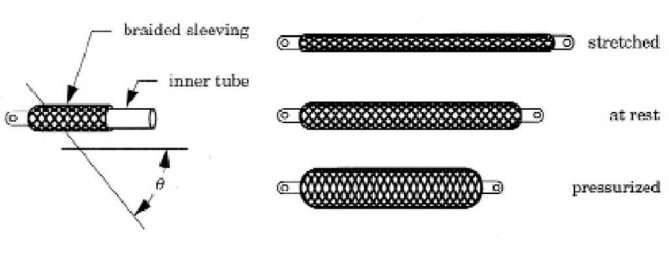

Figure 2.1. Working principle of a traditional McKibben muscle. Reprinted from [26].

The Inverse Pneumatic Artificial Muscle (IPAM) has recently been proposed as an alternative to PAMs. The defining feature of the IPAM is that it extends with positive pressure gradient instead of contracting. The IPAM claims a 300% axial strain while maintaining advantages of the conventional PAM [16]. Nevertheless, like the PAM, it is effective in tension and does not offer significant improvements in extension ratio [2] .

Another novel variant of the traditional PAM design is the Series Pneumatic Artificial Muscle (sPAM), which consists of multiple PAMs attached in series [27]. It is made entirely of thin-walled, low-density tubing and can be fabricated from thin sheets of polyethylene requiring no casting or molding. A large portion of the sPAM inflates through unwrinkling and unfolding of its membrane rather than stretching, resulting in zero axial stress during inflation. By operating PAMs in series, the design can technically achieve extension ratios higher than the IPAM. However, due to its light weight and low stiffness, it has low load bearing capabilities. The reported maximum weight that the robot can lift successfully is in the range of 200 grams.

Despite their advantages, providing accurate position and speed control with SPAs is challenging due to the coupling of chamber pressure and actuator motion. Another major issue with many SPAs is that their extension ratio is limited by axial strain capability of the material used which also leads to low repeatability due to fatigue. They are usually limited to less than 450% axial strain [17].

[2]Extension ratio is defined as the ratio between the final length and the initial length for a system that may extend through deformation or by other means. It is given in the form of $L : L_o$ where L is the final length and L_o is the initial length.

2.3. Highly Extensible Actuators

Several highly extensible actuators can be encountered in literature that can surpass the limited extension capabilities of SPAs. Most of these actuators extend by different mechanisms that either push the actuator body forward or extend from the tip.

Reaching very high extension ratios while keeping the actuator housing compact is a challenge even for commercial linear actuators. Although not compliant, there are several highly extensible linear actuators in literature. One such example is the *Spiralift*, which is used as a compact lifting system for heavy platforms [28]. It consists of a rotary mechanism that guides a spiral band along a helical path with interlocking teeth and is reportedly capable of reaching extension ratios of 12.5:1. A conceptually similar actuator is the *Spiral Zipper*, which builds a circular column from a single sheet of plastic using a single motor and planetary gear [29]. Nevertheless, none of these mechanisms can be used in a continuum or soft robot due to their rigidity.

Some compliant mechanisms similar to the proposed pinch-roller drive can be encountered in literature. A rudimentary example is the party-blower (see Figure 2.2), which is a common party item comprised of a paper tube rolled into a coil that quickly unrolls when air is blown into it. It can reach very high extension speeds while retaining stiffness of the main body.

Figure 2.2. A party-blower, also called a party-horn.

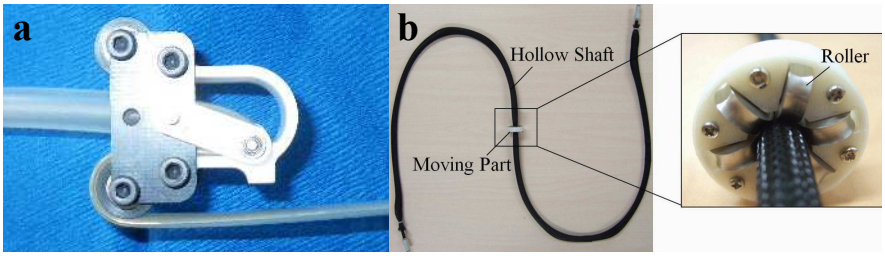

Figure 2.3. (a) Λ-Drive [30] and (b) the Hollow Shaft Actuator [31]

The Hollow Shaft Actuator (HSA) and the Λ-Drive utilize actuation mechanisms comparable to the pinch-roller drive [30,31]. However, these actuators are not suitable for motion with two or more degrees-of-freedom (DoF) since both can only move on a pre-defined shaft (see Figure 2.3). These mechanisms were designed mainly for search and rescue applications.

The Pneumatic Reel Actuator (PRA) is a recent design that consists of a roller with a pair of ball bearings and spiral torsion springs (see Figure 2.4) [32]. When the actuator is unpressurized, the torsion springs inside the reel retract the tubing freely. When pressure is applied to the opposite end of the tubing, the flexible membrane forms a thin-walled cylindrical beam with increased stiffness and pulls more of the tubing out of the reel, lengthening the actuator and storing energy in the torsion springs. This actuator can reportedly reach an extension ratio of 16.8:1. However, to reach higher extension ratios the reel diameter must be increased which is undesirable in applications where size and weight of the end-effector must be minimal. Also, in its current form, the PRA has one DoF and is too stiff to be used in a soft continuum robot.

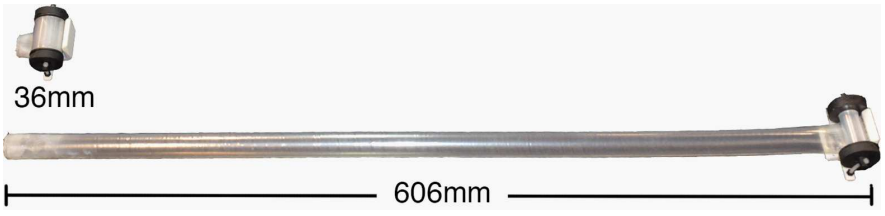

Figure 2.4. The Pneumatic Reel Actuator (PRA). Reprinted from [32]

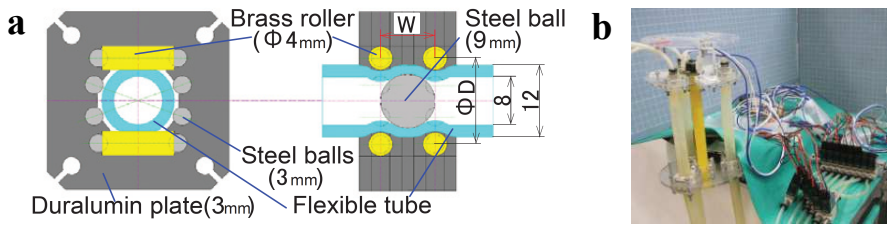

Figure 2.5. (a) The rod-less type flexible pneumatic actuator and (b) its application to a continuum robot arm. Reprinted from [33].

A similar drive mechanism with a rod-less type flexible pneumatic cylinder and an inner steel ball as a cylinder head has been developed (see Figure 2.5) and used in a continuum robot arm to realize controlled motion in 3D space [33]. The mechanism uses pressurized thick tubings that extend from the base to actuate the robot arm and the amount of extension is controlled by changing tubing pressure. A major drawback of this design is that it requires an air inlet at the tip and the tubings are fed from the base of the robot as opposed to extending from the tip. The design is also not suitable for a soft robotic application due to the high rigidity of the thick tubings.

2.4. Growth Based Extension in Soft Continuum Robots

Growth is a pioneering paradigm that has very recently been introduced in the literature as an alternative method to achieve very high extension ratios in continuum robots. According to a study aiming to define types of growing robots, growth based extension has two key properties: (1) the body evolves by addition of material at the tip (tip-based extension) and (2) locomotion is performed by growing the body and not by an external component [34]. Using actuators that extend from the tip instead of pushing the whole body forward leads to higher dexterity, more stable actuation and increased resistance to environmental disturbances due to forward drive of the robot body [35, 36].

In 2017, Dehghani *et al.* developed an extensible self-steering robot with expandable balloons for colonoscopy application [37]. This soft continuum robot moves through a combination of axial strain and tip-based extension. Yarbasi and Samur also developed a similar system with added steering ability in 2-DoF [38] which can reach an extension ratio of 20:1 at peak length (Figure 2.6a).

A promising example of tip-based extension is the vine robot [36] which has been developed very recently (Figure 2.6b). This robot, designed by Hawkes *et al.* has a main backbone made of a thin polyethylene membrane that is pinched at the end with a cone-shaped fastener. It achieves lengthening at the tip through eversion of the membrane driven by internal pressure and its extension ratio is only limited by the amount of membrane material stored at the base. The robot can move on a predetermined path, but it lacks the ability to actively steer its tip during extension.

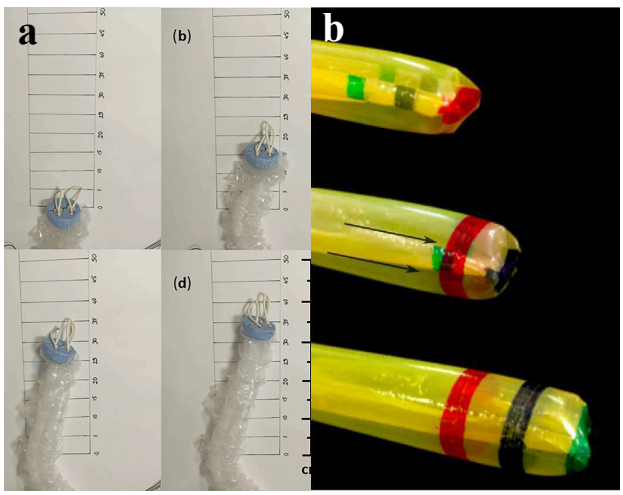

Figure 2.6. (a) The soft continuum robot developed by Yarbasi and Samur [38] and (b) the vine robot developed by Hawkes *et al.* [36]

2.5. Originality of the Proposed Actuator

Although these actuation methods using tip based extension can surpass the extension ratios achieved by traditional SPAs, actuator motion is still dependent on chamber pressure in all of these designs. Providing accurate control of tip position and extension speed is challenging due to the nonlinear relationship between pressure and extension speed. A closed-loop control system with position sensors and sophisticated pressure regulators with fast response time is required in these systems to control the robot with sufficient accuracy. A major advantage of the proposed actuator, besides the ability to provide active steering by using multiple actuators, is the decoupling of pressure and extension/contraction. This allows us to control extension speed independent from pressure without the need for external sensors.

Despite its advantages, the proposed actuator also has certain shortcomings. For instance, due to the movement of the slack section the actuator body does not have zero relative motion with respect to the environment which is a prominent feature of growth-based extension. This leads to sliding friction which can be undesirable in certain applications. Moreover, although extension is actuated intrinsically at the tip, contraction is actuated extrinsically by applying a tension force through the slack section. For this reason, controlled contraction is possible at short strokes or when curvature of the actuator body is low, but it can be problematic at long strokes due to the changing direction of the tension force. A detailed comparison of the pinch-roller drive with the aforementioned actuators is given in Table 2.1.

Table 2.1. The proposed actuator compared with similar pneumatic actuators.

Actuator	**Decoupled pressure**	**Extension from the tip**	**Compact tip**	**Soft body**	**No sliding friction**	**Long stroke contraction**	**Max DoF**
PRA [32]	×	✓	×	×	✓	✓	1
Rod-less type [33]	×	×	×	×	×	✓	3
Dehghani *et al.* [37]	×	✓	×	✓	×	×	1
Yarbasi and Samur [38]	×	✓	×	✓	×	×	2
Hawkes *et al.* [36]	×	✓	✓	✓	✓	×	2
Pinch-roller	✓	✓	✓	✓	×	×	3

3. DESIGN OF THE ACTUATOR

As explained in Section 1.3, this study is divided into two main parts. This is the first part that explains the design and development of the proposed highly extensible actuator. First, the working principle of the actuator is explained. Then, a physical model is proposed that can be used to characterize the effect of design parameters on applied force, speed, durability and stiffness. Second, mechanical design of the prototype and the experimental setup prepared to test the actuator are explained in detail. Finally, experimental results are given to verify the model and finalize the design parameters.

3.1. Working Principle

The working principle of the actuator was described in Section 1.4. To reiterate, the actuator uses a drive mechanism called the "pinch-roller drive" which is demonstrated in Figure 3.1a. In its simplest form, the pinch-roller drive consists of two frictionless rollers anchored on a base. A thin-walled inflatable tubing is squeezed between the rollers, and is connected onto a spool that is attached to a motor from the other end. Inflation of the thin-walled tubing leads to a buildup of pressure on the roller surface, which is translated into rolling kinetic energy of the rollers (plus friction and heat losses) when the slack portion is released by the motor. This causes the slack to be pulled through the rollers, adding more material to the inflated tubing at the tip. Subsequent inflation of the slack section propels the base forward (see Figure 3.1b). Contraction is achieved through controlled reduction of tubing pressure using an exhaust valve while the motor pulls back the slack section (see Figure 3.1c). Controlling the tubing pressure during contraction is crucial as it allows the tubing to remain stiff and prevents local buckling.

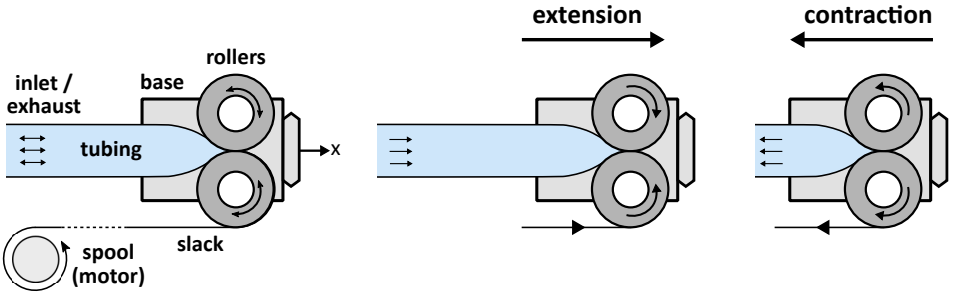

Figure 3.1. (a) Single pinch-roller drive. (b) Extension by releasing more tubing material at the tip while keeping tubing pressure constant and (c) contraction by retracting the tubing while reducing tubing pressure through the exhaust valve.

3.2. Modeling and Simulation

The pinch-roller drive has a working principle that is different from that of conventional SPAs. In this section, the relationship between tubing pressure and actuator force is determined using a force balance at the roller surface for a single pinch-roller drive. Also, several equations are given that can be used to estimate burst pressure, critical bending and buckling forces for any tubing.

3.2.1. Force

The pinch-roller can be modeled as a quasi-static force equilibrium both at rest state and during controlled motion assuming the slack section is released slowly at constant speed. Taking a cut along the xy-plane of the tubing as shown in Figure 3.2a, we can calculate the external forces F_x and F_y acting on the roller in x and y directions respectively using a free body diagram very similar to the one used by Wakana *et al.* [31]. To simplify the model, we assume that the tubing outer layer forms a continuous arc defined by an angle κ at the roller surface as shown in Figure 3.2b.

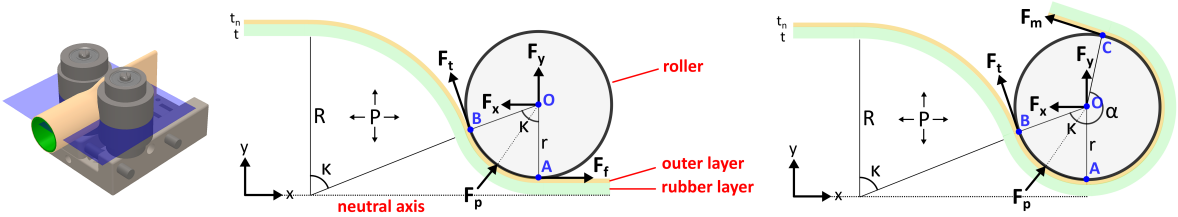

(a) **(b)** **(c)**

Figure 3.2. (a) Cross section of the pinch-roller along the xy-plane. (b) Forces applied on the roller at static equilibrium when the slack section is free (rest state), and (c) when the slack section is pulled by the motor (controlled state) [39].

We consider two states of static equilibrium, one is the *rest state* when the pinch-roller base is fixed and slack section of the tubing is free (Figure 3.2b) and the other one is the *controlled state* when the slack section is connected to the motor, and the pinch-roller is either at rest or is moving at a constant speed (Figure 3.2c).

In both states, forces acting on the rollers by the inflated tubing are the same. Resultant force F_p due to tubing pressure at the roller surface is applied at a point between A and B. At point B, a tension force F_t acts on the rollers in tangential direction due to axial stress on the inflated tubing. In the rest state, a tension force F_f due to friction acts at the pinch point A to counteract F_t. This force is replaced by the tension force F_m in the controlled state which acts at point C. This is the point where the slack section leaves the roller surface.

If we assume friction is large enough that no slipping occurs at the contact surface, forces F_f and F_m will be equal to F_t due to moment balance about the z-axis at point O. We call this the "no slip (NS) condition". The other extreme is the "full slip (FS) condition" which can happen if the roller does not rotate freely and the tubing slides on the roller surface as a result. If full slip occurs (i.e. the tubing slides on the roller), these forces can instead be calculated using the belt friction equation. In this case, the friction coefficient (μ) between the outer layer and the roller surface must be known. The equilibrium equations for both states can be seen below.

Rest state: Controlled state:

$$x: \ F_t \ cos\kappa - F_{px} - F_f + F_x = 0 \qquad x: \ F_t \ cos\kappa - F_{px} - F_m \ cos\alpha + F_x = 0 \tag{3.1}$$

$$y: \ F_t \ sin\kappa + F_{py} + F_y = 0 \qquad y: \ F_t \ sin\kappa + F_{py} + F_m \ sin\alpha + F_y = 0 \tag{3.2}$$

$$z: \ F_f = \begin{cases} F_t \\ F_t \ e^{-\mu\kappa} \end{cases} \qquad z: \ F_m = \begin{cases} F_t & \text{(NS)} \\ F_t \ e^{-\mu(\alpha+\kappa)} & \text{(FS)} \end{cases} \tag{3.3}$$

Using Equations 3.1, 3.2 and 3.3, we can obtain expressions for the reaction forces on the roller (F_x and F_y) for both conditions.

Rest state: Controlled state:

$$F_x = \begin{cases} F_t \ \left(1 - cos\kappa\right) + F_{px} \\ F_t \ \left(e^{-\mu\kappa} - cos\kappa\right) + F_{px} \end{cases} \qquad F_x = \begin{cases} F_t \ \left(cos\alpha - cos\kappa\right) + F_{px} & \text{(NS)} \\ F_t \ \left(cos\alpha \ e^{-\mu(\alpha+\kappa)} - cos\kappa\right) + F_{px} & \text{(FS)} \end{cases} \tag{3.4}$$

$$F_y = \begin{cases} -(F_t \ sin\kappa + F_{py}) \\ -(F_t \ sin\kappa + F_{py}) \end{cases} \qquad F_y = \begin{cases} F_t \ \left(sin\alpha + sin\kappa\right) + F_{py} & \text{(NS)} \\ F_t \ \left(sin\alpha \ e^{-\mu(\alpha+\kappa)} + sin\kappa\right) + F_{py} & \text{(FS)} \end{cases} \tag{3.5}$$

The angle κ can be expressed as:

$$\kappa = \ cos^{-1}\frac{r_t}{R + r_t} \tag{3.6}$$

where r_t is the minimum distance from point O to the tubing neutral axis expressed as $r_t = \ r + t + t_n$. We can assume that the tubing does not deform axially ($\epsilon_x = 0$) as it is fixed from both ends at rest. In this case, the tension force will be the same at all points on the tubing. Taking a point sufficiently far from point B, we can approximate the tubing as a cylindrical pressure vessel. Force F_t can be found by applying a force balance on a cut along the tubing cross section (see Figure 3.3a):

$$F_t = \pi \left((R + t + t_n)^2 - R^2\right) \sigma_x = P\pi R^2 \tag{3.7}$$

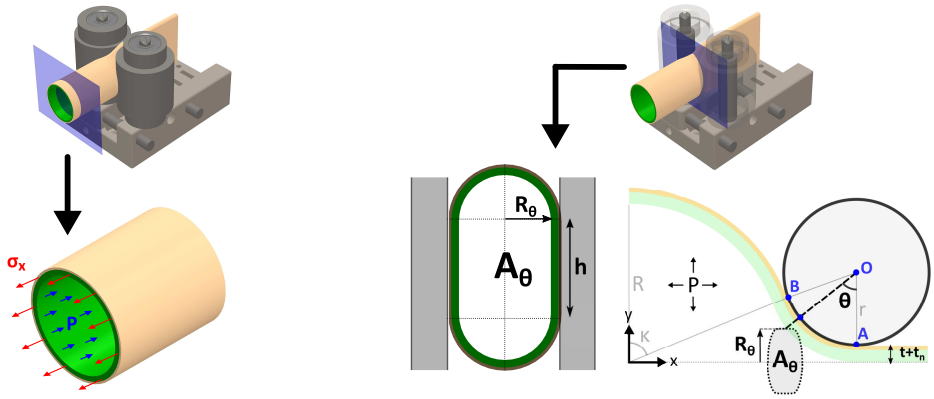

(a) **(b)**

Figure 3.3. (a) Forces acting on the tubing cross section at a point sufficiently far from point B (b) Cross section of the tubing between points A and B at angle θ [39].

In order to find F_p, we must calculate the total contact area between the rollers and the tubing. At any angle defined by θ between points A and B, we estimate the tubing cross-section as a shape with the width of $2R_\theta$ while maintaining the circumference of the fully inflated section with inner radius R as shown in Figure 3.3b. Calculating R_θ and h results in:

$$R_\theta = r_t\big(1 - cos(\theta)\big) \tag{3.8}$$

$$h = \pi(R - R_\theta) \tag{3.9}$$

At angle θ, tubing pressure P works on the infinitesimal contact area dA which can now be expressed as:

$$dA = hr_t d\theta \tag{3.10}$$

Neglecting inward force due to shrinkage of the rubber layer, x and y components of F_p can be calculated as an integral over dA:

$$F_{px} = P \int_0^\kappa sin\,\theta\,\pi \cdot \big(R - R_\theta\big)\, r_t\; d\theta \tag{3.11}$$

$$F_{py} = P \int_0^\kappa cos\,\theta\,\pi \cdot \big(R - R_\theta\big)\, r_t\; d\theta \tag{3.12}$$

Although radius of the outer nylon layer R_n remains constant, radius R and thickness t of the inner rubber layer changes with tubing pressure. In this study, strains on the rubber layer do not exceed %60 ($R_{max} \leq 5$ mm). For simplicity, it is assumed that the rubber layer has a roughly linear stress-strain relationship at small strains. However, for larger strains, an hyperelastic material model can be used. We assume that the tubing is fixed at both ends, so no deformation occurs in axial direction and radial strain is negligible ($\epsilon_x = 0, \epsilon_r = 0$). For a thin-walled cylindrical pressure vessel $\sigma_r \approx 0$ and:

$$\sigma_\theta = \frac{PR}{t} \tag{3.13}$$

Using Equation 3.13 and considering the Hooke's law for triaxial stress state [40] we can obtain an expression for ϵ_θ. We can also calculate the deformed thickness t of the rubber knowing that the total volume stays constant ($\nu = 0.5$).

$$\epsilon_\theta = \frac{R - R_o}{R_o} = \frac{1 - \nu^2}{E}\sigma_\theta \tag{3.14}$$

$$t = \frac{R_o}{R}\, t_o \tag{3.15}$$

Combining Equations 3.13, 3.14 and 3.15, we can express R in terms of tubing pressure P. This equation is only valid when the tubing is inflated and has a radius lower than R_{max} which is the maximum radius the tubing can reach before being constrained by the outer layer. The final expression for tubing inner radius R can be found using Equation 3.16.

$$R = \begin{cases} R_o & R \leq R_o \\ \dfrac{\lambda - \sqrt{\lambda^2 - 4PR_o\lambda}}{2P} & R > R_o \text{ and } R < R_{max} \\ R_{max} & R \geq R_{max} \end{cases} \tag{3.16}$$

where $\lambda = \dfrac{Et_o}{1 - \nu^2}$ and $R_{max} = R_n - t$

The model contains the following parameters: E and ν are the Young's modulus and Poisson's ratio for the rubber tubing respectively; R_o and t_o are natural inner radius and wall thickness respectively; P is tubing pressure, r is roller radius; R_n and t_n are fixed inner radius and wall thickness of the outer layer respectively. Variables R and t denote the current inner radius and wall thickness of the rubber tubing and are dependent on pressure (P).

This model was developed for a composite tubing with two layers. It is assumed that the softer inner layer has an inner diameter that changes with pressure whereas the stiff outer layer has a fixed diameter. However the model can also be applied to different types of tubings by changing the model parameters, namely mechanical properties of the inner layer (E and ν) and the natural inner radius and wall thickness (R_o and t_n). For instance, the inner layer can be neglected by setting $R_o = R_{max}$ and $t_o = 0$.

3.2.2. Speed

When controlled by a motor, the speed of the actuator is directly related to motor speed assuming enough force is generated to initiate motion. When slack portion is attached to the motor, the pinch-roller drive essentially forms a single movable pulley as shown in Figure 3.2.2. In this case, tip velocity (v_{tip}) is simply half of the tangential velocity of the spool on which the tubing is wrapped (in the given equation r_s represents spool radius and w represents motor speed in rad/s):

$$v_{tip} = \frac{\omega r_s}{2} \tag{3.17}$$

The pinch-roller will reach maximum speed only when the rollers can move freely on the pressurized tubing. This is called unconstrained speed as the slack section is not constrained by a motor. For unconstrained speed, tubing pressure and friction losses in the pinch-roller are the limiting factors.

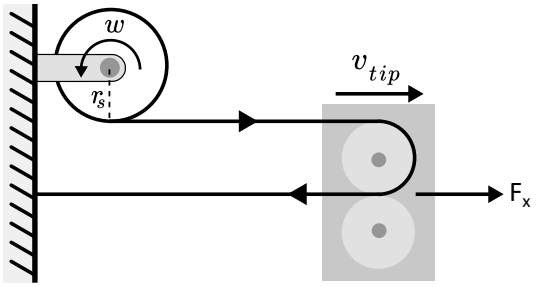

Figure 3.4. When controlled by a motor, the actuator can be modeled as a loaded movable pulley where force F_x is applied by the inflated tubing at the tip.

3.2.3. Stiffness

In addition to calculating actuator force and speed, understanding the stiffness of the inflated tubing is also important for the design of the actuator. This includes static failure due to internal pressure and also failure due to buckling and bending.

3.2.3.1. Burst Pressure. Calculating the burst pressure of the tubing is necessary to determine the operating range for pressure and characterize the actuator's durability. For a thin-walled pressure vessel, stresses on the membrane can be calculated using Equations 3.18, 3.19 and 3.20.

$$\sigma_\theta = \frac{PR}{t} \tag{3.18}$$

$$\sigma_x = \frac{PR}{2t} \tag{3.19}$$

$$\sigma_r \approx 0 \tag{3.20}$$

The burst pressure P_b of the tubing can be estimated conservatively using the Tresca criterion for a thin-walled pressure vessel made of ductile material [40]:

$$P_b = \frac{\sigma_o \, t}{R} \tag{3.21}$$

where σ_o is the tensile strength.

It should be noted that Equation 3.21 does not take into account the effect of hydrostatic pressure which can significantly affect the yield strength of polymers. For most glassy polymers, the modified Tresca criterion gives a satisfactory description of the yield process for samples under tensile hydrostatic stress [41]:

$$P_b = \frac{2\tau_o\, t}{R(1+\mu_T)} \tag{3.22}$$

where τ_o is the shear strength at zero hydrostatic pressure and μ_T denotes the pressure sensitivity of the material.

3.2.3.2. Buckling Failure. Another important design criterion is buckling. Thin-walled pressure vessels have higher bending and buckling stiffness compared to regular thin-walled beams due to the addition of internal pressure which increases load carrying ability. Therefore, the classical beam theory cannot be used to accurately describe buckling in pressure vessels. As a load is applied to an inflated cylindrical beam, wrinkles begin to form on the membrane. The propagation of these wrinkles leads to buckling failure (see Figure 3.5a).

Le Van and Wielgosz successfully obtained linearized equations for critical buckling force of a cantilevered inflated beam under compressive force illustrated in Figure 3.5b [42].

$$\begin{aligned} F_c^2\frac{\Omega^2 I}{A_0} + \Omega^2 I(E+p/A_0)(p+kGA_0) - F_c[\Omega^2 I(E+p/A_0)\ldots \\ +(p+kGA_0)(1+\Omega^2 I/A_0)] = 0 \end{aligned} \tag{3.23}$$

Solving for the smaller root of Equation 3.23, critical buckling force (F_c) is obtained as:

$$F_{c\,,\,LeVan} = \frac{(E+\dfrac{p}{A_o})I\Omega^2}{1+\Omega^2\dfrac{I}{A_o}+\Omega^2\dfrac{(E\dfrac{p}{A_o})I}{p+kGA_o}} \tag{3.24}$$

where

$$\Omega = \frac{\pi}{2L_o} \tag{3.25}$$

For thin-walled cylindrical beams the correction shear coefficient k can be taken as 0.5 [43]. In Equations 3.24 and 3.25, E is the elastic modulus, G is the shear modulus, p is axial force due to pressure ($p = F_x$), I is the second moment of area, A_o is cross-sectional area of the tube before inflation and L_o is natural length of the beam before inflation.

Fichter also achieved linearized equations for an inflated tubing under compressive axial force [44]. Considering a simplified 2D case on the xy-plane, he shows that the following ordinary differential equation can be obtained for rotation around the z-axis ($\omega = \frac{du}{dx}$)

$$\omega^{''} + \beta^2 \omega = \frac{\beta^2 C}{F_c} \tag{3.26}$$

where

$$\beta^2 = \frac{F_c}{E\pi r^3 t}\left(\frac{p + G\pi rt}{p + G\pi rt + F_c}\right) \tag{3.27}$$

For a cantilevered beam, the boundary conditions are:

$$u(0) = \omega(0) = \omega^{'}(L) = \omega^{''}(L) = 0 \tag{3.28}$$

Applying the boundary conditions above to Equation 3.26 and solving for a nontrivial solution, we obtain:

$$\beta L = \frac{\pi}{2} \tag{3.29}$$

Finally, substituting Equation 3.27 into Equation 3.29 and solving for F_c, the following expression is obtained:

$$F_{c\,,\,Fichter} = \frac{EI\dfrac{\pi^2}{4L^2}(p + G\pi rt)}{EI\dfrac{\pi^2}{4L^2} + p + G\pi rt} \tag{3.30}$$

where $I = \pi r^3 t$ for a thin-walled cylinder and, r, t, L are radius, wall thickness and length of the beam respectively.

3.2.3.3. Bending Failure. If instead a transverse load is applied at the tip, bending will occur as illustrated in Figure 3.5b. It has been shown that critical bending load can simply be estimated using Equation 3.31 [45].

$$F_b = \frac{\pi\, p\, r^3}{L} \tag{3.31}$$

These equations have been verified experimentally and were shown to provide a good estimation for thin-walled tubings similar to the ones used in the proposed actuator [32]. They can be used as general guidelines to estimate the critical bending and buckling forces for the inflated tubing.

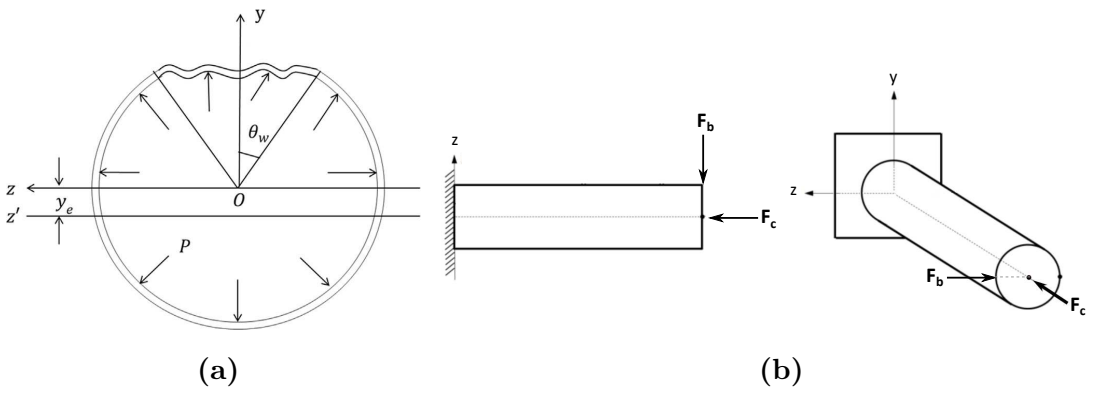

Figure 3.5. (a) Transverse section of an inflated beam under wrinkling (θ_w denotes the wrinkling angle) [46]. (b) Cantilevered inflated beam under compressive and transverse force.

3.3. Prototype

3.3.1. Design Iterations

Multiple design iterations were made for the pinch-roller drive (Figure 3.6). The initial design (Figure 3.6a) consisted of two rollers housing small 8 mm bearings mounted on a fixed base. The distance between rollers was adjusted by hand and fixed with a set screw. After initial testing, main issues with the design were found to be: air leak between the rollers, shafts bending at high pressures and the tubing sliding out of alignment due to poor retention. These problems were rectified in the final iteration (Figure 3.6c). The adjustment mechanism was improved by adding a single tightening screw in the middle with two guide shafts on each side. Steel roller shafts and longer rollers were added to fix shaft bending and poor tubing retention.

3.3.2. Inflatable Tubing

Initial tests of the actuator were done using a 0.035 mm thick Polyamide 12 (PA12) tubing with 5 mm OD provided by Simeks Medical. These tests revealed the importance of achieving a tight seal between the rollers for smooth, continuous motion. The PA12 sample has high hardness and low surface roughness which made sealing difficult; even a small misalignment between roller shafts lead to air leaks.

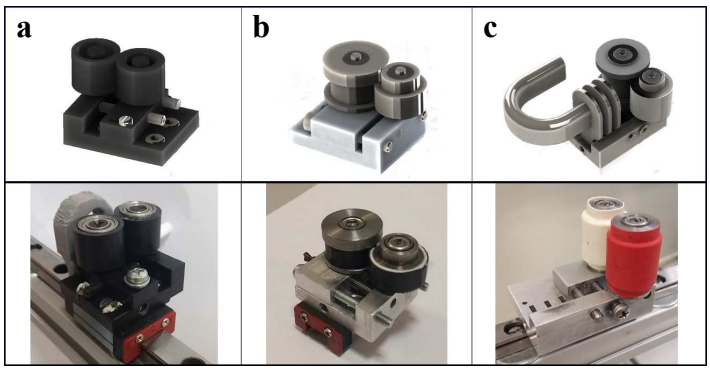

Figure 3.6. Design iterations of the pinch-roller drive where (a) is the first, (b) is the second and (c) is the final prototype.

Figure 3.7. The actuator extending at constant speed while the slack section is released by the motor. Composite PA12/L tubing with 5 mm OD is used.

For this reason, a soft latex tubing was placed inside the PA12 outer layer to minimize leakage. The composite PA12/L tubings with 5 mm OD can be seen in Figure 3.7. Detailed discussion about characterization of different tubing materials and their comparison can be seen in Section 3.5.1. Technical specifications of all tested tubings are given in Table 3.1.

3.4. Experimental Methods

Tubing characterization experiments were performed to assess force capability of the actuator using different tubings and determine the effects of design parameters such as tubing diameter and material on design requirements such as output force, sealing and flexibility. Results of the tubing characterization experiments were used to select the most suitable tubing sample for use in the soft continuum robot described in Chapter 4. The selected tubing was also used in maximum speed and model validation experiments.

3.4.1. Experimental Setup

A 1-DoF test setup was designed and manufactured to test the highly extensible actuator. The test setup was used to assess feasibility of the pinch-roller drive concept, make improvements to the design, test different tubing materials and check validity of the models. The test setup consists of a pinch-roller drive attached onto a linear carriage and mounted on a linear rail (DMN-09) to minimize friction and restrict motion

to one degree of freedom (see Figure 3.8). A single pressure transmitter (Keller PA 21-Y) was used to record pressure data and solenoid valves (FG Line C01) were used to control the air flow. Pneumatic line was connected to a pressure tank (Proter 24L) which was used as the main pressure source. Dynamixel AX-12A smart serial servo motor was used to control extension and contraction.

The test-setup was used in two main configurations: (1) with the tubing in straight configuration and fixed from both sides (see Figure 3.8b) and (2) tubing connected to the servo motor (see Figure 3.8c). First configuration was used to measure maximum actuator speed and force. Second configuration was used to test controlled motion of the actuator.

(a)

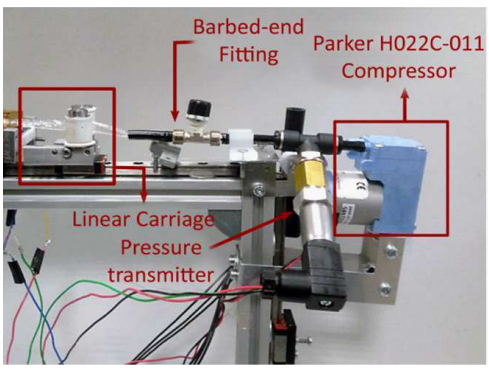

(b)

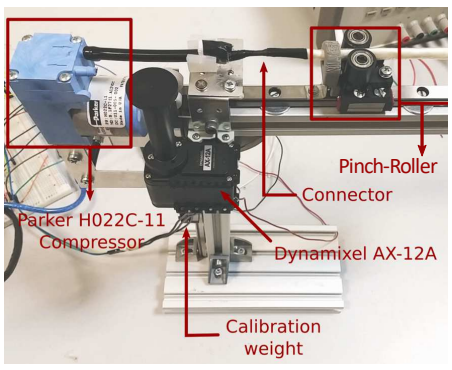

(c)

Figure 3.8. (a) CAD model of the 1-DoF test setup. (b) First configuration used for experiments and (c) second configuration used to test actuator motion. Note that the miniature pump was replaced with a pressure tank in the final design (Figure 3.11).

3.4.2. Tubing Characterization

Four design criteria were chosen to assess the suitability of the tested tubing samples. These criteria are listed below in order of importance:

(i) Flexibility and softness
(ii) Force output
(iii) Sealing
(iv) Durability

Flexibility is the most important criteria since the actuator is designed for soft robotic applications. Force output is also crucial since the tubing has to generate enough force to actuate the pinch-roller drive even at low pressures. Achieving a good seal is important for continuous operation as any air leakage can cause the slack (uninflated) section to inflate, leading to intermittent motion and even locking of the actuator if pressure at the slack section balances the inlet pressure. Finally, durability is also considered since the tubing has to operate inside the desired pressure range without failure.

Tested samples are shown in Figure 3.9 and their specifications are given in Table 3.1. Discarded samples that did not actuate the pinch-roller are not shown in this figure. These samples were either too thick or stiff. Samples (4)-(7) are double-layered tubings manufactured in-house. These samples have a thin, durable outer layer made of a hard polymer (e.g. PA12) to increase yield strength and a soft inner layer made of natural rubber latex to provide sealing and increase flexibility. The tubings for both layers were obtained separately as stock samples from different manufacturers and assembled by hand. Natural rubber latex tubings were obtained from Qualatex.

Table 3.1. Specifications of the tested tubing samples. The ones with no manufacturer information were manufactured in-house.

#	Code	Material	Manufacturer	OD (mm)	Thickness (mm)	Shore
1	PA12(5)	Polyamide 12	Simeks	5	0.035	75D
2	PA12(10)	Polyamide 12	Simeks	10	0.035	75D
3	PEL	Pellethane	Lubrizol	4.572	0.254	80A
4	HDPE/L	HDPE+Latex	-	16	0.400	68D+35A
5	LDPE/L	LDPE+Latex	-	10	0.390	55D+35A
6	PA12/L(10)	PA12+Latex	-	10	0.335	75D+35A
7	PA12/L(5)	PA12+Latex	-	5	0.335	75D+35A
8	PB72	Pebax	Vention	5.613	0.127	72D
9	PB55	Pebax	Vention	5.613	0.127	55D
10	PTFE	PTFE	Zeus	7.823	0.127	60D

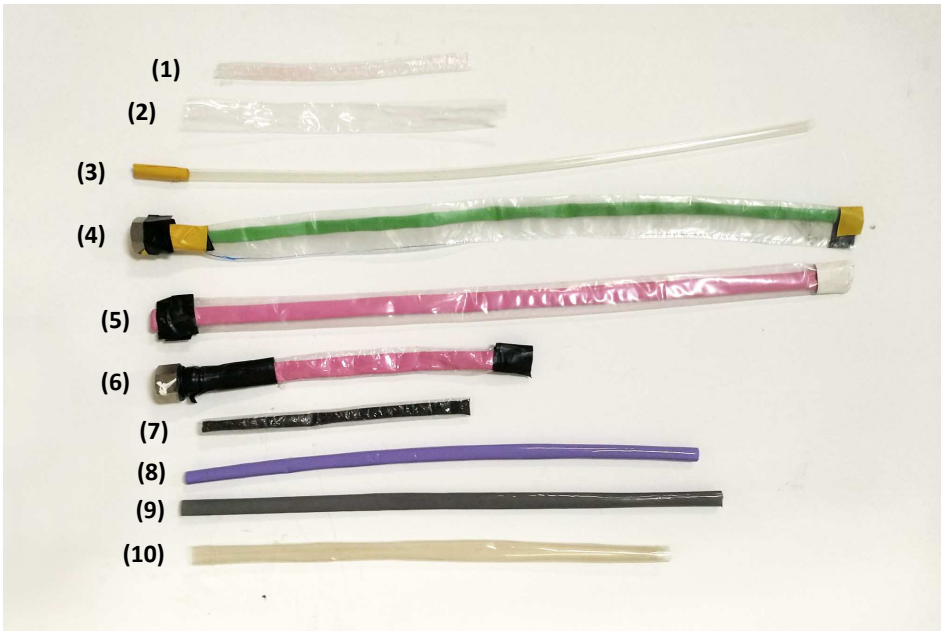

Figure 3.9. Tested tubing samples. Tubing specifications are given in Table 3.1.

Main design parameters considered were tubing material, outer diameter (OD), wall thickness and Shore Hardness as a measure of softness. Friction coefficient (μ) between roller and tubing outer layer is also a design parameter that affects force output (see Section 3.2.1). However, it was not considered during the selection process since as long as the rollers are rotating properly (i.e. model follows the NS assumption) friction coefficient does not have a major impact on actuator performance. OD, which is the main parameter for actuator force as shown in Section 3.2.1, is not the same for every sample since only stock samples and samples produced in-house could be tested due to manufacturing limitations. For this reason, force data for each sample was divided by the cross-sectional inside area of the tubing (πR^2) to normalize the results.

An ATI Nano 17 force/torque sensor was used to record force data. The sensor was mounted on a fixed frame (see Figure 3.11b) and connected to the NI-PCI 6220 data acquisition card. Analog data was converted to force measurements (N) using the LabView ATI DAQ library. Tests were done by keeping the tubing length constant at 100 mm and recording the maximum force output at different tubing pressures to characterize the force/pressure relationship for each sample. The tested range was between 40-160 kPa which is considered to be the operating range.

3.4.3. Maximum Speed

A push-button was mounted onto the fixed frame used for force experiments and the pinch-roller was positioned at a pre-determined starting position before each trial as shown in Figure 3.10. Tubing pressure and time elapsed for the base to move a displacement of 80 mm was recorded using NI CompactRIO Real-Time Operating System (RTOS). The average speed was calculated using the measured elapsed times. Tubing pressure (gauge) was increased from 0-400 kPa at roughly 25 kPa intervals.

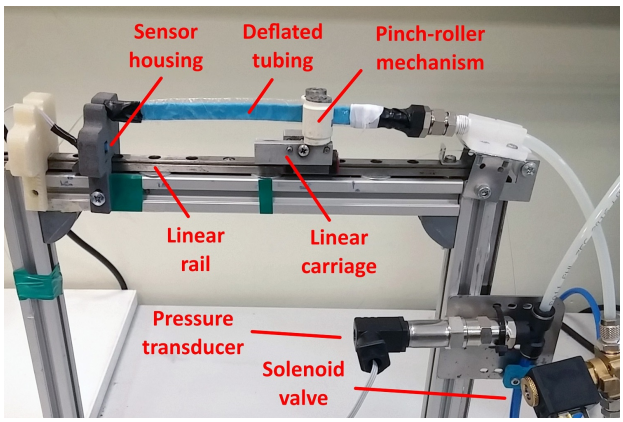

Figure 3.10. The experimental setup used for maximum speed tests. A push button is mounted inside the sensor housing and the linear carriage is manually pulled back to the starting position before each trial.

3.4.4. Model Validation

Model validation experiments were performed to verify the models given in Section 3.2 for output force, critical buckling and bending loads.

3.4.4.1. Force. Force data was taken using the same procedure mentioned in Section 3.4.2. The sensor was recalibrated before each trial. Tubing pressure (gauge) was increased from 0-300 kPa at roughly 25 kPa intervals and experimental results were compared to the force model. The experiment was performed on two PA12/L tubings with the same specifications to evaluate repeatability.

The following model parameters were used: $E \approx 2$ MPa, $\nu = 0.5$, $\mu \approx 0.4$, $R_o = 3.3$ mm, $t_o = 0.375$ mm, $t_n = 0.03$ mm, $R_n = 4.97$ mm and $r = 7.5$ mm. R_o, t_o, t_n, R_n and r were measured using electronic calipers, ν was taken from literature data for natural latex rubber and E was obtained as an approximate value from the manufacturer's technical data sheet (Qualatex).

3.4.4.2. Buckling Failure. The effect of tubing length on critical buckling force (F_c) was investigated at a constant tubing pressure of 100 kPa.

Tubing length was decreased from 200-50 mm at 25 mm intervals. The ATI Nano 17 force/torque sensor was attached to the actuator as shown in Figure 3.11. At each length, the adjustment screw was tightened to prevent the pinch-roller from moving and the compressive force applied on the sensor was increased slowly until the inflated beam buckled. The maximum force was recorded just before buckling failure . Three trials were done at each length and the results were compared to the F_c calculated using the models given in Section 3.2.3.2.

3.4.4.3. Bending Failure. Critical bending force (F_b) was also measured at different lengths by keeping pressure constant at 100 kPa and decreasing tubing length from 200-25 mm at 25 mm intervals. Similar to the buckling experiments, the ATI Nano 17 force/torque sensor was attached to the side of the actuator. A transverse force was applied at the tip until bending failure occurred and the maximum force was recorded. Three trials were done at each length and the results were compared to the F_b calculated using the model given in Section 3.2.3.3.

A single layer, LDPE tubing with 10 mm OD was used for both buckling and bending tests since the model assumes homogeneous, elastic material. The specifications are the same as the LDPE/L tubing shown in Table 3.2 without the inner layer. The following model parameters were used: $E \approx 300$ MPa, $G \approx 105$ MPa, $R = 5$ mm and $t = 0.090$ mm.

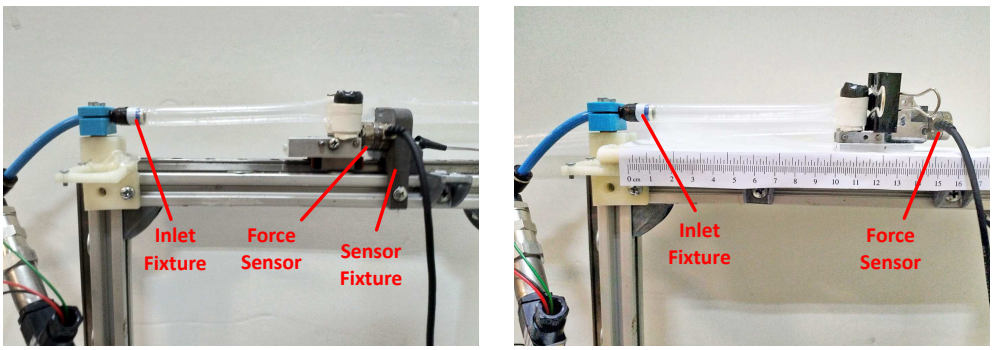

(a) **(b)**

Figure 3.11. Experimental setup used for (a) measuring actuator force and (b) for buckling experiments.

3.5. Results and Discussion

3.5.1. Tubing Characterization

Normalized force profiles of the tested tubings are given in Figure 3.12a. Burst pressure estimates are also shown for each tubing next to the respective force profile. Note that the values labeled with (∗) were determined experimentally and the others were obtained from the manufacturer. The rankings for all four selection criteria are given in Figure 3.12b. We based the force ranking on normalized force results and the durability ranking on burst pressure ratings. Rankings for flexibility and sealing were determined empirically through observation.

PTFE sample was not tested due to significant air leak between the rollers. Sample with code name HDPE/L was also not tested due to very low durability (burst pressure $<$ 100 kPa). This sample was manufactured in-house by covering a rubber latex tubing with a thin (0.1 mm) HDPE sheet using an impulse heat sealer. However, we were not able obtain a strong seal which significantly lowered durability. Samples with 10 mm OD were used for PA12 and PA12/L.

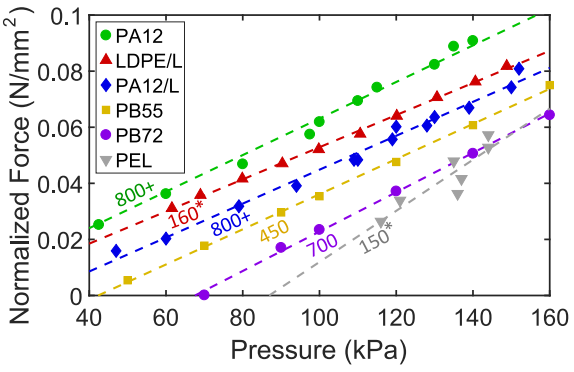

(a)

#	Flexibility	Force	Sealing	Durability
1	LDPE/L	PA12	PA12/L	PA12
2	PEL	LDPE/L	LDPE/L	PA12/L
3	PA12/L	PA12/L	PEL	PB72
4	PA12	PB55	PA12	PB55
5	PB55	PB72	PB55	LDPE/L
6	PB72	PEL	PB72	PEL

(b)

Figure 3.12. (a) Normalized force (force output/effective area) for tested tubing samples between 40-160 kPa. Burst pressure estimate (kPa) for each tubing is also shown next to the respective force profile. (b) Ranking of the tested samples for all selection criteria from highest to lowest rank (1-6).

Results indicate that PA12 sample had the highest force output, reaching a normalized force close to 0.1 at 150 kPa. LDPE/L and PA12/L samples also produced significant force, reaching a normalized force of 0.08 at 150 kPa.

Although the PA12 sample had the highest force output and durability, it had low flexibility and had problems with sealing. In general, hard polymers (PA12 and PB55) produced enough force to actuate the pinch-roller but did not provide enough sealing between the rollers. Conversely, soft polymers such as Polyurethane (PEL) provided enough sealing but produced low force and underwent radial deformation which was undesirable. For this reason, LDPE/L and PA12/L, the two double-layer tubings with rubber latex inner layer were chosen as the most suitable candidates in terms of both force output, sealing and flexibility. The inner layer provides adequate sealing between the rollers while the outer layer restricts radial expansion of the rubber and increases durability without compromising flexibility of the tubing. Between these two samples, PA12/L had higher durability (burst pressure $\sim$ 800 kPa) than LDPE/L (burst pressure $\sim$ 160 kPa). However, we were not able to obtain PA12 samples longer than 120 mm from the manufacturer. For this reason PA12/L tubings were used for maximum speed and model verification tests to reach pressures higher than 160 kPa whereas the longer LDPE/L tubings were used in the soft continuum robot (see Chapter 4). Technical specifications of these tubings are given in Table 3.2.

Table 3.2. Detailed technical specifications of the PA12/L and LDPE/L tubings shown in Figure 3.1.

PA12/L						
Layer	**Material**	**OD (mm)**	**Wall Thickness (mm)**	**Elastic Modulus (MPa)**	**Shore**	**Length (mm)**
Inner	Latex	6.5	0.3	2	35A	120
Outer	PA 12	10	0.035	1100	75D	120
LDPE/L						
Inner	Latex	6.5	0.3	5	35A	300
Outer	LDPE	10	0.090	300	55D	300

3.5.2. Maximum Speed

Maximum (unconstrained) speed data and the corresponding curve fit are given in Fig. 3.13a. Tip speed was recorded as zero under 25 kPa since force generated was not enough to actuate the pinch-roller. A square-root relationship was observed. The actuator was able to reach speeds in excess of 1 m/s at pressures above 200 kPa.

3.5.3. Model Validation

3.5.3.1. Force. The experimentally obtained force data from the two tubings and the model results are given in Figure 3.13b. The force-pressure relationship was highly similar for both tubings which indicates repeatability. The solid F_{NS} line is the model prediction assuming no-slip condition at the roller surface. The dashed F_{FS} line is the model prediction with full slip. For full-slip condition, we determined an average static friction coefficient of $\mu = 0.4$ at the nylon-aluminum interface from the literature [47].

The model lines have a curved region at pressures between 0-150 kPa which occurs as the inner rubber layer is not fully expanded in this pressure range. As tubing pressure is increased, the inner rubber layer expands, which leads to an increase in the inner radius (R) and consequently the force output (F_x) as shown in Equation 3.16. When R reaches its maximum value (R_{max}), it can no longer increase due to the inner layer being constrained by the rigid outer layer. This manifests as a kink around 150 kPa on the model line. After this point, the pressure-force relationship stays linear as expected.

It can be seen in Figure 3.13b that the experimental results deviate from the no-slip prediction and rather lie between the NS and FS lines, especially at pressures higher than 100 kPa. This may be due to the relatively low friction coefficient of the tubing outer surface (PA12). A material pairing with higher friction coefficient can be used to prevent slippage and obtain higher forces.

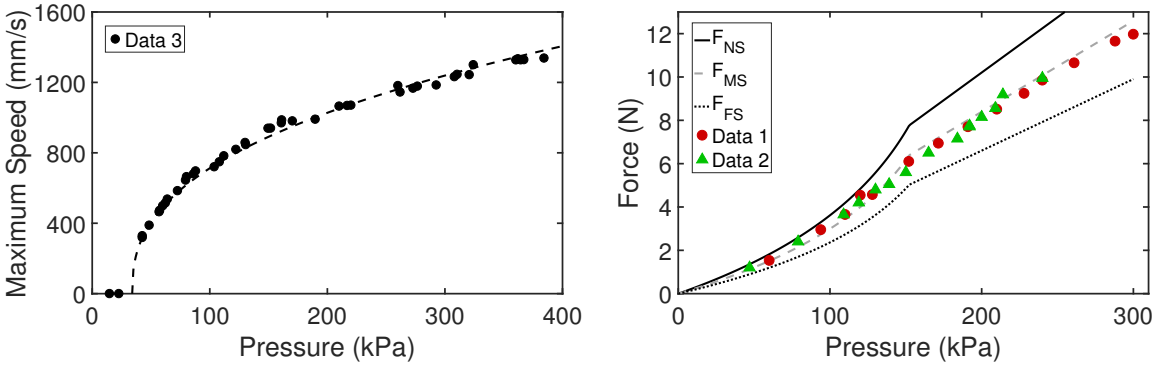

Figure 3.13. (a) Maximum extension speed and pressure relationship. (b) Force and pressure relationship. Solid and dashed lines represent the theoretical models. Data 1, 2 and 3 represent the measurements taken from three separate tubings.

In addition to friction losses, differences in the roller-tubing interface geometry, material deformation and manufacturing imperfections (e.g. roller shafts not being perfectly aligned, air leak between the rollers at high pressures) may have also contributed to the drop in force output. In order to take these losses into account, a mixed-slip (MS) condition is also added to the figure which is the average of the NS and FS lines. The dashed gray F_{MS} line fits the data well both at low and high pressures.

3.5.3.2. Buckling Failure. The experimental results for the buckling experiments and the model estimation using both Le Van's and Fichter's models are given in Figure 3.14a. Both models produced similar results although Fichter's model lies slightly below Le Van's at lower tubing lengths, possibly due to the increased effect of the shear modulus. Overall, the experimental results fit the model estimation at high lengths and follow a similar trend. The failure load is inversely proportional to tubing length as the models suggest. However, measured data deviates from model estimation at tubing lengths lower than 100 mm. This could be due to the formation of local buckling regions on the tubing surface due to wear. The experiment was performed on a single sample and measurements were taken with descending length, which could have compounded this effect at lower lengths.

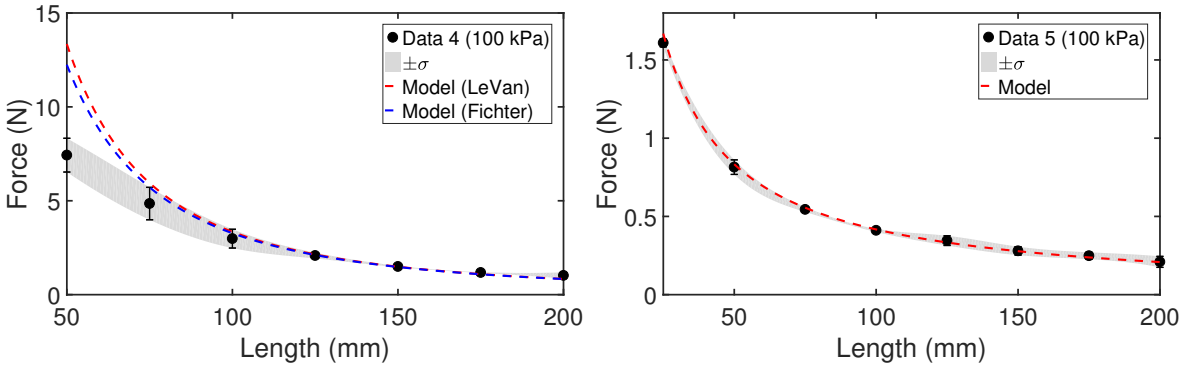

(a) **(b)**

Figure 3.14. Results of the buckling and bending experiments. (a) Measured critical buckling force (F_c) compared to the two models. (b) Measured critical bending force (F_b) compared to the model. Data 4 and 5 indicate that measurements were taken from separate tubings. Shaded areas show the standard deviation.

3.5.3.3. Bending Failure. Figure 3.14b shows the experimental data for bending failure under transverse load and the model estimation calculated using Equation 3.31. The model matches the data very well at both high and low tubing lengths.

3.5.3.4. Roller Diameter. As shown in Section 3.2.1, design parameters that affect force output are tubing outer layer diameter (R_n), tubing inner layer dimensions and material (R_o,t_o,E,ν), friction coefficient (μ) and roller radius (r). Roller radius is the easiest parameter to control since tubings could not be manufactured with custom specifications and instead were chosen from readily available samples. Therefore, the effect of roller diameter to tubing diameter ratio ($\frac{r}{R_n}$) on output force is investigated in Figure 3.15. For all three cases, decreasing the roller diameter leads to higher output force. However, this effect is more noticeable in the NS model since tension force (F_{tx}) which increases with decreasing roller diameter is more significant. In the FS case, pressure force F_{px} is more significant than F_{tx}. Since F_{px} decreases with decreasing roller diameter instead, the effect of roller diameter on output force is reduced.

Results from Section 3.5.3.1 indicate that the MS model gives the closest results to experimental data. It can be seen that although a roller/tubing diameter ratio of 0.25 gives the highest force, increasing the roller diameter fourfold only leads to a 7% reduction in force (0.41 N) at 100 kPa with the MS model (see Figure 3.15a). This reduction is slightly more prominent at higher pressures, reaching 9% (0.81 N) at 200 kPa (see Figure 3.15b). It can be said that optimizing roller diameter is more important at high pressure ranges ($\gg$ 200 kPa). Nevertheless for the expected operating range between 40-140 kPa, roller/tubing diameter ratio does not have significant effect on force, especially if the tubing diameter is necessarily large.

This simulation also demonstrates the importance of using rollers in the actuator as opposed to fixed shafts. Even with the relatively low friction coefficient between nylon and aluminum, the actuator produces 45% less force with the FS condition at 100 kPa ($\frac{r}{R_n} = 0.25$) where the tubing slides between the rollers, as opposed to the NS condition where the rollers are rotating freely.

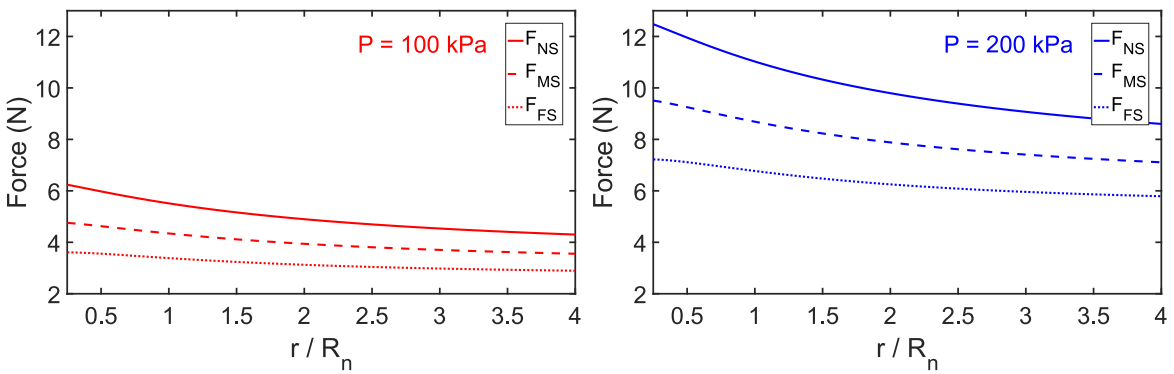

(a) **(b)**

Figure 3.15. Simulating the effect of roller diameter to tubing diameter ratio ($\frac{r}{R_n}$) on output force (a) at 100 kPa and (b) at 200 kPa tubing pressure. R_n was taken as 10 mm for all simulations.

4. DESIGN OF THE SOFT CONTINUUM ROBOT

A major advantage of the proposed actuator is that multiple actuators can be used in parallel to provide active steering to a soft robot. This is due to the inherent flexibility and softness of the inflated tubings. By combining multiple actuators in a soft body and extending them at different speeds (i.e. asymmetrical extension), it is possible to change the direction of motion. In this chapter, application scenarios of the proposed highly extensible actuator to the field of soft robotics are discussed. To this end, two soft continuum robot prototypes have been developed using the proposed actuator. In Section 4.1, design, development and testing of a preliminary prototype with two actuators is discussed. In Section 4.2, design, development and testing of a more sophisticated prototype that can move in 3D space is discussed. The actuators in the preliminary (2D) prototype can be considered to have 2-DoF with bending and extension in one direction while the actuators in the final protoype have 3-DoF with bending in two directions and extension in one direction (see Figure 4.1).

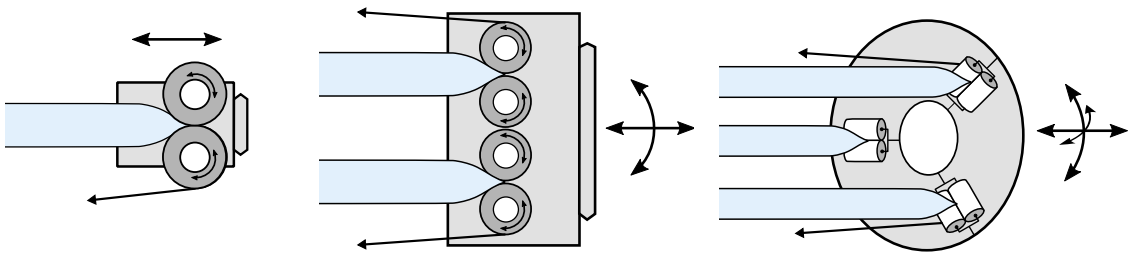

(a) **(b)** **(c)**

Figure 4.1. It is possible to deploy multiple actuators in parallel to form a soft continuum robot that can extend and steer in different directions from the tip. (a) Schematic of a single actuator with 1-DoF, (b) of a robot using two actuators that can navigate on a planar surface, and (c) of a robot using three actuators that can move in 3D free space.

4.1. Preliminary (Planar) Prototype

This section describes the mechanical design, manufacturing and testing of the soft continuum robot using two actuators that can extend and steer on a single plane.

4.1.1. Working Principle

Conceptually, the preliminary prototype consists of two pinch-roller drives mounted side by side on a base (i.e. end effector) which can move freely on a planar surface (Figure 4.2a). Two flexible tubings form the main body, and the base at the tip together with the rollers forms the end effector. The end effector can translate in the x-axis and rotate around the z-axis. Extending or contracting both tubings at the same speed leads to translation whereas asymmetrical extension or contraction leads to rotation. For instance, to rotate the end effector left while going forward, the right tubing (tubing 2) will be released faster than the left one as shown in Figure 4.2b. By extending and rotating the tip, the end effector can cover a planar workspace constrained by length of the main body.

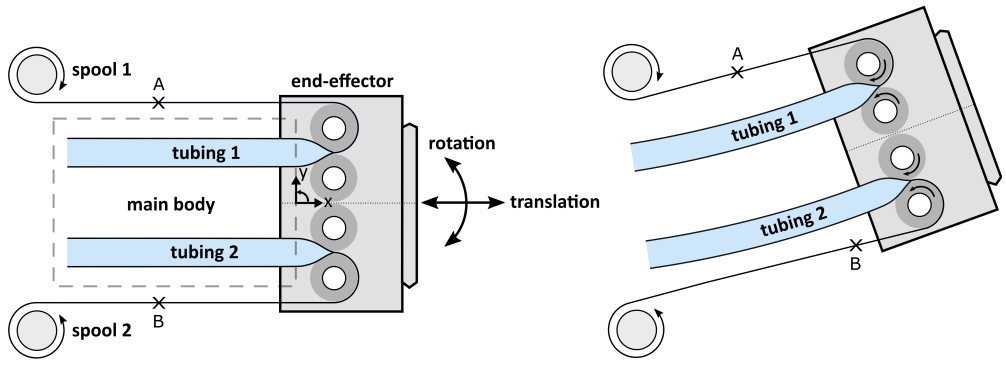

(a) **(b)**

Figure 4.2. (a) Proposed soft continuum robot using two actuators. The end effector can translate in the x-axis, and rotate around the z-axis by extending or contracting the tubings at different rates. (b) The end-effector turns left by releasing tubing 2 faster than tubing 1. Note the location of point B. As tubing 2 is released faster than tubing 1, point B moves farther than point A [39].

4.1.2. Components and Assembly

The robot is composed of three main sections, namely the end effector at the tip, the main body that includes two thin-walled inflatable tubings used as actuators, and the control hub that includes all mechanical and electronic components used to control the robot (see Figure 4.3). In the following subsections, these parts are explained.

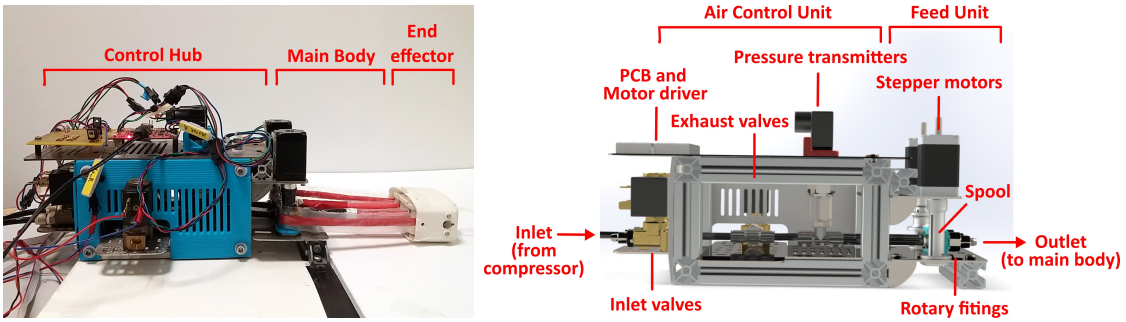

(a) **(b)**

Figure 4.3. (a) Side view of the robot showing the three main sections. (b) 3D model of the control hub with the feed unit (FU) that controls tubing extensions and the air control unit (ACU) that regulates tubing pressures [39].

4.1.2.1. End Effector. The end effector consists of four main components: rollers, fixed base, moving base and outer shell (Figure 4.4a). Majority of the parts were fabricated by a 3D printer for easy prototyping. All components except the roller shafts were printed with *Polyamide (EOS PA 2200)* which is a polymer with relatively low density and high tensile strength. The roller shafts were manufactured on a lathe using *Silver Steel (115CrV3)* since there are threaded holes at both ends of the shafts.

The outer shell is used to protect the pinch-roller from external forces and prevent debris from entering the rollers. It also acts as a housing to attach a force sensor at the tip for experiments (Figure 4.4b). The end effector contains four rollers in total, one on each moving base and two on the fixed base. The outer rollers are positioned on the roller shafts using a double bearing arrangement. The fixed base is stationed at the center and can be mounted onto the outer shell using guiding channels on top

and bottom (Figure 4.4a). Two M4 brass plastic inserts are fitted onto the sides of the fixed base to act as female thread for the tightening screws. The moving base is used to adjust the tightness for each roller pair with the help of a tightening screw (Figure 4.4c).

Major issues encountered during design of the pinch-roller drive (see Section 3.3) were roller shaft alignment, retention of the tubings between the rollers and guide shaft alignment. Several improvements have been made to the design to fix these issues in the preliminary soft robot:

(i) *Roller shaft alignment:* The roller shafts are attached onto the base using countersunk flat head screws to center the shaft and keep it in correct alignment (Figure 4.4c). The screws on top have a smaller diameter (M3) than the screws at the bottom (M4). This was purposely done to simplify assembly and minimize friction by keeping the roller suspended and prevent contact between the roller surface and the base.

(ii) *Tubing retention:* The moving base and the fixed base were designed such that they interlace after assembly which prevents the tubing from sliding along the roller axis during motion.

(iii) *Guide shaft alignment:* The roller pairs can be adjusted separately using the respective tightening screw. Two induction hardened chrome plated rods referred to as guide shafts were used to restrict motion and align the moving bases with the fixed base. Each moving base slides on the guide shaft with the help of two LM4UU linear bearings (Figure 4.4c). 3D printed plastic bushings were used to position the guide shafts on the outer shell (Figure 4.4b).

4.1.2.2. Main Body. Two thin-walled tubings (left and right tubings) comprise the main body (Figure 4.4d). Again, as mentioned in Section 3.5, 120 mm long PA/L tubings were used for force and maximum speed tests and 300 mm long LDPE/L tubings were used for navigation (see Table 3.2 for technical specifications). The main body is connected to the end effector as shown in Figure 4.4d.

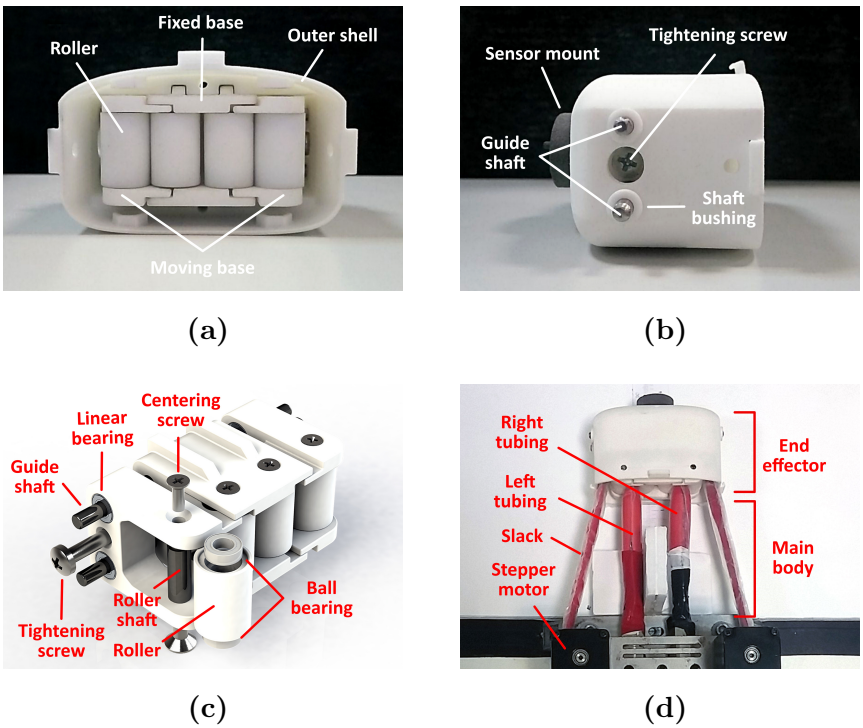

Figure 4.4. (a) Back view of the end effector showing the four main components: roller, fixed base, moving base and outer shell. (b) Side view of the end effector. (c) Exploded view without the outer shell (CAD) showing interior components. (d) Top view of end effector after the tubings are attached [39].

4.1.2.3. Control Hub. The control hub houses all electronic and mechanical components used to regulate tubing pressure and extension speed of the two actuators. Technical specifications of these components can be found in Table 4.1. These components can be further categorized into two: the air control unit (ACU) and the feed unit (FU).

The ACU consists of two pneumatic lines in parallel, one for each tubing. Each pneumatic line contains solenoid valves for inlet and exhaust, a pressure transmitter and a barbed-hose end pneumatic fitting with a rotary joint (Pisco RC6-01) (see Figure 4.3b). Both pneumatic lines are connected at the inlet to a silent air compressor with a 24 lt pressure tank that acts as the main pressure source.

The FU is used to control extension and contraction speeds of both tubings. It includes two stepper motors (one for each tubing), a spool attached onto each motor shaft, and a flanged ball bearing for alignment (see Figure 4.3b). Slack portions of the tubings are coiled around the spools which can be released or wound by the motors. Stepper motors were chosen instead of the servo motor used in the 1-DoF experimental setup for their quick response and precise control of angular position and velocity.

Table 4.1. Technical specifications of the components used in the control hub

Component	Model Name	Technical Specifications
Pressure Transmitter	Keller PA-21Y	0-10 bar, 4-20 mA
Inlet / Exhaust Solenoid Valves	FG Line C01	0-10 bar, 12-24V, 1 lt/min
Silent Air Compressor	Proter 24 lt	0-8 bar, 750 W
Stepper Motor	Nema 11 - 200 Step	4.5V, 670 mA, 950 g-cm

4.1.3. Experimental Methods

Force and speed tests were conducted using a semi-circular barrier with a 120 mm radius of curvature (see Figure 4.5). The center of curvature coincided with the center position between the tubing inlets as shown in the figure. For all experiments, a 10 mm thick smooth PVC plate was used as the test surface (see Figure 4.3a).

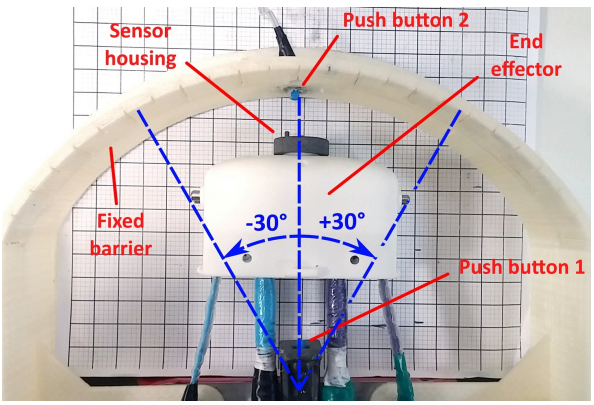

Figure 4.5. Experimental setup used for force and speed experiments. The force sensor is not attached [39].

4.1.3.1. Force Output. Force tests were done to measure the robot's force output during steering at angles between $\pm 30^o$. The force barrier was 3D printed with labels at each 5° rotation interval. The ATI Nano-17 force/torque sensor was mounted onto the end-effector shell using a 3D printed housing.

The tests were performed by manually positioning the end-effector at the desired rotation angle, setting the desired pressure and releasing both tubings at a very low speed (5 rpm) to eliminate effects due to impact. Force values were recorded in radial direction after the sensor touched the barrier and the maximum compressive force applied by the robot was calculated. Measurements were repeated three times at each rotation angle, and the sensor was recalibrated after each trial. A single trial is shown in Figure 4.6 as an example. Note that the force sensor is not attached as the pictures were taken for demonstration purposes.

4.1.3.2. Controlled Speed. Robot speed for straight extension and contraction (0°) was calculated by mounting two push buttons, one at the start position and one at the end position on the barrier. The distance traveled by the end effector between the two points was 32 mm [39]. The measured speed was compared to the input speed which was calculated using the actuator model (see Section 3.2.2).

Each trial was performed by resetting the end effector position (i.e. moving it until it reaches the start or end position) and then releasing the end effector at a constant motor speed. The average speed was calculated by recording the time elapsed for the end effector to reach the end position (see Figure 4.5). Three trials were done at each motor speed and the mean value was taken into consideration. Both extension and contraction speed tests were repeated at 100 kPa and 200 kPa. For contraction speed tests, duty cycle of the exhaust valves was set at 20% for 100 kPa and 30% for 200 kPa to achieve the same main body stiffness [39]. A single trial with both extension and contraction is shown in Figure 4.7.

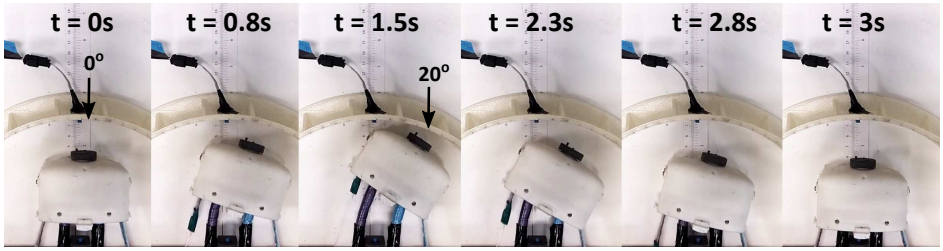

Figure 4.6. The end effector steering at an angle of $+20^o$ in clockwise direction, applying force on the barrier and moving back to the starting position. The force sensor is not attached in these pictures.

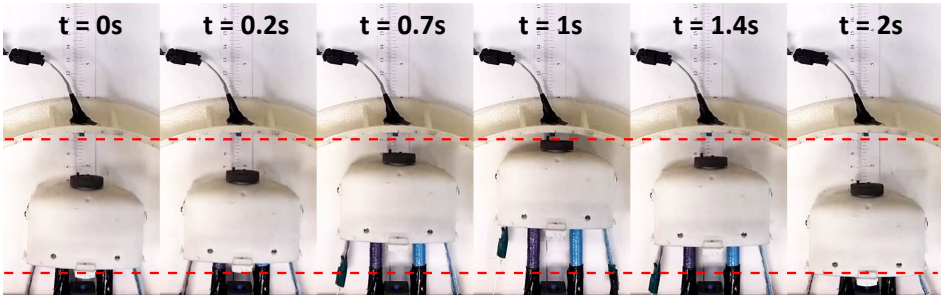

Figure 4.7. The end effector moving forward and backward by extending and contracting the actuator at a constant speed of 28.5 mm/s (90 rpm motor speed).

4.1.3.3. Navigation. 300 mm long LDPE/L tubings were used for navigation experiments (see Table 3.2). Navigation experiments were performed both in open-field, with obstacles and also in closed environments. Extension speed of the actuators were controlled using an user interface (UI) that includes button controls to move the system and to open and close the valves, and numerical controls for adjusting the movement speed and PWM parameters for exhaust valves [39].

4.1.4. Results

4.1.4.1. Force Output. Force and pressure relationship at different rotation angles is given in Figure 4.8a. The force values on the graph are the mean values of the repeated tests in the same angle, including clockwise (+) and counter-clockwise (−) rotation. The solid gray line is the *experimental limit*, which is simply the regression line obtained from actuator force experiments in Section 3.5.3.1 multiplied by two since two actuators are used in parallel (see Figure 3.13b). Maximum force output is obtained at straight extension (0°). Tip force drops with increasing rotation angle as seen in Figure 4.8b. This is caused by a decrease in backbone stiffness due to formation of local buckling regions on the tubing membrane as the backbone diverges from its linear axis.

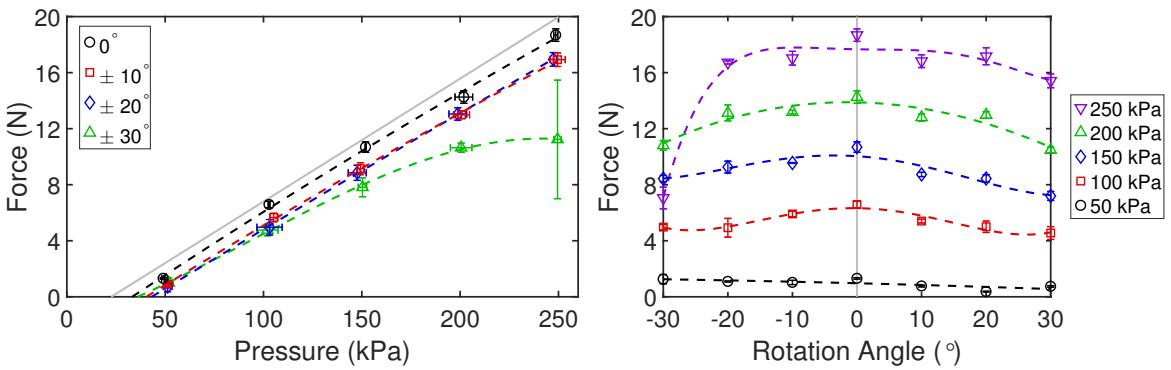

(a) **(b)**

Figure 4.8. (a) Effect of tubing pressure on compressive force and (b) the relationship between compressive force and tip rotation angle in degrees [39].

Maximum measured force is observed to be 1 N below the experimental limit. The frictional force between the end-effector and the test surface was measured using an ATI Nano 17 force/torque sensor. The average static frictional force between the end effector and the surface was measured as 0.35±0.02 N from a total of 10 datasets [39]. The added frictional losses from the rollers combined with the friction between the end-effector and test surface (PVC) could be the reason for the 1 N difference between the maximum measured actuator force and the experimental limit.

Similar values were obtained at $\pm 10^\circ$ and $\pm 20^\circ$ with an additional 1 N drop in the measured force (see Figure 4.8a). Measured force drops drastically above 150 kPa pressure at $\pm 30^\circ$ due to decrease in backbone stiffness. Full buckling was observed during some trials at -30° and 250 kPa causing a drastic reduction in measured force. As a result, data taken at this rotation angle has high standard deviation.

Force and rotation angle relationship and the polynomial regression lines for each data set are given in Figure 4.8b. Although a similar reduction in force is observed for both clockwise and counter-clockwise rotation, the force profiles are not completely symmetric. This can be attributed to manufacturing imperfections and the uneven wear on the tubings which caused one tubing to buckle more than the other. The force reduction was more prominent at higher pressures. Forces close to 20 N were obtained at 250 kPa. However, increasing tubing pressure also increases the probability of full buckling when the tip is rotated, which can be seen at -30°.

4.1.4.2. Controlled Speed. Controlled speed test results are given in Figure 4.9. The model line formed by converting input motor speed to tip speed using Equation 3.17 is also shown for reference. A linear relationship is observed between motor and tip speeds as expected.

The mean absolute error (MAE) between model estimation and measurement at each motor speed is given in Figure 4.10. Measured speed is very close to the model estimation with an average MAE of 2.34 mm/s (extension) and 1.70 mm/s (contraction) at 100 kPa pressure. However, extension speed was measured to be over the model estimation at 200 kPa with an average MAE of 6 mm/s. The highest MAE during extension was 9.2 mm/s at 170 rpm motor speed. The reason of this error might be the increased force exerted by the tubings at 200 kPa (see Figure 4.8) which exceeds holding torque of the stepper motors causing them to miss steps. This problem can be solved by using stronger motors.

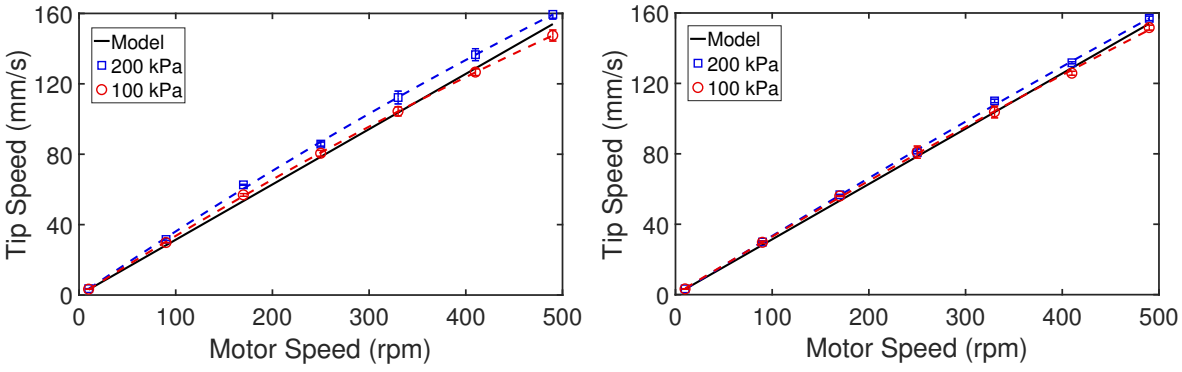

Figure 4.9. Tip speed versus input motor speed during (a) straight extension and (b) contraction. Solid black line represents the tip speed calculated using the theoretical model [39].

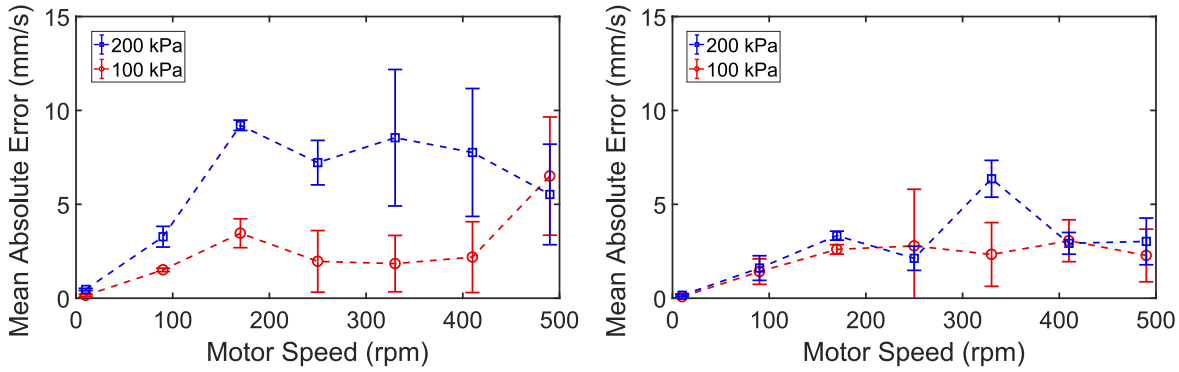

Figure 4.10. Mean absolute error between input and measured (output) speed for (a) straight extension and (b) contraction. Error bars show the standard deviation in data.

4.1.4.3. Navigation. The robot backbone can extend from its initial length of 5 mm to 300 mm at full extension. This corresponds to an extension ratio of 9.5 when the 30 mm end-effector length is added. A rough estimation of the robot's workspace is given in Figure 4.11 where shaded areas are regions in which full buckling is likely to occur. Controlled extension is not possible in these regions although they can still be reached if the backbone is supported by a closed structure as in Figure 4.12.

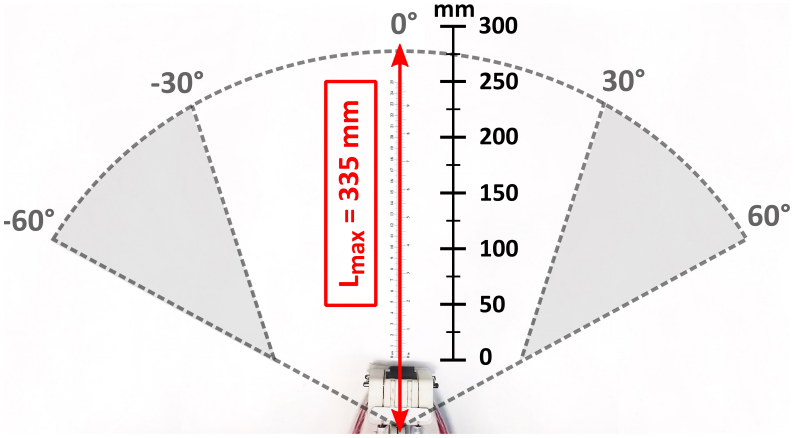

Figure 4.11. Workspace of the proposed soft robot. Maximum length is initial length of the end-effector plus length of the tubings. Shaded areas represent regions where full buckling is likely to occur in at least one tubing [39].

Figure 4.12 shows navigation of the robot in a closed environment to reach a goal position. In addition, Figure 4.13 shows navigation of the robot in an open environment to reach two different goal positions. The closed maze had a minimum radius of curvature of 50 mm. A maximum rotation angle of 45° was reached during motion. The tubing pressure was fixed at 75 kPa for all navigation tests.

Results from the maze tests are a good demonstration of the capabilities of our actuator. The robot was easily navigated to the desired goal position by controlling extension and rotation at the tip. The ability to quickly change the rotation/extension speed based on the environment is very advantageous in such applications since the operator can use low speed for intricate tasks such as maneuvering around an obstacle and higher speeds for simple tasks such as straight extension.

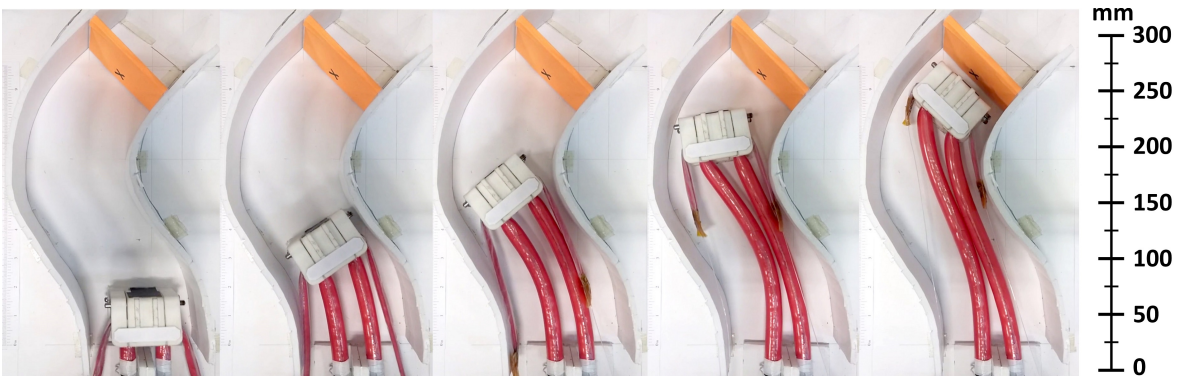

Figure 4.12. The soft robot quickly moves in a curved maze to reach the goal position. The user can follow the maze path accurately during extension by controlling rotation angle at the tip [39].

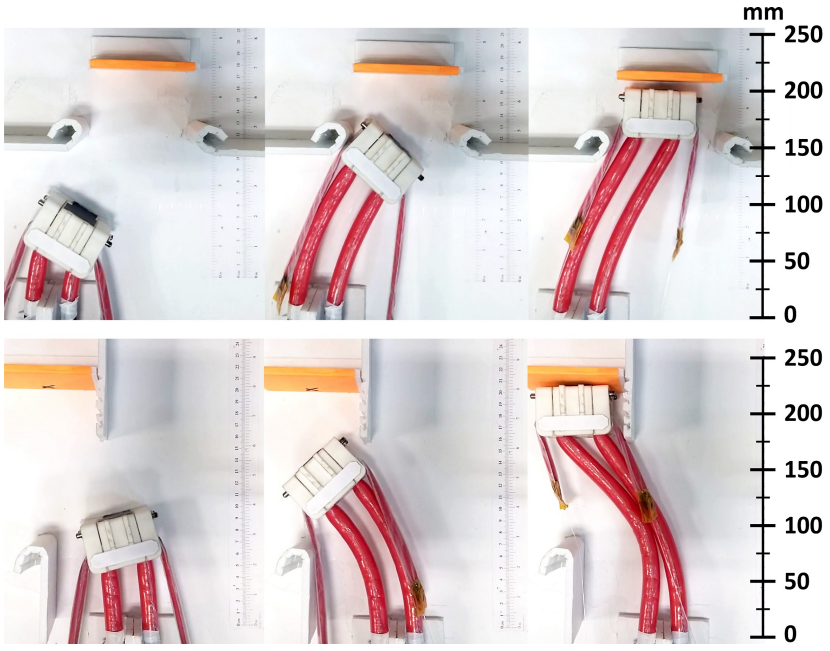

Figure 4.13. The soft robot moves in an open environment while avoiding obstacles. The user can steer the robot to pass through apertures on a wall oriented horizontally (top) or vertically (bottom). The robot can continue exploring the environment after passing through the aperture [39].

4.2. Final (3D) Prototype

This section describes the mechanical design, assembly and testing of the soft continuum robot with three actuators that can move in 3D space. Control system design for the robot is the subject of another study by Talas [48] and is not explained in detail.

4.2.1. Working Principle

The final prototype uses the same working principle as the preliminary prototype which was explained in Section 4.1.1 with an additional actuator. Instead of the parallel configuration used for planar motion, this robot uses a triangular configuration where three actuators are positioned at the corners of an imaginary equilateral triangle at the base and the end effector. This configuration is commonly used in tendon-driven continuum robots with three tendon wires [5]. Figure 4.14 illustrates the basic working principle of the robot with three actuators. In Figure 4.14, black colored triangle is the base, and blue colored triangle is the end effector. Black circles represent the fixed inlets, blue circles represent the pinch-rollers on the end-effector, inflated tubings are shown as thick blue lines and uninflated (slack) sections are shown as dashed blue lines.

When extension speeds of all tubings are the same (i.e. $v_1 = v_2 = v_3$), the robot tip extends straight along the Y-axis if deflection due to gravity is neglected (Figure 4.14a). However, if at any moment, the extension speed of the third tubing is increased so that it is higher than the other two tubings (i.e. $v_1 > v_2 = v_3$), the robot tip will steer in the direction perpendicular to l_{12} which is the opposite side of the imaginary triangle at the tip (Figure 4.14b). Using a combination of different extension speeds, the robot tip can be steered in any desired direction in three-dimensional space. Along with steering direction, the steering angle, or the sharpness of steering, can also be also be controlled by changing the difference in extension speeds. For instance, for the configuration given in Figure 4.14b, steering angle can be increased simply by increasing v_3.

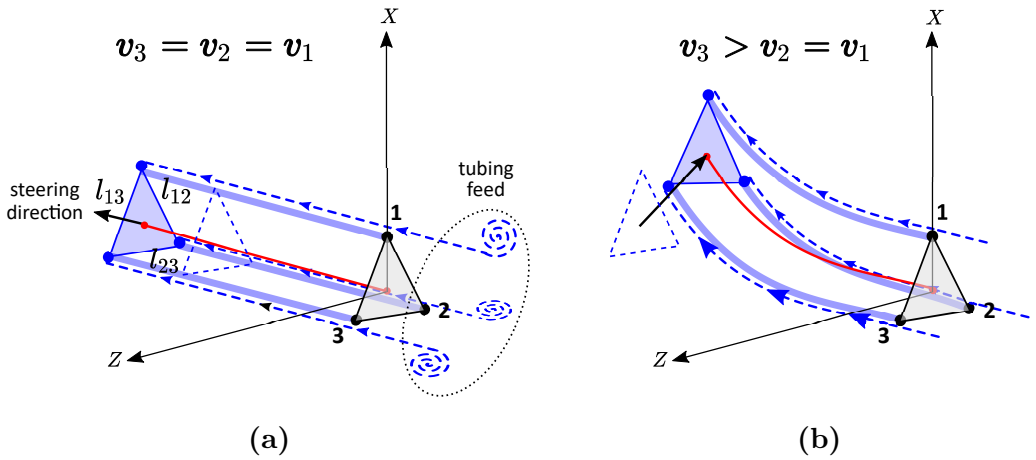

Figure 4.14. Working principle of the robot with three actuators. At (a) the robot is extending straight along the Y-axis, since extension speeds are the same. At (b) extension speed of the third tubing (v_3) is increased which causes the end effector to steer towards the opposite side l_{12} as shown.

4.2.2. Mechanical Design

The final prototype has a design similar to the preliminary prototype. Since weight of the robot also comes into play during motion in free space, several components are added to provide stiffness and prevent buckling failure of the tubings. The design consists of two main sections, much like the planar robot: (1) the robot body which includes the tubings, the backbone and the sheaths (see Figure 4.15a) and (2) the end-effector which includes the pinch-rollers and components attached to the tip such as the force sensor (see Figure 4.15b). In Figure 4.15a, solid arrows represent the point of extension for each extending component. It can be seen that the sheaths and the backbone extend from the base, whereas the tubings extend from the tip.

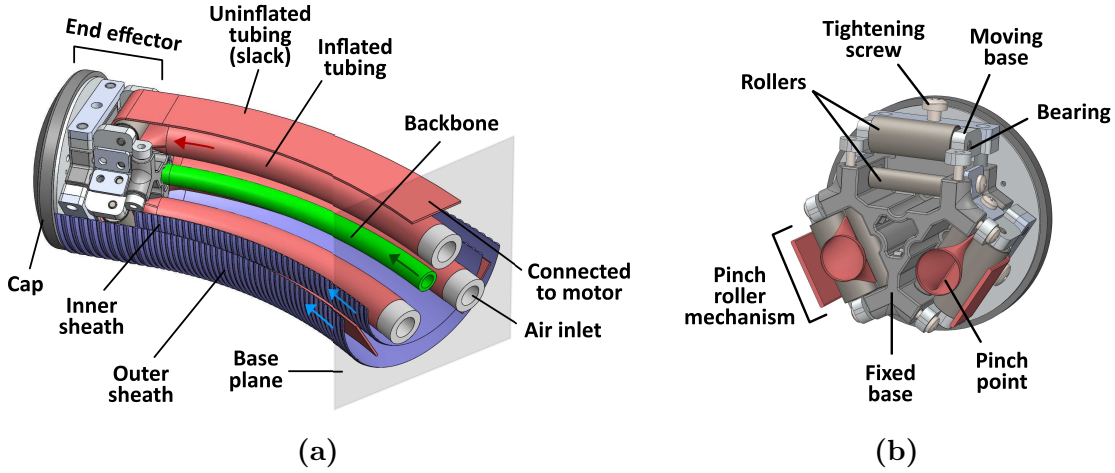

Figure 4.15. (a) Section view of the robot body. The inner and outer sheaths are shown in blue, backbone is in green and the tubings are in red. (b) Detailed view of the end-effector. Three pinch-roller drives are positioned with equal radial spacing around the centroid forming an equilateral triangle.

4.2.2.1. Robot Body. A colorized diagram of the robot body is given in Figure 4.15a. Components that did not exist in the preliminary prototype are the sheaths and the backbone. In 3D space, deflection of the robot body due to end effector weight comes into play, which was not an issue for the preliminary prototype. A hollow shaft that pases through the center of the robot body called the backbone (green) was added to provide structural support when the tubings are not pressurized. It extends from the base through the sheath reservoir and is supported by two PTFE bushings at both sides (see Figure 4.16). These bushings keep the backbone in alignment and minimize friction as it extends from the base.

Local buckling of the inflated tubings was a prominent issue during navigation tests of the planar robot (see Section 4.1.4.3). For this reason, an inner sheath (blue) was placed around the inflated tubings, covering both the tubings and the backbone. This sheath restricts radial tubing motion and prevents buckling failure of the inflated tubings. An outer sheath (blue) is also added to cover all components including the uninflated tubings (slack). The slack section will undergo tension when the tubing is pressurized from inlet and change shape depending on the location of the end effector. The outer sheath keeps the slack section in alignment along the robot body. Both

sheaths were designed to have very low weight, low friction and a very high extension ratio. They have a crimped structure that gives them the ability to extend or compress significantly during motion (see Section 4.2.3.2 for information on the manufacturing process). They are attached onto the end effector through a connector piece as shown in Figure 4.16. The sheaths are stored on the sheath reservoir which is fixed to the base plane. The tubings inlets are also fixed on the base plane (see Figure 4.16).

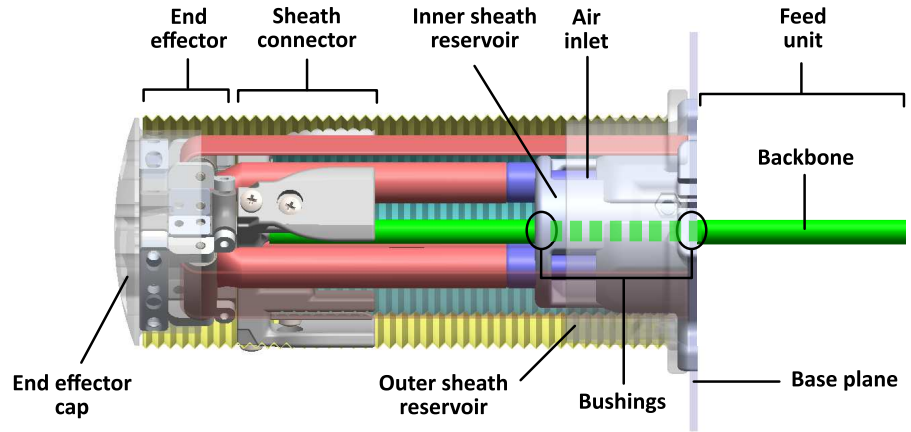

Figure 4.16. Colorized diagram of the robot body as seen from the side. Inner sheath is attached to the sheath connector. The backbone is fed through a hole at the center. Two bushings are located at each side for alignment. End effector cap and outer sheath reservoir are partially transparent to show interior components.

4.2.2.2. End Effector. Detailed diagram of the end effector and its interior components is given in Figure 4.17. The end effector includes an adjustment mechanism to fine-tune the tightness of each roller pair, similar to the one used in the end effector of the planar robot. The top roller is attached onto the corresponding moving base and the bottom roller is attached onto the end effector base for each roller pair. Unlike the planar robot, the rollers have different diameters, with the top roller being larger than the bottom roller. This was done to make assembly easier. The bottom roller can pass through the bearing housing due to its small diameter and the bearings can be attached from both sides during assembly.

The adjustment can be done by tightening or loosening the screws, thus changing the distance between end effector base and moving base. There are three tightening screws on each roller pair, two on one side and one on the other, to prevent bending or rotation of the moving base due to tubing pressure. Bearings are attached on both sides of the rollers to minimize friction and are fixed on the moving base with plate covers. Three brass inserts (M3) are located at the tip to attach the cap (see Figure 4.15b) or other components such as camera, gripper etc. Please note that the tool channels on the fixed base shown in Figure 4.17 were added to help the assembly of the force sensor from the other side.

Due to the increased importance of weight for the 3D application, the end effector was designed to be as small and compact as possible. For this reason, instead of using separate roller shafts like in the planar robot, bearings were attached directly onto the rollers using small pins at both ends.

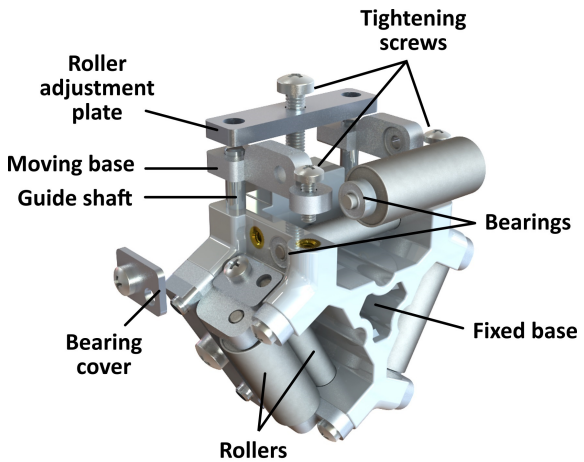

Figure 4.17. Exploded view of the end effector with interior components. The pinch-rollers and the adjustment mechanism for each roller pair is shown.

4.2.3. Components and Assembly

The assembled prototype can be seen in Figure 4.18. The robot has two main sections: the robot body which includes the end effector and the control hub. Control hub contains the feed unit (FU) and the air control unit (ACU).

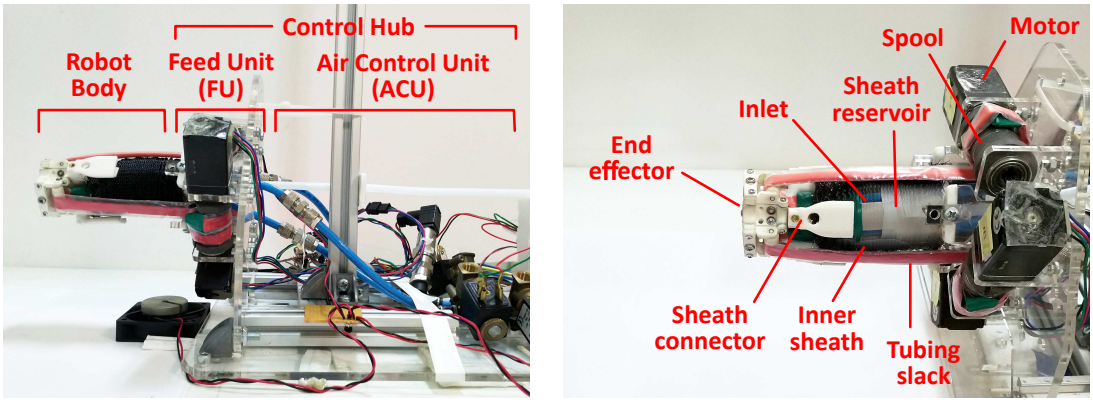

(a) **(b)**

Figure 4.18. Side view of the assembled robot. (a) Showing the three main sections, and (b) close up of the main parts in the robot body and the feed unit. The outer sheath and the end effector cap is not attached in both pictures and also (b) is edited to make inner sheath partially transparent to show interior components [49].

4.2.3.1. End Effector. The end effector is located at the tip of the robot body and houses the pinch-roller drives necessary to actuate the robot. All parts of the end effector were fabricated by a 3D printer for easy prototyping. The end effector parts are made of Polyamide (EOS PA 2200) similar to the end effector in the preliminary prototype (see Figure 4.19).

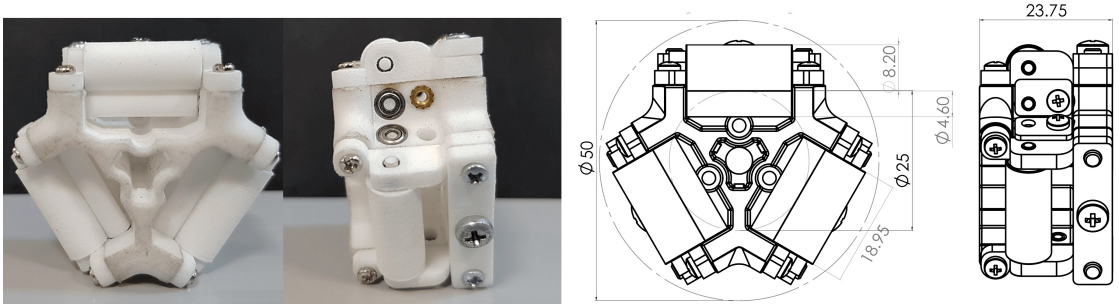

Figure 4.19. Back and side view of the end effector after assembly. The dimensions are given in mm [49].

4.2.3.2. Robot Body. The sheath connector which is attached to the tail end of the end effector and the end effector cap which is attached at the tip were also 3D printed. Polylactide (PLA) was chosen as the material since inflated tubings do not apply significant stress on the connector. The connector was manufactured as a separate part for easy assembly and disassembly of the inner/outer sheaths. The outer sheath and the cap are disassembled in Figure 4.18b to show interior parts of the robot body.

Tubings used in the robot body are LDPE/L type, with an LDPE outer layer and rubber latex inner layer. These tubings were also used for navigation tests with the planar robot (see Table 3.2 for specifications).

The inner and outer sheaths are made of polyester. Their crimped structure allows them to reach an extension ratio of 35:1 at full extension (see Figure 4.20). The outer sheath has a maximum outer diameter of 55 mm in compressed state whereas the inner sheath has a maximum outer diameter of 40 mm. The sheaths were manufactured in-house using a thermoforming process where off-the-shelf expandable braided sleevings were fitted onto a machined steel pipe with the desired outer diameter, compressed to the minimum length and heated at 350° C for 5 minutes.

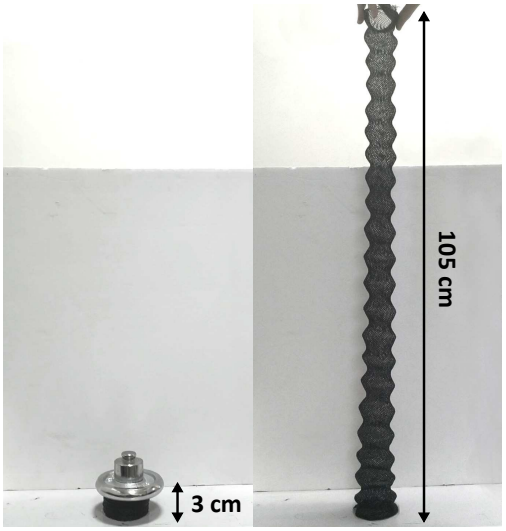

Figure 4.20. Both sheaths can extend significantly. The outer sheath has a compressed length of 3 cm and a maximum length of 105 cm.

A hollow flexible shaft with an outer diameter (OD) of 6 mm and inner diameter (ID) of 4 mm is used as the backbone. The backbone does not extend from the tip like the tubings and is instead pulled from the base by the force generated at the tip which causes the shaft to slide on the inflated tubings during motion. This applies additional shear stress on the tubings, increasing wear and tear while decreasing the output force. For this reason, PTFE was chosen as the shaft material to minimize friction force between the shaft and the inflated tubings. All components of the robot body, including the sheath connector, the sheath reservoirs and sheaths, the end-effector cap, and the tubings are shown in Figure 4.21.

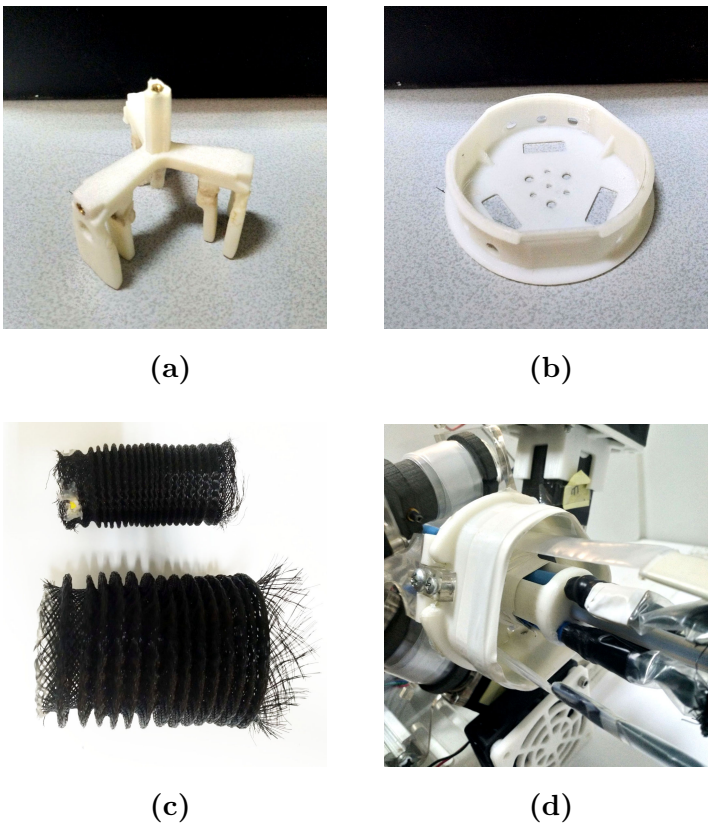

(a) **(b)**

(c) **(d)**

Figure 4.21. Components of the robot body. (a) The sheath connector, (b) the end effector cap, (c) inner and outer sheaths and (d) the inner and outer sheath reservoirs and the tubings.

4.2.3.3. Control Hub. Control hub contains all control elements including motors, motor drivers, sensors and solenoid valves. Control elements from the planar robot are also used in the final robot, with one more pneumatic line and motor for the added actuator. The control hub is divided into the FU and the ACU, much like the planar robot's control hub.

The FU houses all components necessary to control extension of the robot body (See Figure 4.18b). Three stepper motors are located in co-radial arrangement with equal spacing, aligned such that the uninflated tubings are positioned perpendicular to the base plane (see Figure 4.22). Each tubing is attached onto a spool that is fixed on the motor shaft with a flanged ball bearing at the other end for shaft alignment. A4983 microstep drivers (SparkFun Quadstepper) were used to control the motors [49]. Bearing housings and the base (see Figure 4.22) were laser cut from 5mm thick acrylic. Each bearing housing contains holes with embedded M5 hex nuts which allows them to be fixed onto the base using M5 pan-head screws. A sheath reservoir is located at the center of the FU which houses the inner and outer sheaths in compressed state. Dimensions and weights of the main parts in the robot body and the FU can be seen in Table 4.2. Weights are not given for parts in the FU since they are not inside the moving robot body.

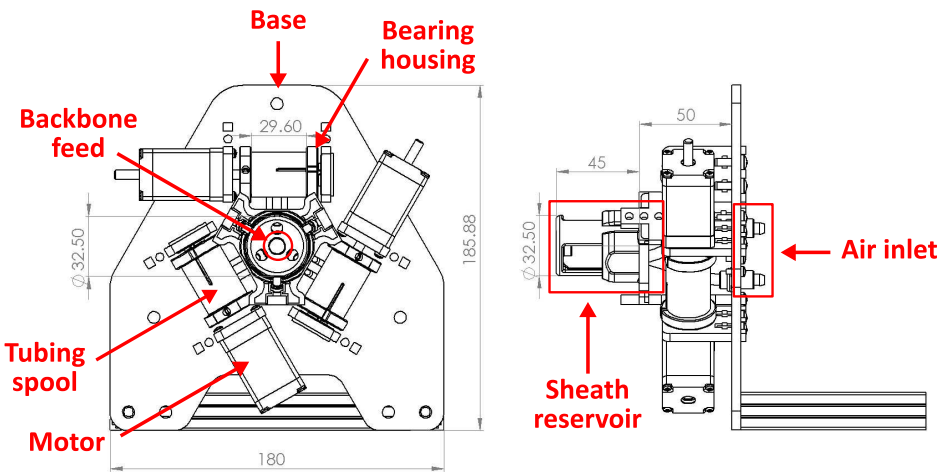

Figure 4.22. Dimensions of the feed unit (FU) in mm and its components. Please note that only the inner sheath reservoir is shown.

Table 4.2. Material, manufacturing method, dimension and weight of main components in the robot body and the FU.

	Material	**Manufacturing Method**	**Dimensions (mm)**		**Weight (g)**
Robot Body					
End effector	PA 12	SLS	OD = 50	L = 23.75	25
Inner Sheath	PET	Thermoforming	OD = 30 / 40	L_{min} = 30 / L_{max} = 350	2
Outer Sheath	PET	Thermoforming	OD_{max} = 55		2
Sheath Connector	PLA	FDM	OD_{max} = 54.5	L = 30	28
Backbone	PTFE	-	OD = 6 / ID = 4	L = 400	10
Feed Unit (FU)					
Sheath Reservoir	PLA	FDM	OD = 35	L = 40	–
Spools	PA 12	SLS	OD = 24	Width = 30	–
Base	Plexiglass	Laser cutting	Height = 186	Width = 180	–
Bearing Housing	Plexiglass	Laser cutting	Height = 45	Width = 30	–

The ACU is used to regulate the interior pressure of each tubing through PWM control using one inlet and exhaust valve and one pressure transmitter. Six solenoid valves and three pressure transmitters are used in total. All pneumatic lines are connected to an air compressor with pressure tank that acts as the pressure source (Figure 4.23). Technical specifications of all components in the control hub were given in Section 4.1.2.3, Table 4.1.

Figure 4.23. Pressurized tank with compressor that is used as the main pressure source.

4.2.3.4. Assembly Instructions. The components in the robot body have to be assembled in a specific order. In this section, assembly instructions for the robot body are given. Assembly steps are shown graphically in Figure 4.24. The steps are denoted as circled numbers for each component and arrows represent the direction in which the particular component is inserted. In addition, each step is described in detail in Figure 4.25. The assembled robot with all components can be seen in Figure 4.26.

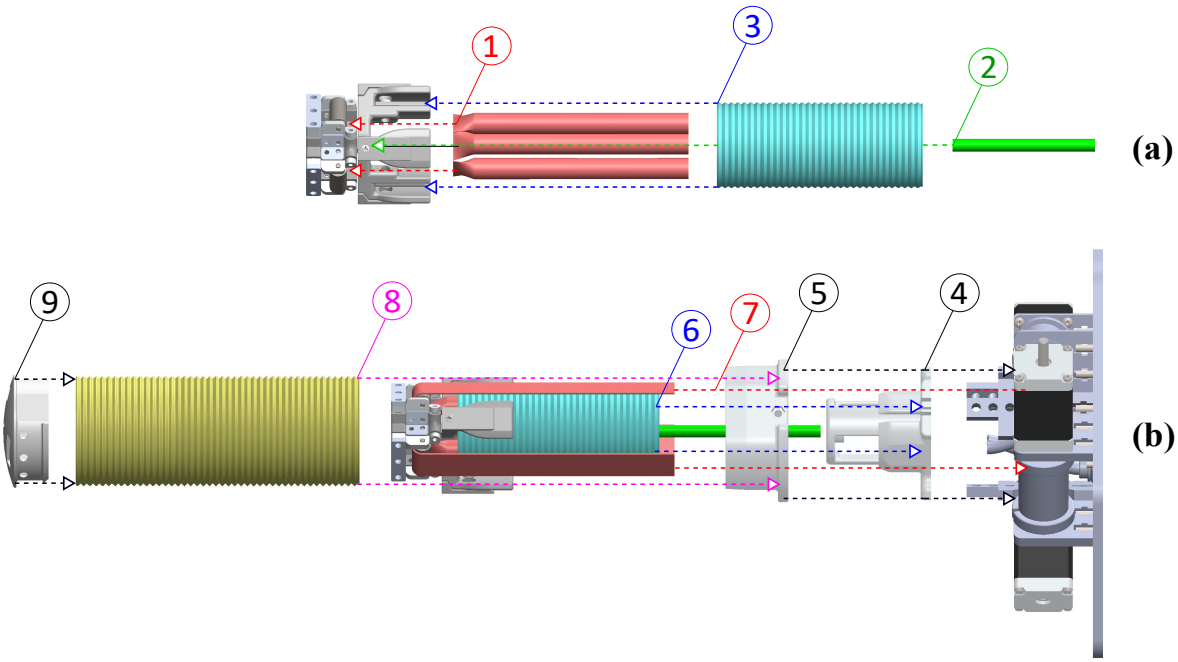

Figure 4.24. Assembly directions for (a) the inner sub-assembly and (b) for the final assembly of the robot body. Components are color coded as indicated: tubings (red), inner sheath (blue), outer sheath (yellow/purple), shaft (green), sheath reservoirs (white) and all other components are gray.

Sub-Assembly (a):

(1) The sheath connector is attached to the tail end of the end effector sub-assembly (this step is not shown). The tubings (red) are then passed through the pinch-rollers.

(2) The shaft (green) is attached to the sheath connector at the center.

(3) The inner sheath (blue) is attached to the sheath connector and is tightened using screws.

Final Assembly (b):

(4) The inner sheath reservoir is attached to the feed unit.

(5) The outer sheath reservoir is attached to the feed unit.

(6) Subassembly (a) is attached to the feed unit. First, inflated section of the tubings lying inside the inner sheath are attached to the inlet fixture on the inner sheath reservoir (4). Then, the inner sheath is placed on the inner sheath reservoir.

(7) The slack section of the tubings are attached to their respective tubing spools on the feed unit.

(8) The outer sheath is pulled over subassembly (a) and is placed on the outer sheath reservoir (5).

(9) The end effector cap is screwed to the tip of the end effector and the outer sheath (8) is attached to the cap (9).

Figure 4.25. Detailed instructions for each assembly step shown in Figure 4.24.

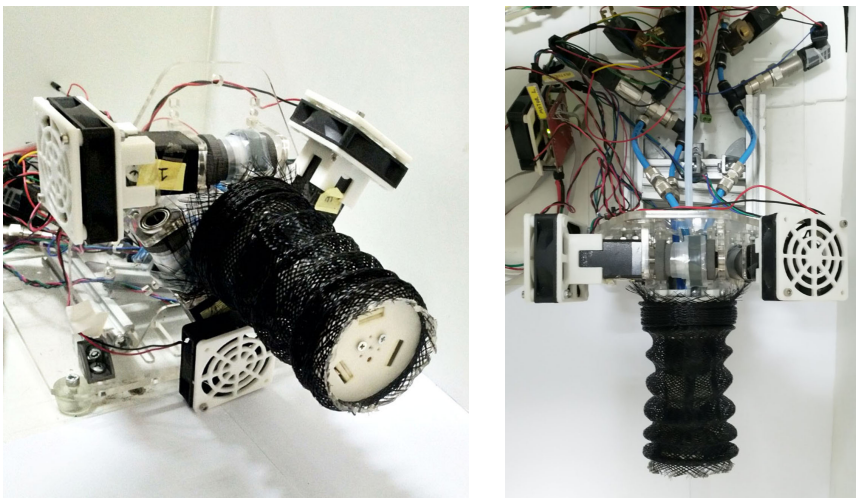

(a) **(b)**

Figure 4.26. (a) Front view of the assembled robot with outer sheath and the end effector cap. Fans used to prevent overheating of the stepper motors can also be seen. (b) Top view of the assembled robot. The backbone that is fed through the feed unit and the air control unit can be seen.

4.2.4. Experimental Methods

In this section, experimental methods used for performance testing and mechanical characterization of the robot are outlined. Force output and maximum speed tests were performed similar to actuator tests (Section 3.4). However since LDPE/L tubings were used in this system, all tests were performed with these tubings in the robot body. For this reason, maximum pressure range for all tests was between 0-160 kPa.

4.2.4.1. Bending Stiffness. Bending stiffness of the robot body was not important for the preliminary prototype since it was supported by a planar surface. However, stiffness becomes an important factor in 3D space as the robot has to resist deflection due to external forces and gravity. For this reason, an experiment was performed to evaluate bending stiffness of the robot body at different body lengths and pressures. The body lengths tested were 120, 170 and 210 mm, and the tubing pressures were chosen as 60, 100 and 140 kPa.

To obtain the force-deflection profile, an experimental setup was prepared where an ATI Nano 17 force/torque sensor was attached at the tip of a digital caliper (Mitutoyo) aligned perpendicular to the robot body (see Figure 4.27a). The deflection at the robot tip was increased in 2.5 mm increments until $\delta = 20$ mm, and in 5 mm increments after this point. The transverse reaction force exerted by the robot was measured using the sensor. A total of 5 repetitions were performed for each body length/pressure couple for deflections ranging from 0-40 mm.

4.2.4.2. Force Output. The maximum axial force exerted by the robot when extended straight at different tubing pressures was measured to characterize the force-pressure relationship and compare the results to the model. Axial force was measured using an ATI Nano 17 force/torque sensor attached at the robot tip (see Figure 4.27b). The tests were conducted in static configuration at steady-state with the tubing pressure increasing from 10 to 150 kPa in 10 kPa intervals. Force measurements were repeated 5 times at each pressure point. Also, to show the hysteresis in the pressure-force relation, another test was conducted by linearly increasing the pressure from 50 kPa to 150 kPa, then decreasing from 150 kPa to 50 kPa and then again increasing from 50 kPa to 150 kPa and measuring the force continuously during the test. Data from 5 trials were filtered and averaged to obtain a single hysteresis loop.

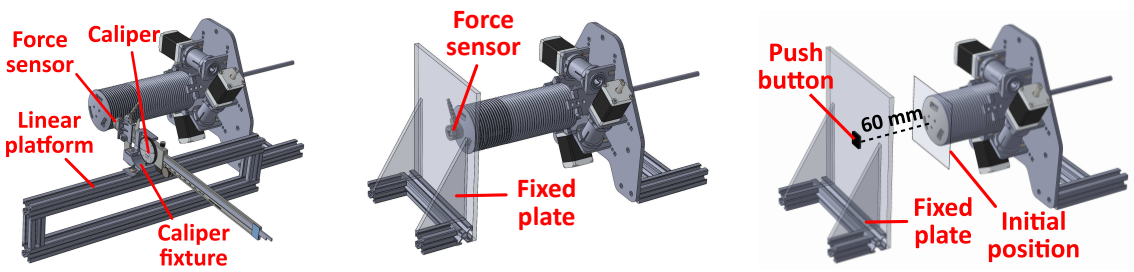

(a) (b) (c)

Figure 4.27. 3D model of the test setup used for (a) bending stiffness, (b) force output and (c) maximum speed experiments.

4.2.4.3. Maximum Speed. The speed limit of the robot tip was evaluated at different tubing pressures. To attain maximum speed, tubing slack was disconnected from the motors and average speed of the robot was calculated by measuring the travel time for a known distance. Similar to test setup prepared for speed experiments of the preliminary prototype, a push button was placed on a fixed plate 60 mm away from the initial position of the end effector and CompactRIO RTOS and FPGA were used together to measure the travel time with 1 ms resolution (see Figure 4.27c) [49]. The end effector was released after pressurizing the tubings and travel time was measured. The experiments were performed at random pressure points between 60 and 100 kPa. Pressure values higher than 100 kPa were not tested, because, unlike the other experiments, the tubings were not restricted by the motors and as such the robot was driven at very high speeds leading to wear and tear on the tubings and eventually perforation.

4.2.4.4. Workspace. A simple constant curvature (cc) kinematic model was used to estimate the robot's workspace [49]. First, the theoretical workspace was calculated using the cc-model. The theoretical model takes two system constraints into account, namely maximum length of the backbone (L_{max}) and minimum radius of curvature of the backbone (R_{min}). These were taken as L_{max}=300 mm and R_{min}=50 mm. According to the theoretical workspace, the robot should be able to operate roughly in a hemispherical volume centered at the base of the robot, constrained only by these two parameters. However, due to changing stiffness at different lengths and mechanical limitations resulting from buckling of the tubings, the maximum curvature of backbone changes with backbone length rather than being constant throughout the workspace. For this reason, we performed an experiment by driving the robot tip to 100 different goal coordinates inside the theoretical workspace and applied regression analysis to estimate the minimum radius of curvature (R_{min}) at each backbone length assuming the backbone profile has constant curvature ($R_{min} = f(L_b)$). The relative positioning error was calculated at each position using Equation 4.1. The kinematic model and calculation of the position error is discussed in detail by Talas [48].

$$E_{rel} = \ 100 \ \frac{\|\tilde{e}\|}{\|\tilde{p}\|} \tag{4.1}$$

In Eq. 4.1, $\tilde{p}^*$ is measured mean tip position vector, $\tilde{p}$ is goal position vector and $\tilde{e}$ is the error vector where $\tilde{e} = \tilde{p}^* - \tilde{p}$.

An Intel RealSense D435 depth camera (having integrated stereo camera, RGB module and infrared projector, with RMS depth error $\leq 2\%$) was used to track a colored circle-shaped marker at the robot tip at the initial and final locations. To evaluate the marker position in real-world coordinates, RGB and depth images taken with the camera were aligned and the RGB image was segmented to find the center pixel of the marker and extract the 3D position data from depth image. The 3D data was then converted into millimeters by measuring the distance between two fixed reference markers. Detailed information about the camera and depth conversion is given by Talas [48]. A total of 100 data points were taken at constant tubing pressure of 140 kPa.

4.2.4.5. Navigation. Multiple navigation experiments were performed to demonstrate the robot's ability to carry out tasks inside its workspace such as lifting and carrying weights, and navigating towards a predetermined goal position both in open field and around obstacles. The tip speed and steering angle of the robot was controlled manually using the Force Dimension omega.6 device [48]. Different obstacles were placed in the workspace to evaluate the robot's ability to operate in closed or cluttered environments.

4.2.5. Results

4.2.5.1. Bending Stiffness. Results of the bending stiffness experiments are presented in Figure 4.28 as force-deflection graphs. The standard deviation ($\pm\sigma$) for each regression curve is shaded. The force-deflection relationship is close to linear for small deflections (<5 mm) as expected from the uniform beam assumption. However, a decreasing trend for stiffness is observed at higher deflections. There are several reasons causing the uniform beam assumption to not hold for large deflections. One reason is that the distance between tubings changes due to applied force which affects the overall stiffness of the robot.

Another reason is the local buckling of the tubings causing deflection to be non-uniform through the body but local at some points, therefore lowering the transverse reaction force at the tip. Other than local buckling, full buckling of the tubings was observed at deflections larger than 25 mm at a body length of 130 mm which resulted in a sharp decline in stiffness. For this reason, values higher than 25 mm were omitted at 130 mm body length in Figure 4.28a.

Initial bending stiffness was calculated from slope of the regression curve at zero deflection ($\delta = 0$) for each body length/pressure couple. The results are summarized in Table 4.3.

Table 4.3. Initial bending stiffness (N/mm) at $\delta = 0$. Leftmost column indicates the body length and top row indicates the tubing pressure at which the experiment was performed.

	60 kPa	**100 kPa**	**140 kPa**
130 mm		0.129±0.013	
170 mm	0.066±0.002	0.082±0.006	0.088±0.008
210 mm		0.048±0.001	

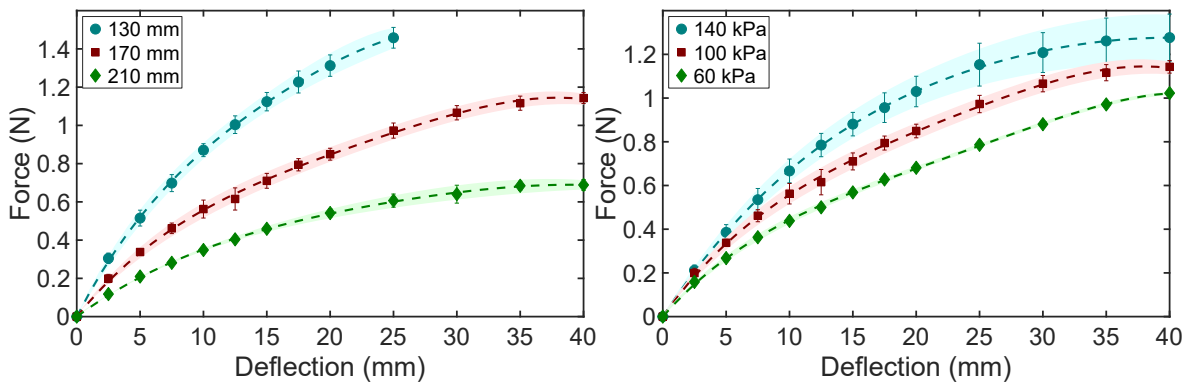

(a) **(b)**

Figure 4.28. Bending stiffness test results for (a) different lengths at 100 kPa tubing pressure (b) different pressures at 170 mm body length. Shaded areas show the standard deviation [49].

4.2.5.2. Force Output. For the final soft continuum robot, total force output (F_{total}) was simply estimated by calculating the force produced by a single actuator (F_{act}) using the model given in Section 3.2.1 and multiplying it by three since three actuators are used:

$$F_{total} = 3\,F_{act} \tag{4.2}$$

The static force test results given in Figure 4.29a show that the force output of the robot follows the model estimation, and is within the minimum and maximum model limits. For the pressures above 60 kPa, deviation of the force results is observed to be smaller which means pressures above 60 kPa are more appropriate to operate the robot since the force characteristics are more stable.

Mean absolute error (MAE) of the test data is calculated as 0.494 N and the root-mean-square error (RMSE) is 0.575 N when compared to model estimation. In general, measured force was lower than the model data, which can be explained by neglected or underestimated friction forces in the system (i.e. friction at the rollers and between the inflated and uninflated parts of the tubings). Maximum force exerted by the robot is measured to be 20.1±0.3 N at 150 kPa tubing pressure. This value is only limited by material characteristics of the tubings. Therefore, the force output can be higher than our current prototype by using tubings with greater burst pressure and durability.

Force data taken continuously while changing the pressure is given in Figure 4.29b. The pressure increase and decrease lines vary due to hysteresis in the system. Whereas this error is common in this type of pneumatic system, it does not significantly affect control of the robot since extension speeds of the actuators are not related to pressure. It may, however, affect stiffness and force output if precise control of these two parameters is required. Nevertheless, hysteresis can be modeled for cases where the pressure needs to be changed continuously during operation of the robot.

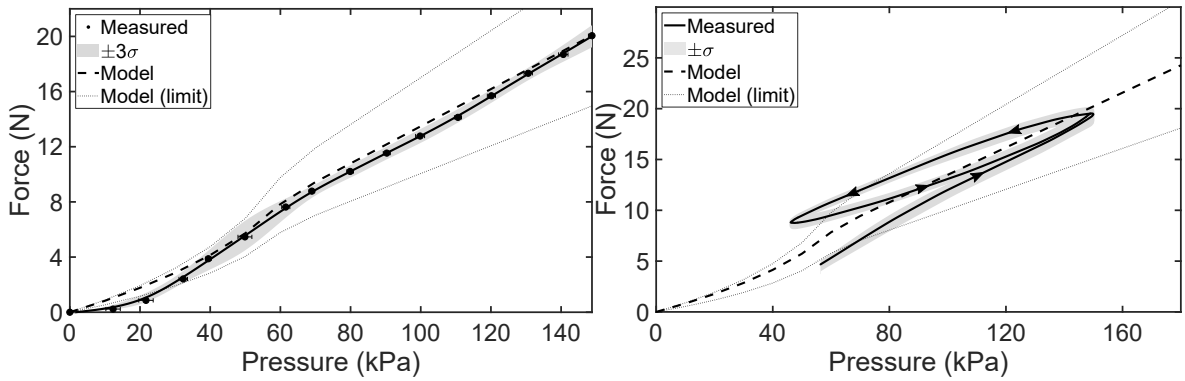

(a) **(b)**

Figure 4.29. Static force output test results taken (a) at steady state for discrete pressure values, and (b) while continuously changing the pressure. Shaded areas show the standard deviation. The model estimation is given as a dashed line (MS assumption). Maximum limit is obtained using the NS assumption and minimum limit is obtained using the FS assumption (see Section 3.2.1) [49].

4.2.5.3. Maximum Speed. Test results given in Figure 4.30 show the peak speed capability of the prototype when tubings are not restricted by the motors. As can be seen from the figure, static friction in the system is not completely overcome by force exerted by the tubings at pressures below 50 kPa, which causes a drastic decrease in speed and irregular motion during operation. The lowest and highest speed values measured were 543 mm/s at 55 kPa and 1490 mm/s at 100 kPa for the tests where roller friction is overcome.

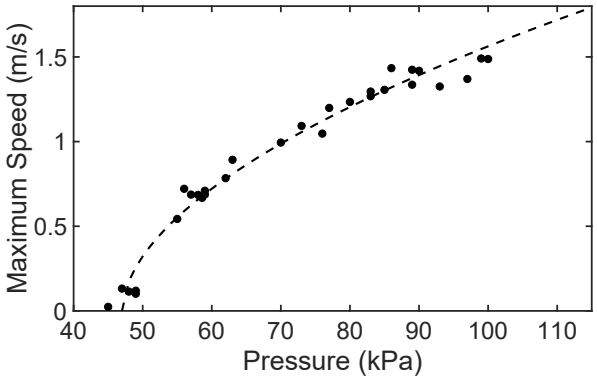

Figure 4.30. Results for maximum speed tests where tip speed is independent from motor speed [49].

4.2.5.4. Workspace. Data from position control experiments indicate that minimum radius of curvature (R_{min}) of the backbone increases with increasing backbone length (L_b) as expected. R_{min} for the system was found to follow the given equation for $0 < L_b < L_{max}$ where $L_{max} = 300$ mm.

$$R_{min} = 2.8894 \times 10^{-5} L_b^3 - 0.0118 L_b^2 + 1.9354 L_b \quad (4.3)$$
$$K_{max} = \frac{1}{R_{min}}$$

where K_{max} is the maximum backbone curvature.

The empirical workspace calculated using Eq. 4.3 is shown in Figure 4.31 in blue, and the theoretical workspace with fixed R_{min} of 50 mm is shown in red. Measured tip coordinates and their respective relative positioning errors (%) are also shown. Location of the fixed base frame and a 3D representation of the robot's empirical workspace are shown in Figure 4.32.

As seen in Figure 4.31, relative error increases at regions close to empirical workspace limits due to unstable behavior of the robot body. This instability is caused by local buckling of the tubings at high curvatures and tip deflection at high backbone lengths. Technically, the robot can also reach positions that are outside the empirical workspace (blue) but still inside the theoretical workspace (red). However, stable operation in these regions is not viable as controlling the robot tip becomes increasingly difficult due to tip deflection. The relative error was found to reach 25% at points close to the workspace boundary while ranging between 2.5% to 15% at interior regions close to the central Y-axis.

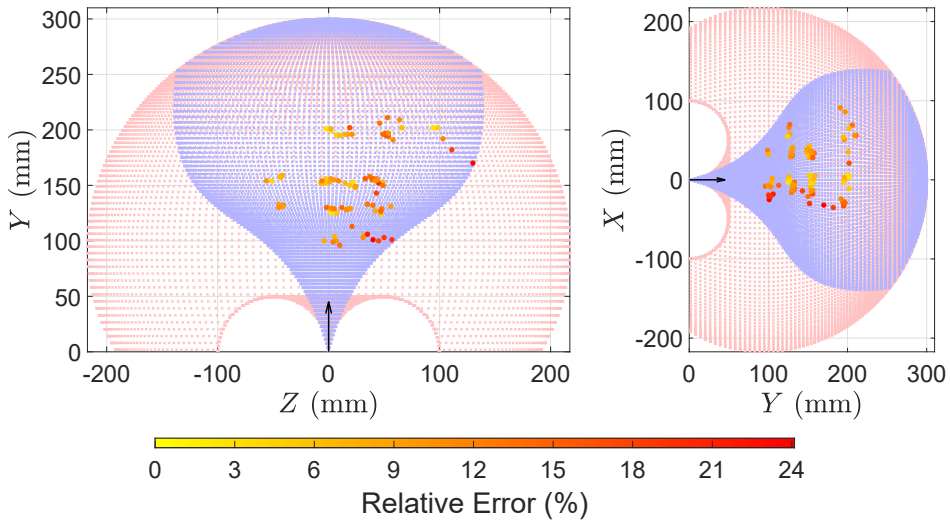

Figure 4.31. Empirical workspace (blue), theoretical workspace with fixed minimum radius of curvature (red) and measured tip locations from experiments. Color spectrum represents the relative positioning error (%) [49].

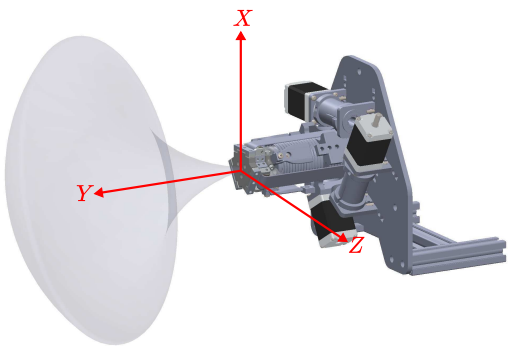

Figure 4.32. Location of the base frame (XYZ). Gray shaded volume represents the robot's empirical workspace.

4.2.5.5. Navigation. Figure 4.33 shows sequences of still-frame images taken from selected navigation experiments. During all experiments, the robot was controlled in real-time using omega.6 [48]. Figure 4.33a shows the robot approaching and lifting a weight using an attachment at the tip. Maximum weight lifted was 200 g or about 8 times the weight of the end effector (not shown in the figure).

Figure 4.33b shows the robot growing towards a target in open-field with no obstructions. Although the robot is not supported by the environment, it is able to maintain body stiffness and prevent sagging of the tip during growth.

More challenging trajectories are shown in Figures 4.33c and 4.33d. In Figure 4.33c, the robot is steered through an obstacle towards a target positioned at the upper left corner of the workspace. In Figure 4.33d, the robot is navigated through a tunnel towards the same target. Despite being constrained inside a tunnel that has an inner diameter (70 mm) close to the maximum outer diameter of the robot, the soft robot body can adapt to its surroundings and overcome friction to steer in the desired direction.

A similar task is shown in Figure 4.33e without the outer sheath, where the robot is steered inside a tunnel with higher curvature. The outer sheath, although important for retention of the tubing slack section, is not essential for movement and can be removed in cases where contact with the surroundings does not significantly affect the growth trajectory. The ability to provide active steering with fast response time is advantageous in scenarios where the robot tip must undertake sharp changes in extension speed or steering direction such as in Figure 4.33e.

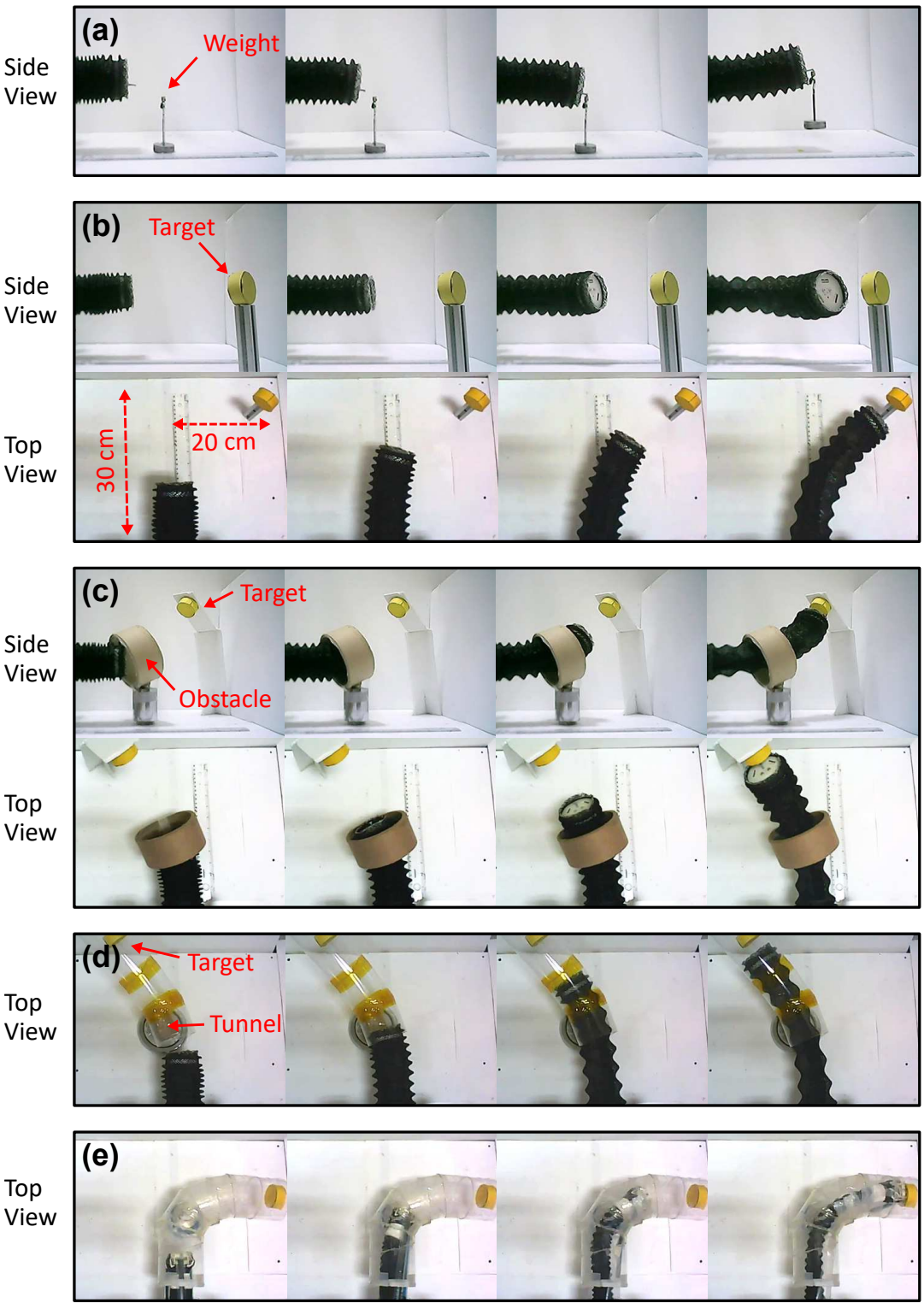

Figure 4.33. Snapshots taken from navigation experiments showing the robot trajectory with time (a) lifting a weight of 100 g (b) growing towards a target in open field (c) passing through an obstacle (d,e) navigating through closed tunnels. Note that the outer sheath is removed in the last image sequence [49].

5. DISCUSSION

Results obtained from the actuator experiments (Section 3.5) show that the proposed design works as expected with extension directly controlled by the motor instead of tubing pressure. Force test results show that the designed actuator can exert forces close to or higher than similar pneumatic actuators in the literature [13, 27, 32, 33, 38].

Results also indicate that tubing material, diameter and thickness have significant impact on actuator performance. Dimensions of the pinch-roller and roller friction also affect performance, but less than the tubing parameters. As such, the actuator performance can be improved further by manufacturing custom tubings with optimized design parameters using the guidelines given in Section 3.5 instead of using stock samples. The LDPE/L tubings used in the soft robot only have a burst pressure rating around 160 kPa. Considering the mostly linear relationship between force and pressure, the maximum stiffness, force and speed of the actuator can all be increased by improving durability of the tubing.

One of our claims was that the proposed design would allow simple and accurate control of extension by eliminating the effects of pressure. Controlled speed tests performed on the preliminary (planar) prototype show that accurate speed control is possible when applied to a robot. The mean absolute error between input and measured speed was 2.34 mm/s for extension and 1.70 mm/s for contraction at 100 kPa.

When incorporated in the final soft robot that can move in 3D space, the actuators were able to produce a maximum axial force of 20.1 N at 150 kPa tubing pressure, and a maximum speed of 1.49 m/s at 100 kPa using tubings with 10 mm OD (Section 4.2.5). The RMSE between measurement and model data is 0.575 N with measured force being slightly lower than model prediction which can be attributed to unanticipated friction losses in the system.

It can be said that the operation pressure of the final robot is between 60 and 140 kPa to obtain a continuous motion and prevent tubing failure, when all of the experimental results from Section 4.2.5 are taken into consideration. Pressure can also be used to change the tubing stiffness which can be useful in soft robotic applications. At 170 mm straight extension, maximum bending stiffness of the final robot was measured as 0.066 N/mm at 60 kPa and 0.088 N/mm at 140 kPa.

It is possible to change the dimensions of the robot body depending on intended applications. For instance, although the final prototype has a maximum length of 350 mm, its stroke can be increased by manufacturing actuators with longer tubings. This can be important for applications where long range navigation is required such as large-scale inspection of buildings. However, it should be noted that bending stiffness does decrease with increasing body length as expected. Although this did not affect navigation experiments, it can be a problem for applications that require extensions higher than 350 mm. In this case, a variable stiffness mechanism or an additional shell surrounding the body may be necessary.

Body size can also be decreased for applications such as minimally invasive surgery by reducing tubing diameter. A major consideration for scaling is the roughly square scaling law between tubing diameter and tip force ($F \propto D^2$) which can be derived from the model. According to this relationship, halving the tubing diameter will cause the output force to decrease roughly by a factor of 4. This loss can be compensated by increasing tubing pressure, assuming tubings have the necessary burst pressure. Similarly, increasing tubing diameter will lead to an exponential increase in output force so the robot can be navigated at lower pressures which may be safer for human interaction.

The developed actuator can be used in robotic applications that require the robot body to extend significantly such as closed area inspection, and search and rescue operations. Medical applications such as minimally invasive surgery, endoscopy or colonoscopy can be also be considered with downscaling.

6. CONCLUSION

In this study, a novel highly-extensible pneumatic actuator that extends from the tip has been designed and its application to a soft continuum robot has been demonstrated. It is believed that the proposed actuator can reach high extension ratios while providing accurate control of actuator speed and position due to the decoupling of pressure and extension. Firstly, a model of the actuator was developed. Then, a prototype of the actuator was manufactured, and experiments were performed to validate the model. Secondly, the actuator was used in two soft continuum robot prototypes, one that can move on a plane and one that can move in 3D space. Finally, experiments were performed on the robots to explore their mechanical characteristics and navigation capabilities. The results indicate that multiple actuators can be used to successfully navigate a tip-extending soft continuum robot. Speed test results show that controlling extension speed is possible with this design. The final prototype was able to reach a maximum extension speed of 1.49 m/s at 100 kPa. The maximum force exerted by the robot at the tip was measured as 20.1 N at 150 kPa.

6.1. Contributions and Originality

The originality of the proposed highly-extensible actuator lies mainly in the decoupling of pressure and motion. The design allows extension and contraction to be controlled using external motors while pressure is used to control stiffness and applied force, which is useful for real-time speed control. Another advantage is the ability to provide active steering by implementing multiple actuators in parallel. Although a maximum of three actuators were used in this study, four or more can be used in single or multisection continuum robot designs for increased dexterity and manipulation capability.

This study has led to several contributions to the literature. An article regarding the design and development of the actuator has been published in the journal Sensors

and Actuators: A [39] and presented as a conference paper in Türkiye Robotbilim Konferansı (ToRK) 2018. The design of the final soft robot prototype has been submitted as an article to the Soft Robotics journal [49] and presented in the "Eversion and Growing Soft Robots" workshop at the RoboSoft 2019 conference. Also, a quasi-static model for the soft robot has been proposed and submitted as an article to the International Journal of Robotics Research [50]. Both articles are currently in review. Finally, a soft robot design using the proposed actuator intended for colonoscopy application has been presented as a conference paper at the Hamlyn Symposium on Medical Robotics [51].

6.2. Outlook and Future Work

The highly-extensible actuator has certain advantages over similar designs in literature. However, it can be improved further by manufacturing custom-made tubings with optimized parameters instead of using stock samples. The pinch-roller drive can also be improved further by increasing the traction between tubing outer layer and roller to prevent slippage and minimizing frictional losses in the system. Different roller-tubing material combinations can be tested to see the effect on force output.

In the force model, the inner rubber layer was assumed to behave like a Hookean material to simplify the calculations. For better results, the inner layer should be modeled as a hyperelastic material. A Neo-Hookean model is suitable for strains in the range of 150% or the more general Mooney-Rivlin model can be used for strains higher than 200% [52]. Moreover, deformation of the outer layer can also be considered to improve the model even further. Polymeric materials exhibit viscoelastic behavior that may be more apparent during repeated use at different speeds.

Certain experiments can be improved and additional experiments can be performed to better characterize the actuator. For instance, friction between the carriage and the linear rail was not taken into account during actuator tests on the 1-DoF experimental setup. This friction force could have contributed to the experimental

data being lower than the model. During speed experiments, the initial acceleration time of the actuator from rest was not considered. To obtain better results, a high-speed camera or multiple photogate timers can be used to measure the instantaneous speed. When the actuator is operated at high speeds and pressures, the thin-walled tubings undergo significant stress especially on the outer surface at the pinch point between the rollers. If the actuator is to be commercialized, durability over extended use should also be determined. Experiments can be performed to quantify the lifetime of the actuator at different speeds and pressure ranges. For soft robotic applications in closed environments such as endoscopy, the forces applied on the robot body and the opposing reaction force applied by the robot become an important factor. These forces can be measured using a maze-like setup with embedded sensors. A model can also be developed to characterize the deformation and buckling failure of the tubings due to external forces at different curvatures.

The designed soft robot has issues with losing stiffness at high backbone length. Bulky components such as the sheath connector and the end effector cap can be eliminated to minimize the weight of the end effector, which would reduce deflection of the tip. As a future study, a variable stiffness mechanism using particle jamming [13], or a latch mechanism similar to the one used by Hawkes *et al.* [36] can be incorporated in the design. A design that incorporates helical springs wound around the tubings can also be considered to increase stiffness.

A major issue encountered during tests of the final prototype was local buckling of the tubings due to the tension force applied at the tip when the robot was retracted. This was especially prominent at high backbones lengths and it obstructed controlled contraction of the actuators. Increasing stiffness of the robot body and using high-precision pressure regulators to control tubing pressure could help prevent this issue. Another option could be to change the design altogether and include embedded micro-motors in the rollers as opposed to the base to eliminate the effects of slack tension.

REFERENCES

1. Grossard, M., N. Chaillet and S. Régnier, *Flexible Robotics: Applications to Multiscale Manipulations*, John Wiley & Sons, 2013.

2. Majidi, C., "Soft Robotics: A Perspective—Current Trends and Prospects for the Future", *Soft Robotics*, Vol. 1, No. 1, pp. 5–11, 2014.

3. Cianchetti, M., M. Calisti, L. Margheri, M. Kuba and C. Laschi, "Bioinspired locomotion and grasping in water: the soft eight-arm OCTOPUS robot", *Bioinspiration & biomimetics*, Vol. 10, No. 3, p. 035003, 2015.

4. Rus, D. and M. T. Tolley, "Design, fabrication and control of soft robots", *Nature*, Vol. 521, No. 7553, p. 467, 2015.

5. Robinson, G. and J. Davies, "Continuum robots-a state of the art", *IEEE International Conference on Robotics and Automation*, Vol. 4, No. May, pp. 2849–2854, 1999, `http://ieeexplore.ieee.org/xpls/abs_all.jsp?arnumber=774029`.

6. Burgner-Kahrs, J., D. C. Rucker and H. Choset, "Continuum Robots for Medical Applications: A Survey", *IEEE Transactions on Robotics*, Vol. 31, No. 6, pp. 1261–1280, dec 2015, `http://ieeexplore.ieee.org/document/7314984/`.

7. Ohno, H. and S. Hirose, "Design of slim slime robot and its gait of locomotion", *Proceedings 2001 IEEE/RSJ International Conference on Intelligent Robots and Systems. Expanding the Societal Role of Robotics in the the Next Millennium (Cat. No. 01CH37180)*, Vol. 2, pp. 707–715, IEEE, 2001.

8. McMahan, W., V. Chitrakaran, M. Csencsits, D. Dawson, I. D. Walker, B. A. Jones, M. Pritts, D. Dienno, M. Grissom and C. D. Rahn, "Field trials and testing of the OctArm continuum manipulator", *IEEE International Conference on Robotics and*

Automation, 2006. ICRA 2006., pp. 2336–2341, IEEE, 2006.

9. Ross, D., M. P. Nemitz and A. A. Stokes, "Controlling and Simulating Soft Robotic Systems: Insights from a Thermodynamic Perspective", *Soft Robotics*, Vol. 3, No. 4, pp. 170–176, dec 2016, https://www.liebertpub.com/doi/10.1089/soro.2016.0010.

10. Mehling, J., M. Diftler, M. Chu and M. Valvo, "A Minimally Invasive Tendril Robot for In-Space Inspection", *The First IEEE/RAS-EMBS International Conference on Biomedical Robotics and Biomechatronics, 2006. BioRob 2006.*, pp. 690–695, IEEE, 2006, http://ieeexplore.ieee.org/document/1639170/.

11. Webster, R. J., A. M. Okamura and N. J. Cowan, "Toward active cannulas: Miniature snake-like surgical robots", *IEEE International Conference on Intelligent Robots and Systems*, pp. 2857–2863, IEEE, 2006.

12. Mahl, T., A. Hildebrandt and O. Sawodny, "A variable curvature continuum kinematics for kinematic control of the bionic handling assistant", *IEEE transactions on robotics*, Vol. 30, No. 4, pp. 935–949, 2014.

13. Cianchetti, M., T. Ranzani, G. Gerboni, T. Nanayakkara, K. Althoefer, P. Dasgupta and A. Menciassi, "Soft Robotics Technologies to Address Shortcomings in Today's Minimally Invasive Surgery: The STIFF-FLOP Approach", *Soft Robotics*, Vol. 1, No. 2, pp. 122–131, jun 2014, https://www.liebertpub.com/doi/10.1089/soro.2014.0001.

14. Trivedi, D., C. D. Rahn, W. M. Kier and I. D. Walker, "Soft robotics: Biological inspiration, state of the art, and future research", *Applied Bionics and Biomechanics*, Vol. 5, No. 3, pp. 99–117, dec 2008, http://content.iospress.com/doi/10.1080/11762320802557865.

15. Laschi, C., M. Cianchetti, B. Mazzolai, L. Margheri, M. Fol-

lador and P. Dario, "Soft Robot Arm Inspired by the Octopus", *Advanced Robotics*, Vol. 26, No. 7, pp. 709–727, jan 2012, https://www.tandfonline.com/doi/full/10.1163/156855312X626343.

16. Hawkes, E. W., D. L. Christensen and A. M. Okamura, "Design and implementation of a 300% strain soft artificial muscle", *Proceedings - IEEE International Conference on Robotics and Automation*, Vol. 2016-June, pp. 4022–4029, 2016.

17. Digumarti, K. M., A. T. Conn and J. Rossiter, "Euglenoid-Inspired Giant Shape Change for Highly Deformable Soft Robots", *IEEE Robotics and Automation Letters*, Vol. 2, No. 4, pp. 2302–2307, 2017.

18. Abidi, H., G. Gerboni, M. Brancadoro, J. Fras, A. Diodato, M. Cianchetti, H. Wurdemann, K. Althoefer and A. Menciassi, "Highly dexterous 2-module soft robot for intra-organ navigation in minimally invasive surgery", *The International Journal of Medical Robotics and Computer Assisted Surgery*, Vol. 14, No. 1, p. e1875, feb 2018, http://www.ncbi.nlm.nih.gov/pubmed/29205769 http://doi.wiley.com/10.1002/rcs.1875.

19. Siciliano, B. and O. Khatib, *Springer handbook of robotics*, Springer, 2016.

20. Greigarn, T. and M. C. Çavuşoğlu, "Task-space motion planning of MRI-actuated catheters for catheter ablation of atrial fibrillation", *2014 IEEE/RSJ International Conference on Intelligent Robots and Systems*, pp. 3476–3482, IEEE, 2014.

21. Kim, Y.-J., S. Cheng, S. Kim and K. Iagnemma, "Design of a tubular snake-like manipulator with stiffening capability by layer jamming", *2012 IEEE/RSJ International Conference on Intelligent Robots and Systems*, pp. 4251–4256, IEEE, 2012.

22. Shepherd, R. F., F. Ilievski, W. Choi, S. A. Morin, A. A. Stokes, A. D. Mazzeo, X. Chen, M. Wang and G. M. Whitesides, "Multigait soft robot.", *Proceedings*

of the National Academy of Sciences of the United States of America, Vol. 108, No. 51, pp. 20400–3, dec 2011, http://www.ncbi.nlm.nih.gov/pubmed/22123978 http://www.pubmedcentral.nih.gov/articlerender.fcgi?artid=PMC3251082.

23. Kofod, G., W. Wirges, M. Paajanen and S. Bauer, "Energy minimization for self-organized structure formation and actuation", *Applied Physics Letters*, Vol. 90, No. 8, p. 081916, 2007.

24. Liu, Z. and P. Calvert, "Multilayer hydrogels as muscle-like actuators", *Advanced Materials*, Vol. 12, No. 4, pp. 288–291, 2000.

25. Bishop-Moser, J. and S. Kota, "Design and modeling of generalized fiber-reinforced pneumatic soft actuators", *IEEE Transactions on Robotics*, Vol. 31, No. 3, pp. 536–545, 2015.

26. Daerden, F. and D. Lefeber, "Pneumatic artificial muscles: actuators for robotics and automation", *European Journal of Mechanical and Environmental Engineering*, Vol. 47, No. 1, pp. 11–21, 2002.

27. Greer, J. D., T. K. Morimoto, A. M. Okamura and E. W. Hawkes, "Series pneumatic artificial muscles (sPAMs) and application to a soft continuum robot", *Proceedings - IEEE International Conference on Robotics and Automation*, pp. 5503–5510, 2017.

28. Gagnon, P. and P. LaForest, "Push actuator", US Patent 4,875,660, Oct. 24 1989.

29. Collins, F. and M. Yim, "Design of a spherical robot arm with the spiral zipper prismatic joint", *2016 IEEE International Conference on Robotics and Automation (ICRA)*, pp. 2137–2143, IEEE, 2016.

30. Mori, Y., H. Tsukagoshi and A. Kitagawa, "Flexible sliding actuator using a flat tube and its application to the rescue operation", *Robotics and Automation (ICRA), 2010 IEEE International Conference on*, pp. 3266–3272, IEEE, 2010.

31. Wakana, K., H. Namari, M. Konyo and S. Tadokoro, "Pneumatic flexible hollow shaft actuator with high speed and long stroke motion", *Robotics and Automation (ICRA), 2013 IEEE International Conference on*, pp. 357–363, IEEE, 2013.

32. Hammond, Z. M., N. S. Usevitch, E. W. Hawkes and S. Follmer, "Pneumatic Reel Actuator: Design, modeling, and implementation", *Robotics and Automation (ICRA), 2017 IEEE International Conference on*, pp. 626–633, IEEE, 2017.

33. Aliff, M., S. Dohta, T. Akagi and H. Li, "Development of a simple-structured pneumatic robot arm and its control using low-cost embedded controller", *Procedia Engineering*, Vol. 41, pp. 134–142, 2012.

34. Del Dottore, E., A. Sadeghi, A. Mondini, V. Mattoli and B. Mazzolai, "Toward Growing Robots: A Historical Evolution from Cellular to Plant-Inspired Robotics", *Frontiers in Robotics and AI*, Vol. 5, p. 16, mar 2018, http://journal.frontiersin.org/article/10.3389/frobt.2018.00016/full.

35. Walker, I. D., "Biologically inspired vine-like and tendril-like robots", *2015 Science and Information Conference (SAI)*, pp. 714–720, IEEE, jul 2015, http://ieeexplore.ieee.org/document/7237221/.

36. Hawkes, E. W., L. H. Blumenschein, J. D. Greer and A. M. Okamura, "A soft robot that navigates its environment through growth", *Science Robotics*, Vol. 2, No. 8, p. eaan3028, jul 2017, http://robotics.sciencemag.org/lookup/doi/10.1126/scirobotics.aan3028.

37. Dehghani, H., C. R. Welch, A. Pourghodrat, C. A. Nelson, D. Oleynikov, P. Dasgupta and B. S. Terry, "Design and preliminary evaluation of a self-steering, pneumatically driven colonoscopy robot", *Journal of Medical Engineering & Technology*, Vol. 41, No. 3, pp. 223–236, apr 2017, http://www.ncbi.nlm.nih.gov/pubmed/28122477 https://www.tandfonline.com/doi/full/10.1080/03091902.2016.1275853.

38. Yarbasi, E. Y. and E. Samur, "Design and evaluation of a continuum robot with extendable balloons", *Mechanical Sciences*, Vol. 9, No. 1, pp. 51–60, feb 2018, https://www.mech-sci.net/9/51/2018/.

39. Baydere, B. A., S. K. Talas and E. Samur, "A novel highly-extensible 2-DOF pneumatic actuator for soft robotic applications", *Sensors and Actuators A: Physical*, Vol. 281, pp. 84–94, 2018, https://linkinghub.elsevier.com/retrieve/pii/S0924424718308550.

40. Dowling, N. E., *Mechanical behavior of materials: engineering methods for deformation, fracture, and fatigue*, Pearson, 2012.

41. Ward, I. M., "The yield behaviour of polymers", *Journal of materials Science*, Vol. 6, No. 11, pp. 1397–1417, 1971.

42. Le Van, A. and C. Wielgosz, "Bending and buckling of inflatable beams: Some new theoretical results", *Thin-Walled Structures*, Vol. 43, No. 8, pp. 1166–1187, 2005.

43. Cowper, G., "The shear coefficient in Timoshenko's beam theory", *Journal of applied mechanics*, Vol. 33, No. 2, pp. 335–340, 1966.

44. Fichter, W., "A theory for inflated thin-wall cylindrical beams", *National Aeronautrics and Space Administration*, 1966, https://ntrs.nasa.gov/search.jsp?R=19660019922.

45. Comer, R. and S. Levy, "Deflections of an inflated circular-cylindrical cantilever beam", *AIAA journal*, Vol. 1, No. 7, pp. 1652–1655, 1963.

46. Ji, Q., C. Wang and H. Tan, "Multi-scale wrinkling analysis of the inflated beam under bending", *International Journal of Mechanical Sciences*, Vol. 126, pp. 1–11, 2017.

47. Tabor, D., "Friction, lubrication and wear", *Surface and colloid science*, Vol. 5, pp. 245–312, 1972.

48. Talas, S. K., *Control System Design of a Highly-Extensible Soft Continuum Robot*, Master's thesis, Bogazici University, 2019.

49. Talas, S. K., B. A. Baydere, T. Altinsoy, C. Tutcu and E. Samur, "Design and Development of a Growing Pneumatic Soft Robot", *Soft Robotics*, 2019, In Review.

50. Tutcu, C., B. A. Baydere, S. K. Talas and E. Samur, "Quasi-static Modeling of a Novel Growing Soft-Continuum Robot", *International Journal of Robotics Research*, 2019, In Review.

51. Altinsoy, T., B. A. Baydere, S. K. Talas and E. Samur, "Design of an Extensible Colonoscopy Robot", pp. 25–26, Hamlyn Symposium on Medical Robotics, 2018.

52. Marckmann, G. and E. Verron, "Comparison of hyperelastic models for rubber-like materials", *Rubber chemistry and technology*, Vol. 79, No. 5, pp. 835–858, 2006.

APPENDIX A: DATASHEETS

For datasheets of control elements (e.g. stepper motors, solenoid valves, pressure transmitters etc.), please refer to [48].

Manual, F/T Transducer Section
Document #9620-05-Transducer Section-24

5.3 Nano17 Specifications (Includes IP65/IP68 Versions)

5.3.1 Nano17 Physical Properties

Table 4.6—Nano17 Physical Properties

Single-Axis Overload	(US) Standard Units	(SI) Metric Units
Fxy	±56 lbf	±250 N
Fz	±110 lbf	±480 N
Txy	±14 inf-lb	±1.6 Nm
Tz	±16 inf-lb	±1.8 Nm
Stiffness (Calculated)		
X-axis & Y-axis forces (Kx, Ky)	4.7×10^4 lb/in	8.2×10^6 N/m
Z-axis force (Kz)	6.5×10^4 lb/in	1.1×10^7 N/m
X-axis & Y-axis torque (Ktx, Kty)	2.1×10^3 lbf-in/rad	2.4×10^2 Nm/rad
Z-axis torque (Ktz)	3.4×10^3 lbf-in/rad	3.8×10^2 Nm/rad
Resonant Frequency		
Fx, Fy, Tz	7200 Hz	7200 Hz
Fz, Tx, Ty	7200 Hz	7200 Hz
Physical Specifications		
Weight[1]	0.02 lb	0.00907 kg
Diameter[1]	0.669 in	17 mm
Height[1]	0.571 in	14.5 mm

Note:
1. Specifications include standard interface plates.

5.3.2 Nano17 IP65/IP68 Physical Properties

Table 4.7—Nano17 IP65/IP68 Physical Properties

Single-Axis Overload	(US) Standard Units	(SI) Metric Units
Fxy	±56 lbf	±250 N
Fz	±110 lbf	±480 N
Txy	±14 inf-lb	±1.6 Nm
Tz	±16 inf-lb	±1.8 Nm
Stiffness (Calculated)		
X-axis & Y-axis forces (Kx, Ky)	4.7×10^4 lb/in	8.2×10^6 N/m
Z-axis force (Kz)	6.5×10^4 lb/in	1.1×10^7 N/m
X-axis & Y-axis torque (Ktx, Kty)	2.1×10^3 lbf-in/rad	2.4×10^2 Nm/rad
Z-axis torque (Ktz)	3.4×10^3 lbf-in/rad	3.8×10^2 Nm/rad
Resonant Frequency		
Fx, Fy, Tz	2200 Hz	2200 Hz
Fz, Tx, Ty	2200 Hz	2200 Hz
Physical Specifications		
Weight[1]	0.09 lb	0.0408 kg
Diameter[1]	0.79 in	20.1 mm
Height[1]	0.873 in	22.2 mm

Note:
1. Specifications include standard interface plates.

Figure A.1. Technical specifications of ATI Nano17 force/torque sensor.

5.3.9 Nano17-E Transducer Drawing

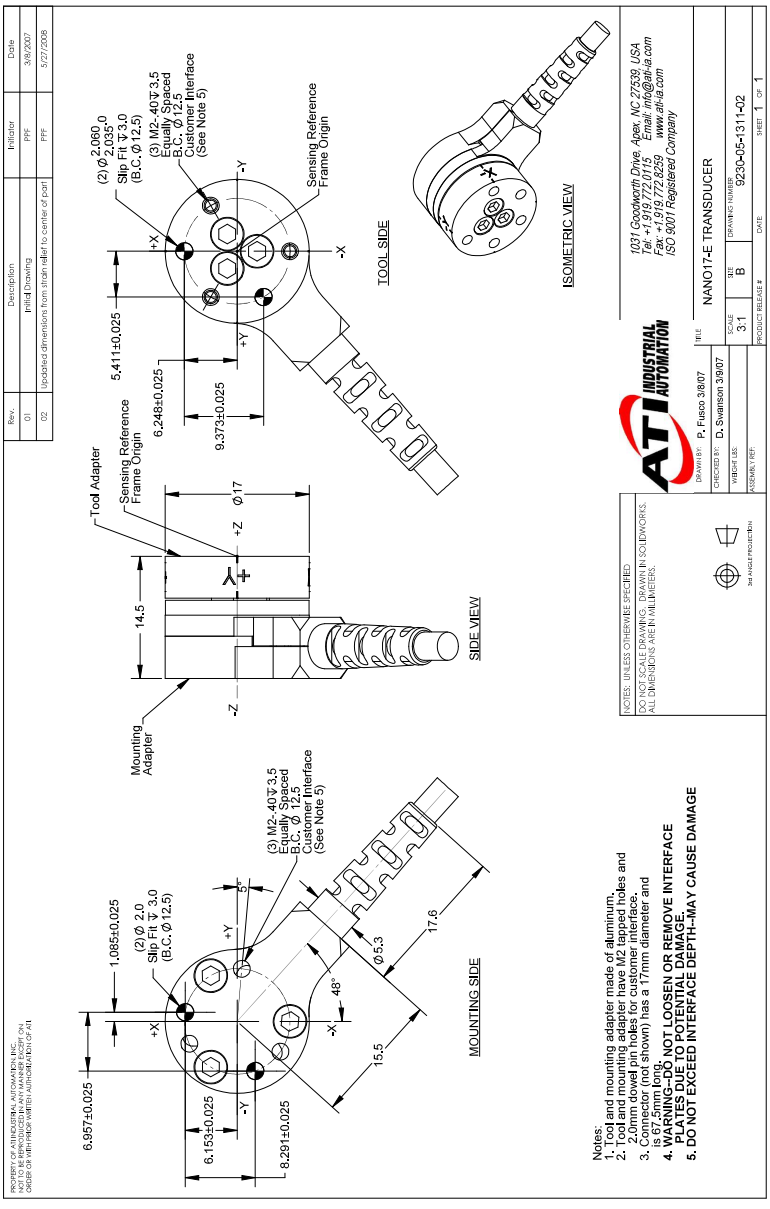

Figure A.2. Technical drawing of ATI Nano17 force/torque sensor.

Component	Subcomponent	Intel® RealSense™ Depth Camera D415	Intel® RealSense™ Depth Camera D435
Intel® RealSense™ Depth Module	Wide Stereo Imagers	X	√
	Standard Infrared Projector	√	X
	Wide Infrared Projector	X	√
	RGB color sensor	√	√

Table 2-2. Intel® RealSense™ Depth Camera D415 Mechanical Dimensions

Dimension	Min	Nominal	Max	Unit
Width		99		mm
Height		23		mm
Depth		20		mm
Mass		72		gr

Table 2-3. Intel® RealSense™ Depth Camera D435 Mechanical Dimensions

Dimension	Min	Nominal	Max	Unit
Width		90		mm
Height		25		mm
Depth		25		mm
Mass		72		gr

Figure 2-1. Intel® RealSense™ Depth Camera D415

Figure A.3. Technical specifications of Intel RealSense D435 depth camera.

Table 2-5. Depth Module SKU Properties

D400-Series Depth Cameras	Intel® RealSense™ Depth Camera D415	Intel® RealSense™ Depth Camera D435
Depth module	**Intel® RealSense™ Depth Module D415**	**Intel® RealSense™ Depth Module D435**
Baseline	55mm	50mm
Left/Right Imagers Type	Standard	Wide
Left/Right Imagers FOV (degrees)	H:69.4 / V:42.5/ D:77	H:91.2 / V:65.5 / D:100.6
IR Projector	Standard	Wide
IR Projector FOV	H:80 / V:55 /D:89.3	H:100.4/V:69/D:110.4
Color Sensor	OV2740	OV2740
Color Camera FOV	H:69.4 / V:42.5/ D:77	H:69.4 / V:42.5/ D:77
Depth Module Dimensions (mm)	X=83.7mm Y=10mm Z=4.7mm	X=70.7mm Y=14mm Z=10.53mm

H – Horizontal FOV, V – Vertical FOV, D – Diagonal FOV, X – Length, Y – Breadth, Z – Thickness

2.7.1 Left and Right Imagers

The Depth Module has two camera sensors referred here as stereo imagers, they are identical parts and are configured with identical settings. The imagers are labeled "left" and "right" from the perspective of the camera module looking outward. The stereo imager pairs are referred as Standard and Wide based on imager field of view.

Figure A.4. Properties of Intel RealSense D435 depth module.

DMS

YENİ ÜRÜN

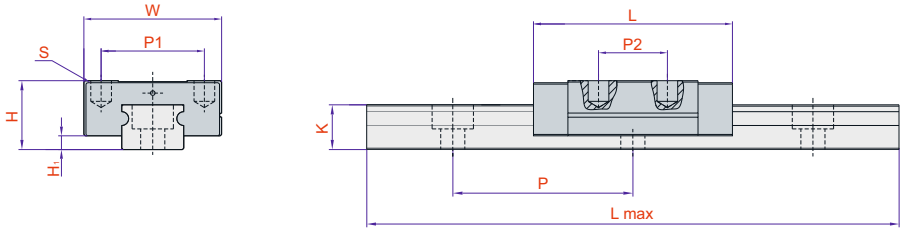

Ray KOD	Araba KOD	MODEL	Ürün Adı	H	H_1	K	P1	P2	P	L	S	W	Statik Kg	Dinamik Kg
4.004.01.07.06	4.004.02.07.06	DMN-07	Minyatür Lineer Araba	8	1.5	4.8	12	8	15	22.5	M2x2.5	17	10	8
4.004.01.09.06	4.004.02.09.06	DMN-09	Minyatür Lineer Araba	10	2	6.5	15	10	20	28.9	M3x3	20	20	15
4.004.01.12.06	4.004.02.12.06	DMN-12	Minyatür Lineer Araba	13	3	8	20	15	25	34.7	M3x3.5	27	32	27
4.004.01.15.06	4.004.02.15.06	DMN-15	Minyatür Lineer Araba	16	4	10	25	20	40	42.1	M3x4	32	45	37

L max: DMN-07 - 700 mm
DMN-09 - 1.000 mm
DMN-12 - 1.600 mm
DMN-15 - 1.600 mm

Tercih Edildiği Yerler

Minyatür seriler, yüksek pozisyon konumlama hassasiyeti ihtiyacı olan uygulamalarda tercih edilmektedir. Yük taşıma kapasiteleri düşüktür. Genellikle dikiş makinaları , medikal cihazlar, ofis makinaları , elektronik kart dizgi makinalarının üretimlerinde tercih edilmektedir.

Figure A.5. Technical specifications of the DMN09 miniature linear guide rail used in the 1-DoF experimental setup (mm).

Properties				Grilamid non-reinforced ▪ only in black 9363							
				Grilamid L 16 LM	Grilamid L 20 G ▪	Grilamid L 20 HL	Grilamid L 20 LM	Grilamid L 20 H FR	Grilamid L 25	Grilamid L 25 H
Mechanical properties										
Tensile E-modulus	(1 mm/min)	ISO 527	MPa	cond.	1100	1100	1100	1100	1500	1100	1100
Tensile strength at yield	(50 mm/min)	ISO 527	MPa	cond.	45	40	40	40	40	40	40
Elongation at yield	(50 mm/min)	ISO 527	%	cond.	15	12	12	12	10	12	12
Tensile strength at break	(50 mm/min)	ISO 527	MPa	cond.	50	50	50	50	35	50	50
Elongation at break	(50 mm/min)	ISO 527	%	cond.	>50	>50	>50	>50	>50	>50	>50
Impact strength	(Charpy, 23 °C)	ISO 179/1eU	kJ/m²	cond.	>100	>100	>100	>100	>100	>100	>100
Impact strength	(Charpy, -30 °C)	ISO 179/1eU	kJ/m²	cond.	>100	>100	>100	>100	>100	>100	>100
Notched impact strength	(Charpy, 23 °C)	ISO 179/1eA	kJ/m²	cond.	7	7	4	4	7	10	10
Notched impact strength	(Charpy, -30 °C)	ISO 179/1eA	kJ/m²	cond.	6	6	3	3	6	7	7
Shore-D hardness		ISO 868	-	cond.	70	70	70	70	72	70	70
Thermal properties											
Melting point	(DSC)	ISO 11357	°C	dry	178	178	178	178	178	178	178
Heat deflection temperature HDT/A	(1.80 MPa)	ISO 75	°C	dry	50	45	45	50	50	45	45
Heat deflection temperature HDT/B	(0.45 MPa)	ISO 75	°C	dry	125	115	115	125	130	115	115
Heat deflection temperature HDT/C	(8.00 MPa)	ISO 75	°C	dry	*	*	*	*	*	*	*
Thermal expansion coefficient long.	(23–55°C)	ISO 11359	10^{-4}/K	dry	1.2	1.2	1.2	1.2	0.9	1.2	1.2
Thermal expansion coefficient trans.	(23–55°C)	ISO 11359	10^{-4}/K	dry	1.4	1.4	1.4	1.4	1.2	1.4	1.4
Max. working temperature	long term	ISO 2578	°C	dry	90-110	90-110	90-110	90-110	90-110	80-100	100-120
Max. working temperature	short term	ISO 2578	°C	dry	150	150	150	150	150	150	150
Electrical properties											
Dielectric strength		IEC 60243-1	kV/mm	cond.	32	32	32	32	34	32	32
Comparative tracking index	CTI	IEC 60112	—	cond.	600	600	550	600	600	600	600
Volume resistivity		IEC 60093	Ω · m	cond.	10^{11}	10^{11}	10^{11}	10^{11}	10^{12}	10^{11}	10^{11}
Surface resistivity		IEC 60093	Ω	cond.	10^{12}	10^{12}	10^{12}	10^{12}	10^{12}	10^{12}	10^{12}
General properties											
Density		ISO 1183	g/cm³	dry	1.01	1.01	1.01	1.01	1.05	1.01	1.01
Flammability (UL 94)	(0.8 mm)	ISO 1210	rating		HB	HB	HB	HB	V2	HB	HB
Water absorption	(23 °C/sat.)	ISO 62	%		1.5	1.5	1.5	1.5	1.4	1.5	1.5
Moisture absorption	(23 °C/50 % r.h.)	ISO 62	%		0.7	0.7	0.7	0.7	0.7	0.7	0.7
Processing properties											
Linear mould shrinkage	long.	ISO 294	%	dry	0.80	0.80	0.80	0.80	0.55	-	-
Linear mould shrinkage	trans.	ISO 294	%	dry	0.85	0.85	0.85	0.85	0.75	-	-
Nomenclature		ISO 1874-1			PA12, EHLS, 14-210LN	PA12, MHR, 18-210	PA12, EHL, 18-210	PA12, MHR, 18-210	PA12, MHR, 18-210	PA12, MHR, 18-010	PA12, EHL 24-210

Text values «conditioned» were obtained using test pieces stored according to ISO 1110.

* not relevant as per CAMPUS 4.1

Figure A.6. Material datasheet for PA12 layer of the PA12/L tubing (Grilamid L25).

Overview of materials for Low Density Polyethylene (LDPE), Sheet/Profile extrusions

Categories: Polymer; Thermoplastic; Polyethylene (PE); Low Density (LDPE); Low Density Polyethylene (LDPE), Sheet/Profile extrusions

Material Notes: This property data is a summary of similar materials in the MatWeb database for the category "Low Density Polyethylene (LDPE), Sheet/Profile extrusions". Each property range of values reported is minimum and maximum values of appropriate MatWeb entries. The comments report the average value, and number of data points used to calculate the average. The values are not necessarily typical of any specific grade, especially less common values and those that can be most affected by additives or processing methods.

Vendors: **Click here to view all available suppliers for this material.**

Please click here if you are a supplier and would like information on how to add your listing to this material.

Physical Properties	Metric	English	Comments
Density	0.919 - 0.930 g/cc	0.0332 - 0.0336 lb/in³	Average value: 0.922 g/cc Grade Count:5
Melt Flow	1.00 - 6.00 g/10 min	1.00 - 6.00 g/10 min	Average value: 2.90 g/10 min Grade Count:5

Mechanical Properties	Metric	English	Comments
Hardness, Shore D	50.0 - 55.0	50.0 - 55.0	Average value: 51.7 Grade Count:3
Tensile Strength, Ultimate	11.0 - 14.0 MPa	1600 - 2030 psi	Average value: 12.5 MPa Grade Count:4
Tensile Strength, Yield	10.0 - 14.0 MPa	1450 - 2030 psi	Average value: 11.2 MPa Grade Count:4
Elongation at Break	500 - 600 %	500 - 600 %	Average value: 533 % Grade Count:3
Modulus of Elasticity	0.221 - 0.483 GPa	32.1 - 70.1 ksi	Average value: 0.315 GPa Grade Count:3

Thermal Properties	Metric	English	Comments
Vicat Softening Point	90.0 - 107 °C	194 - 225 °F	Average value: 96.0 °C Grade Count:3

Figure A.7. Material properties for LDPE layer of the LDPE/L tubing.

22.07.2019 Specification - 148-0078

Nordson MEDICAL
29 Northwestern Drive
Salem, NH 03079
MAIN:603.327.0600
EMAIL:VTN-customerservice@nordsonmedical.com

ENGINEERED SHAFT ITEM NUMBER: 148-0078

Dark Gray Pebax® Medical Tubing, ID 0.221", OD 0.231", Len 55"

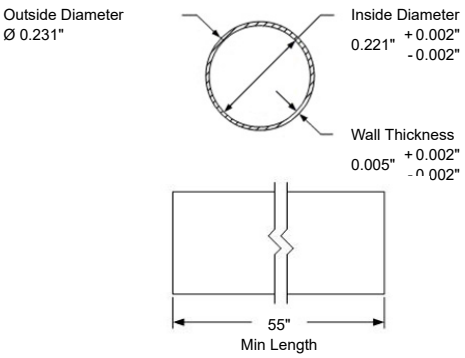

Drawing not to scale.

Product Description		
Item Number	148-0078	
Type	Shaft, Single Lumen	
Inner Diameter	0.221"	+ 0.002"
		- 0.002"
Wall Thickness	0.005"	+ 0.002"
		- 0.002"
Outer Diameter	0.231" Ref	
Min Length	55"	
Color	Dark Gray	
Material	Pebax®	
Durometer	55D	
Notes	All pigments comply to the requirements set forth by the FDA 21 CFR Part 73 Subpart D List.	

Figure A.8. Technical specifications of the PB55 tubing (inches).

Nordson MEDICAL
29 Northwestern Drive
Salem, NH 03079
MAIN:603.327.0600
EMAIL:VTN-customerservice@nordsonmedical.com

ENGINEERED SHAFT ITEM NUMBER: 148-0104

Purple Pebax® Medical Tubing, ID 0.221", OD 0.231", Len 55"

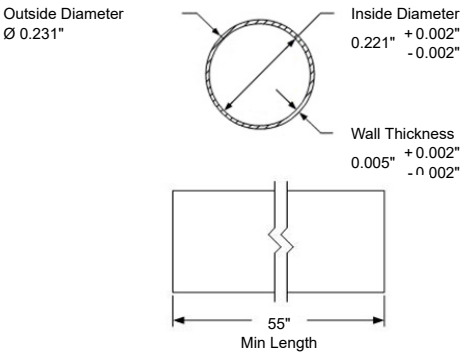

Drawing not to scale.

Product Description		
Item Number	148-0104	
Type	Shaft, Single Lumen	
Inner Diameter	0.221"	+ 0.002"
		- 0.002"
Wall Thickness	0.005"	+ 0.002"
		- 0.002"
Outer Diameter	0.231" Ref	
Min Length	55"	
Color	Purple	
Material	Pebax®	
Durometer	72D	
Notes	All pigments comply to the requirements set forth by the FDA 21 CFR Part 73 Subpart D List.	

Figure A.9. Technical specifications of the PB72 tubing (inches).

22.07.2019 Specification - 115-1809

Nordson MEDICAL
29 Northwestern Drive
Salem, NH 03079
MAIN:603.327.0600
EMAIL:VTN-customerservice@nordsonmedical.com

MEDICAL TUBING ITEM NUMBER: 115-1809

Natural Polyurethane Medical Tubing, ID 0.16", Wall 0.01", Len 0"

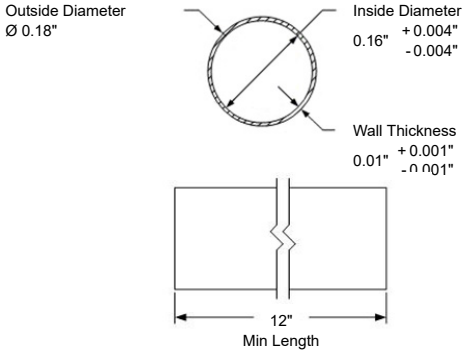

Drawing not to scale.

Product Description		
Item Number	115-1809	
Type	Single Lumen	
Lumens	1	
Inner Diameter	0.16"	+ 0.004"
		- 0.004"
Wall Thickness	0.01"	+ 0.001"
		- 0.001"
Outer Diameter	0.18" Ref	
Min Length	12"	
Color	Natural	
Material	Polyurethane	
Durometer	80A	

Figure A.10. Technical specifications of the PEL tubing (inches).

Sub-Lite-Wall®

Ultra Thin Dimension Extrusion

EXTRUSIONS

Custom Sizes Available

OVERVIEW

Zeus Sub-Lite-Wall® tubing is PTFE tubing with wall thicknesses down to 0.001" and tolerances of ± 0.0005"(0.0127 mm) available in most sizes. Sub-Lite-Wall® tubing is available in both regular and extended micro-miniature dimensions and heat shrink versions.

We produce Sub-Lite-Wall® tubing where the inside diameter, outside diameter and wall thicknesses are uniform throughout. You can define your own specifications with the assurance that Zeus can meet your requirements completely in either an extruded or heat shrink version.

We produce Sub-Lite-Wall® tubing where the inside diameter, outside diameter, and wall thicknesses are uniform throughout.

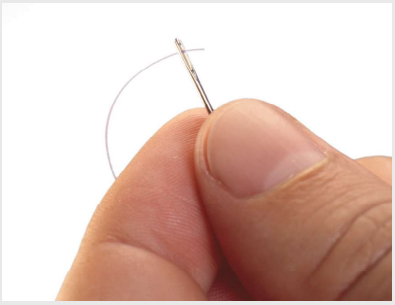

SECONDARY/VALUE-ADD SERVICES:

Custom Etching
Striping *(Spiral)*

COEFFICIENT OF FRICTION | CHEMICAL RESISTANCE | FLAME RESISTANCE

APPLICATIONS

- *Catheter lead delivery*
- *Introducer sheaths*
- *Baloon and stent protectors*
- *Endoscopy*
- *Dental*
- *Batteries*
- *Sensors*
- *Fiber optics*
- *HPLC*

CAPABILITIES AND SIZING

- *Etching available for bonding*
- *Ultra-tight tolerances*
- *Heat shrink*
- *Available in PTFE, FEP, PFA, and PEEK*
- *Customization available*

KEY PROPERTIES

- *Uniform inside and outside diameters*
- *Extremely small wall thickness*
- *Multiple sterilization options*
- *Very lubricious*
- *Working temperature range from 500 °F (260 °C) to -328 °F (-200 °C)*
- *Excellent dielectric insulation properties*
- *Flame resistant: UL 94 V-0*

ZEUS® PERFORMANCE EXTRUSIONS.

zeusinc.com

PTFE SLW ETCH .303 ID

Material PTFE
Inner Diameter (Min. Expanded Inner Diameter) .303 +.0025 - .0025
Wall .005 +.002 -.002
Color Natural
Cut Length 60 +2 -.000
Product Extruded Special Etch
Special Instructions VSL

Figure A.11. Technical specifications of the PTFE tubing (inches).

GENERAL PURPOSE

Wire & Cable Protection Solutions

Braided Sleeving Data Sheet

HellermannTyton

PET Expandable Braided Sleeving

(polyethylene terepthalate)

A general purpose and economical braided sleeving with good abrasion and cut resistance properties.

Application: Flexible, lightweight and durable, PET's construction easily expands over a variety of cable assembly shapes and sizes. PET performs well in abrasive applications. Use whenever flame retardancy and durability are primary concerns.

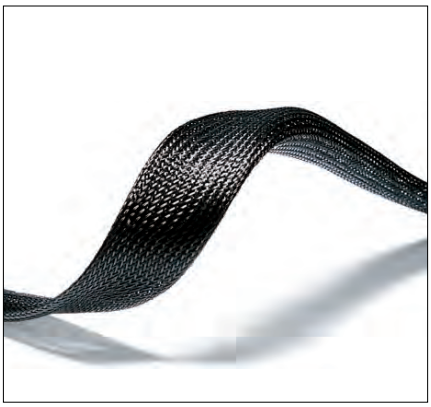

Series: BSP

Physical Properties	
Material	PET
Monofilament Thickness (ASTM D-204)	0.010
Flammability Rating	UL-94
Recommended Cutting	Hot Knife
Colors*	Black
Wall Thickness	0.025
Tensile Strength - Yarn (ASTM D-2265) lbs	7.5
Abrasion Resistance	Medium
Specific Gravity	1.38
Moisture Absorption % (ASTM D-570)	0.1 - 0.2

**Additional colors available upon request.*

Hard Vacuum Data (ASTM e-595 at 10-5 torr)	
TML	0.19
CVCM	0.00
WVR	0.16
Smoke D-Max (ASTM E662)	56
Outgassing	Medium
Oxygen Index (ASTM D-2863)	21

Operating Temperatures	
Minimum Continuous	-94°F / -70°C
Maximum Continuous (MIL-I-23053)	257°F / 125°C
Melt (ASTM D-2117)	482°F / 250°C

Chemical Resistance	
1 = No Effect 2 = Little Effect 3 = Affected 4 = More Affected 5 = Severely Affected	
Aromatic Solvents	2
Chlorinated Solvents	3
Strong Bases	2
Hydraulic Fluid (MIL-H-5606)	1
De-Icing Fluids (MIL-A-8243)	1
Strong Oxidants	2
UV Light	1
Fungus (ASTM G-21)	1
Alipahtic Solvents	1
Weak Bases	1
Salt Water (O-S-1926)	1
Lubricating Oil (MIL-A-8243)	1
Strong Acids	3
Esters/Keystones	1
Petroleum	1
Salts	1

Certifications	
Halogen Free	Yes
SVHC	None
ROHS	Yes
UL/CSA	Yes

Warranty Policy HellermannTyton products are warranted to be free from defects in material and workmanship at the time sold by us; but our obligation under this warranty and that of the seller is limited to the replacement of the product, and neither we nor the seller are bound by any other warranty, expressed, implied or statutory. Under no circumstances are we or the seller liable for any loss, damage, expenses or consequential damages of any kind arising out of the use or inability to use these products. All are sold with the understanding that the user will test them in actual use and determine their adaptability for the intended uses. Every effort is made to ensure accuracy and completeness when describing the technical properties of these products.

For product information visit **www.hellermann.tyton.com** or call **800.537.1512**

Figure A.12. Material datasheet of the expandable braided tubing used to manufacture the inner and outer sheaths for the final (3D) prototype.

APPENDIX B: TECHNICAL DRAWINGS

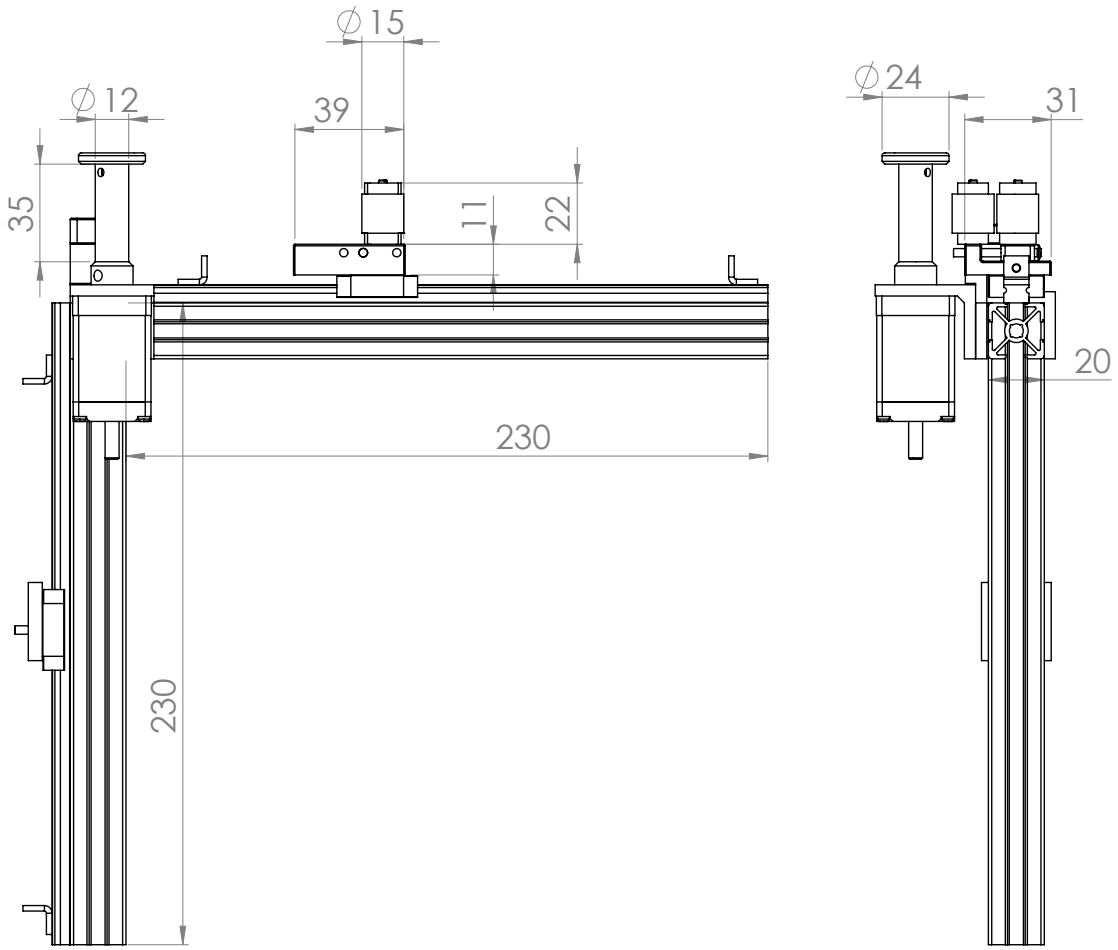

Figure B.1. Dimensions of the 1-DoF experimental setup (mm).

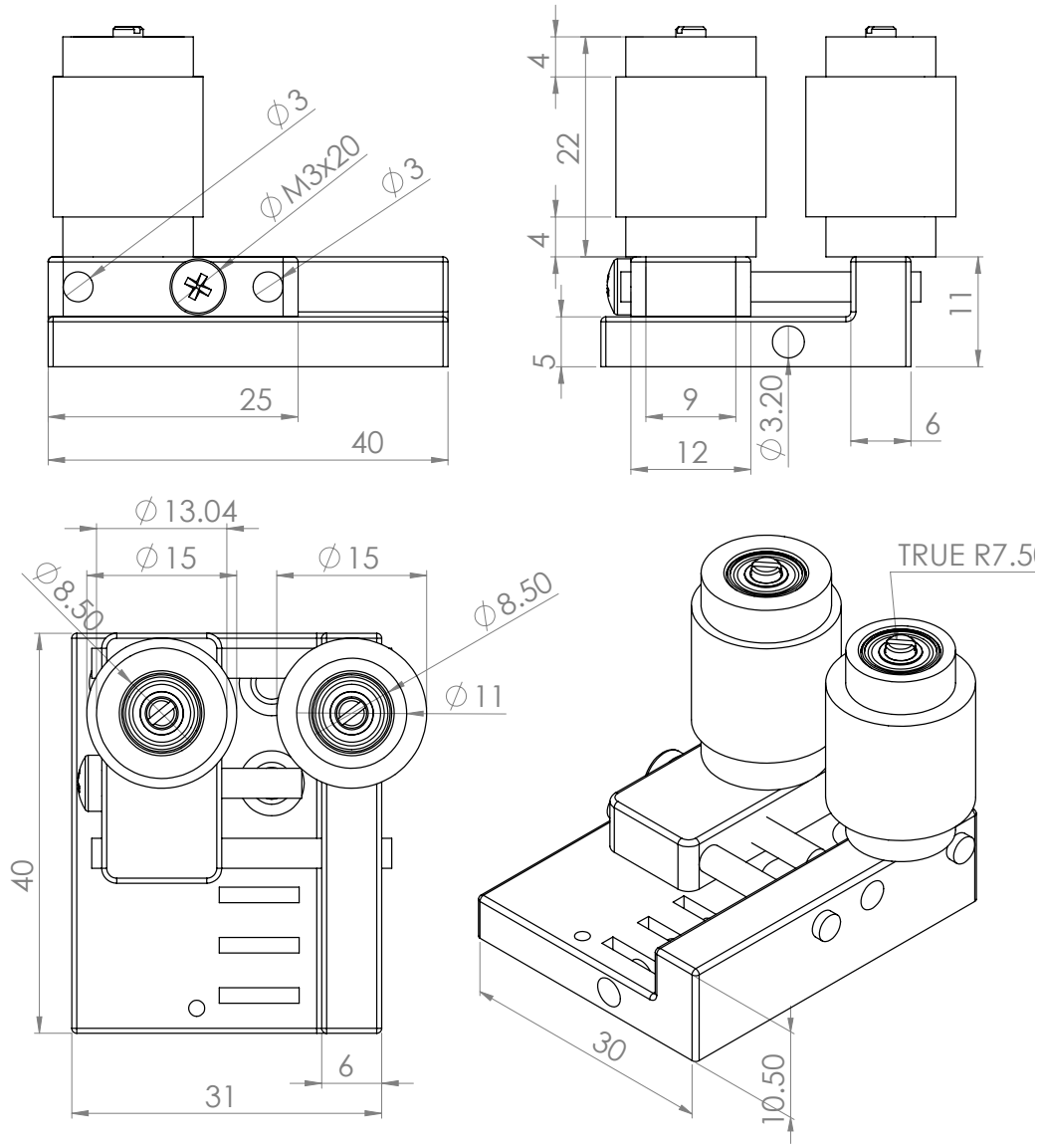

Figure B.2. Technical drawing of the pinch-roller mechanism used for actuator tests (mm).

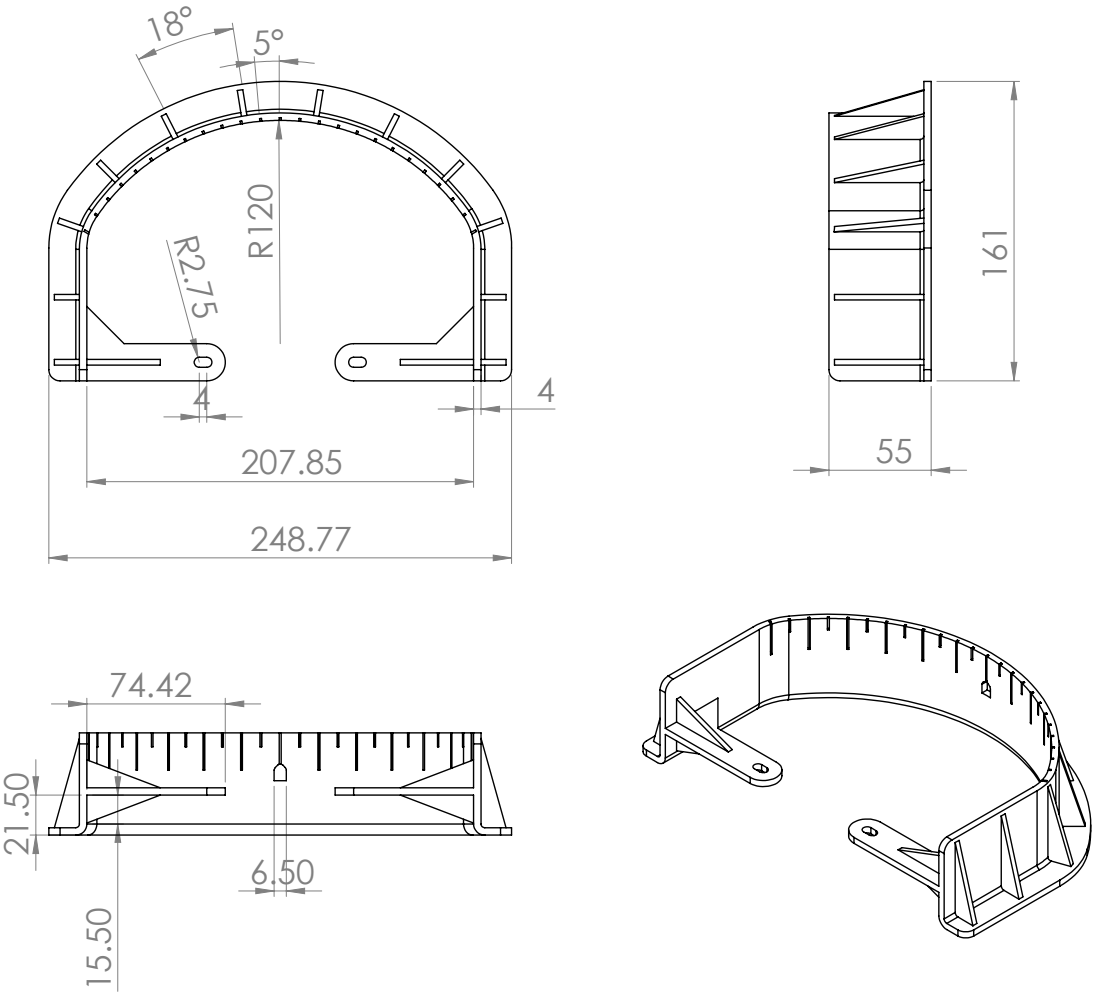

Figure B.3. Dimensions of the 3D printed barrier used to test output force and speed of the preliminary prototype (mm).

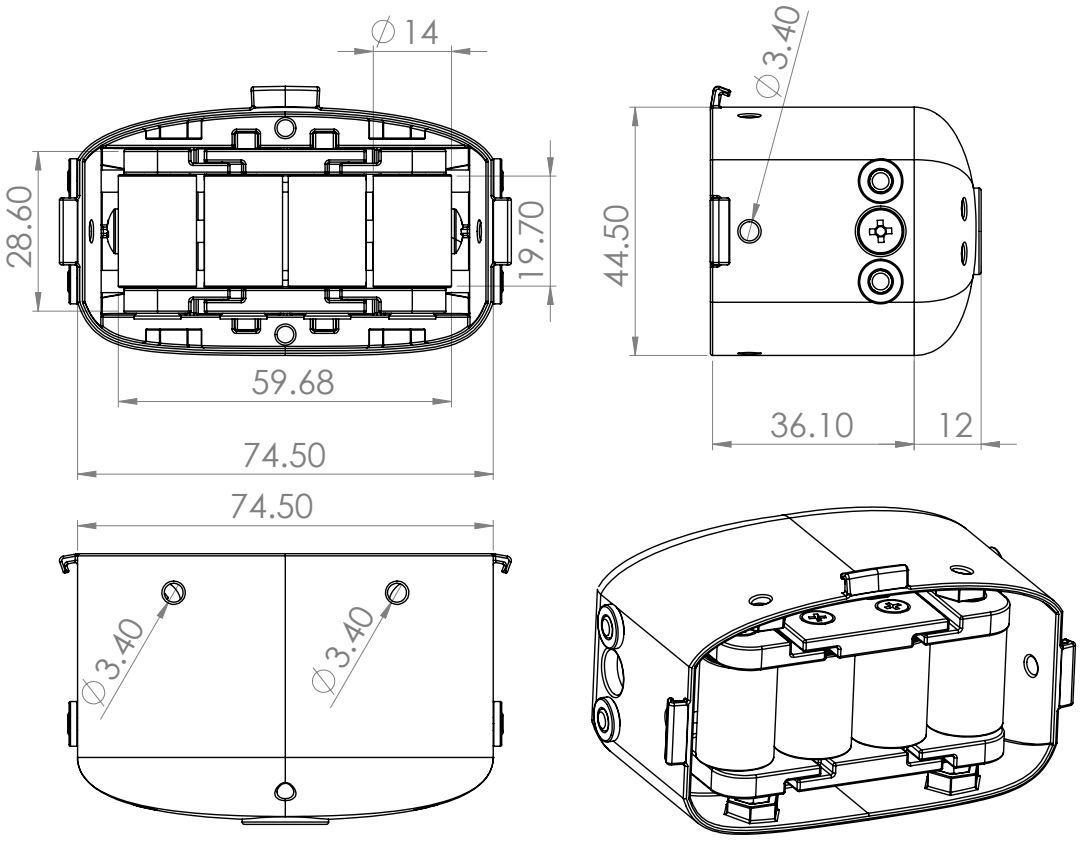

Figure B.4. Technical drawing of the end-effector (mm). Preliminary prototype.

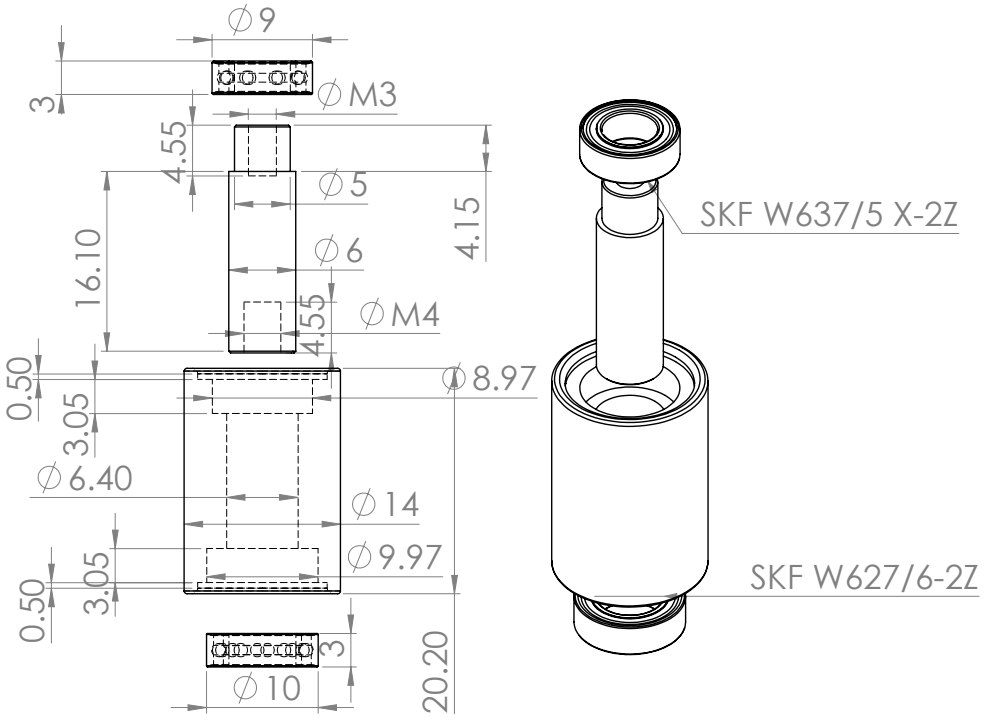

Figure B.5. Technical drawing of the roller assembly (mm). Preliminary prototype.

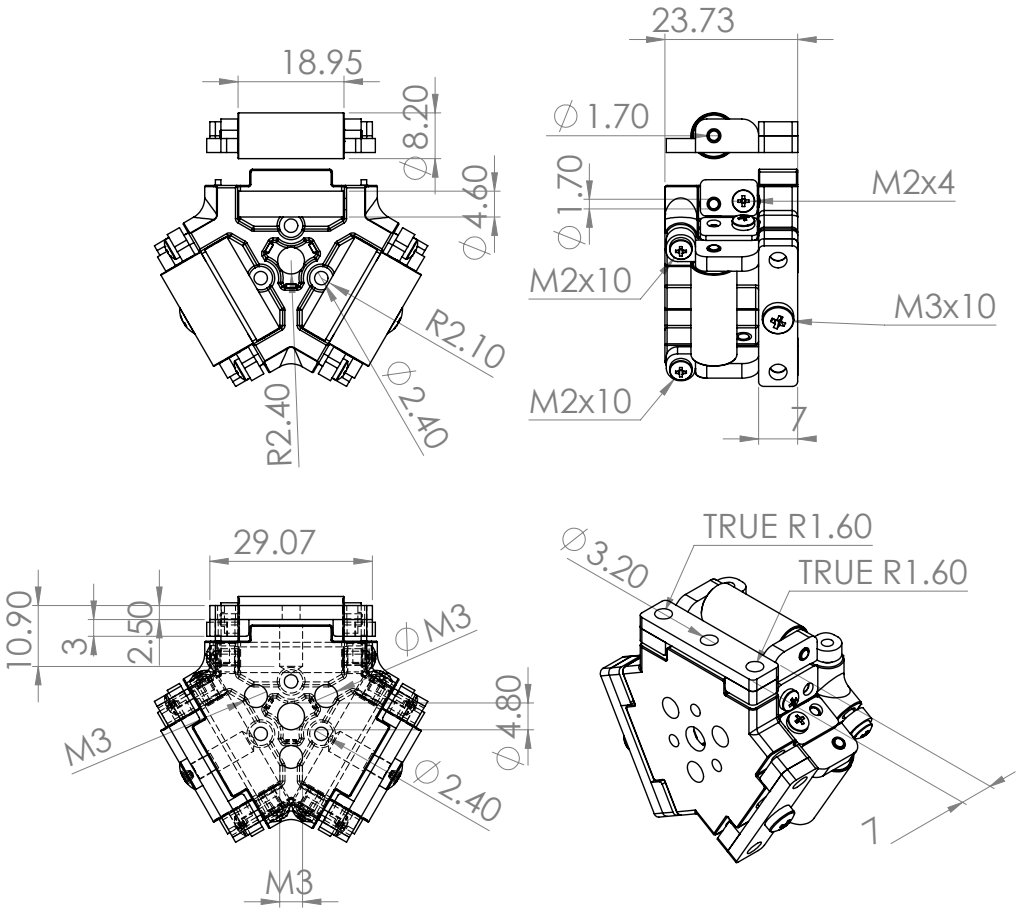

Figure B.6. Dimensions of the end-effector (mm). Final prototype.

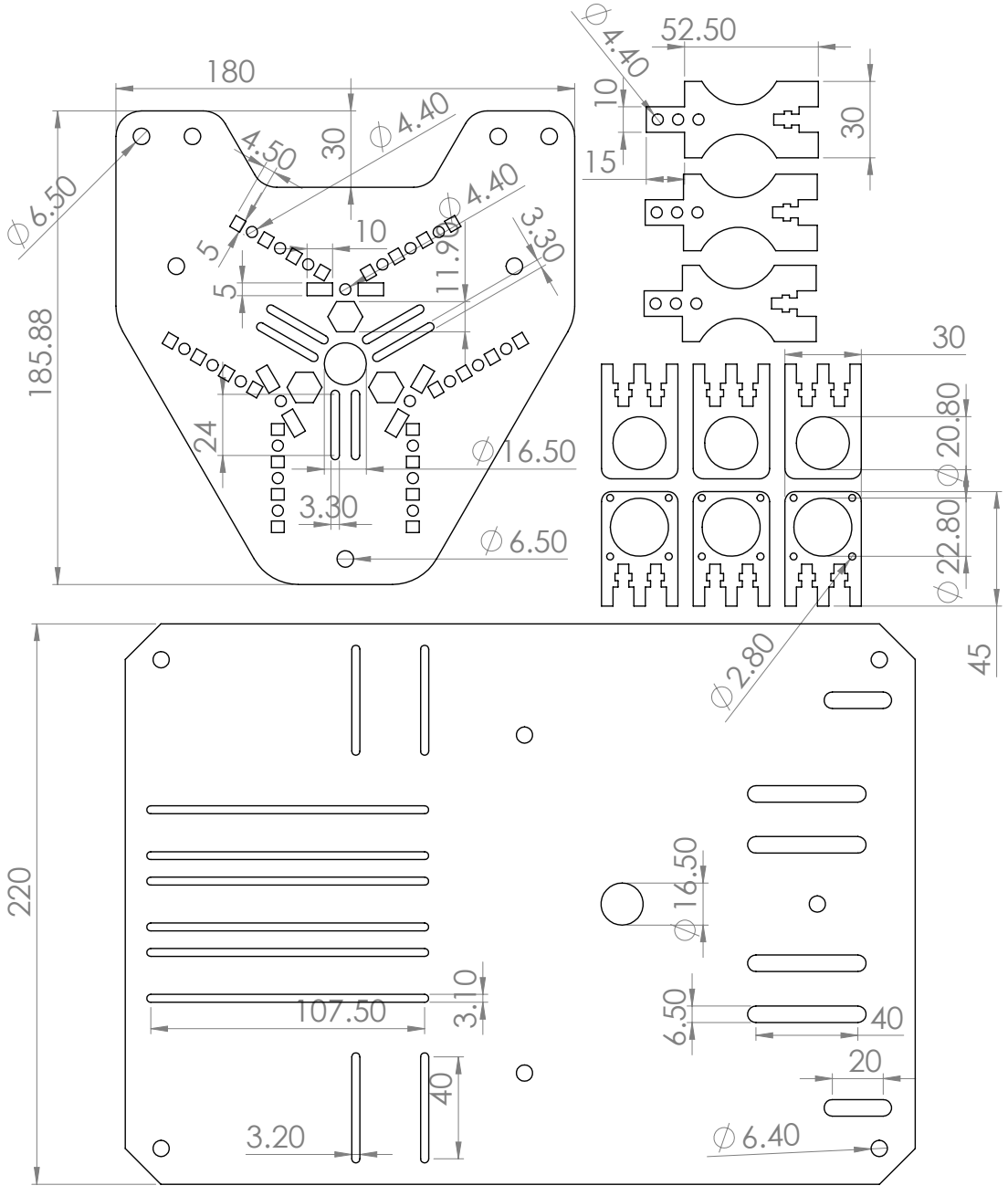

Figure B.7. Dimensions of all laser cut parts in the FU (mm). Final prototype.

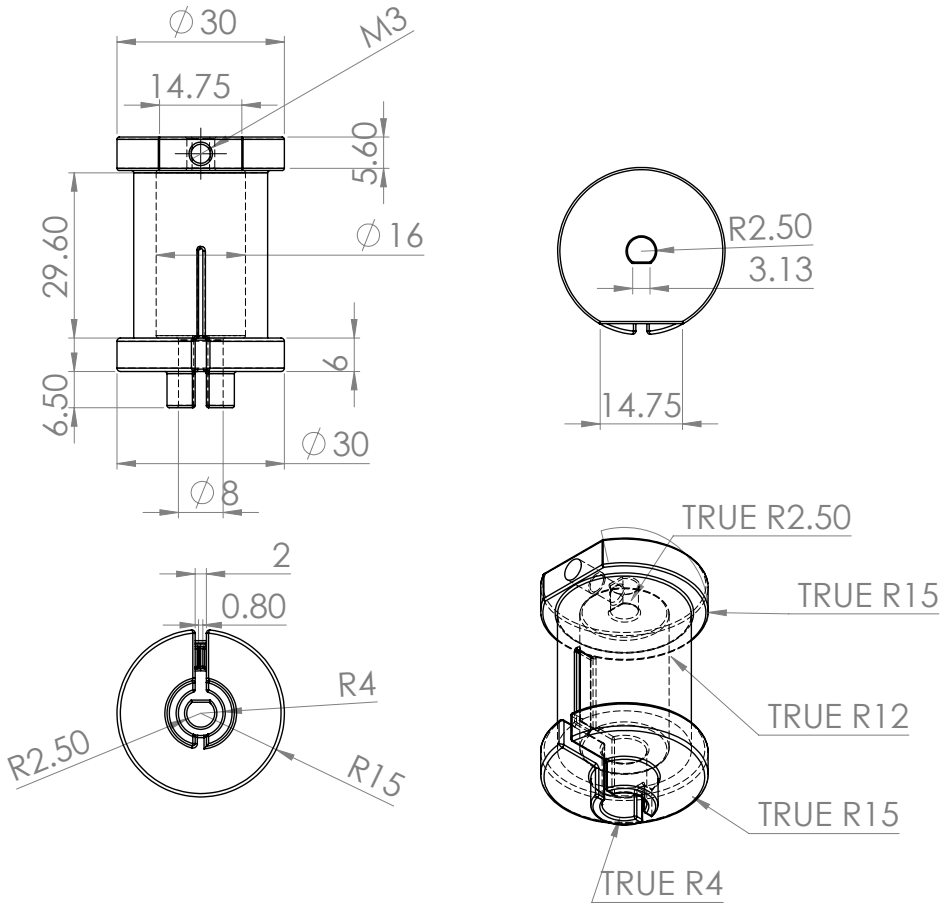

Figure B.8. Technical drawing of the 3D printed spools in the FU (mm). Final prototype.

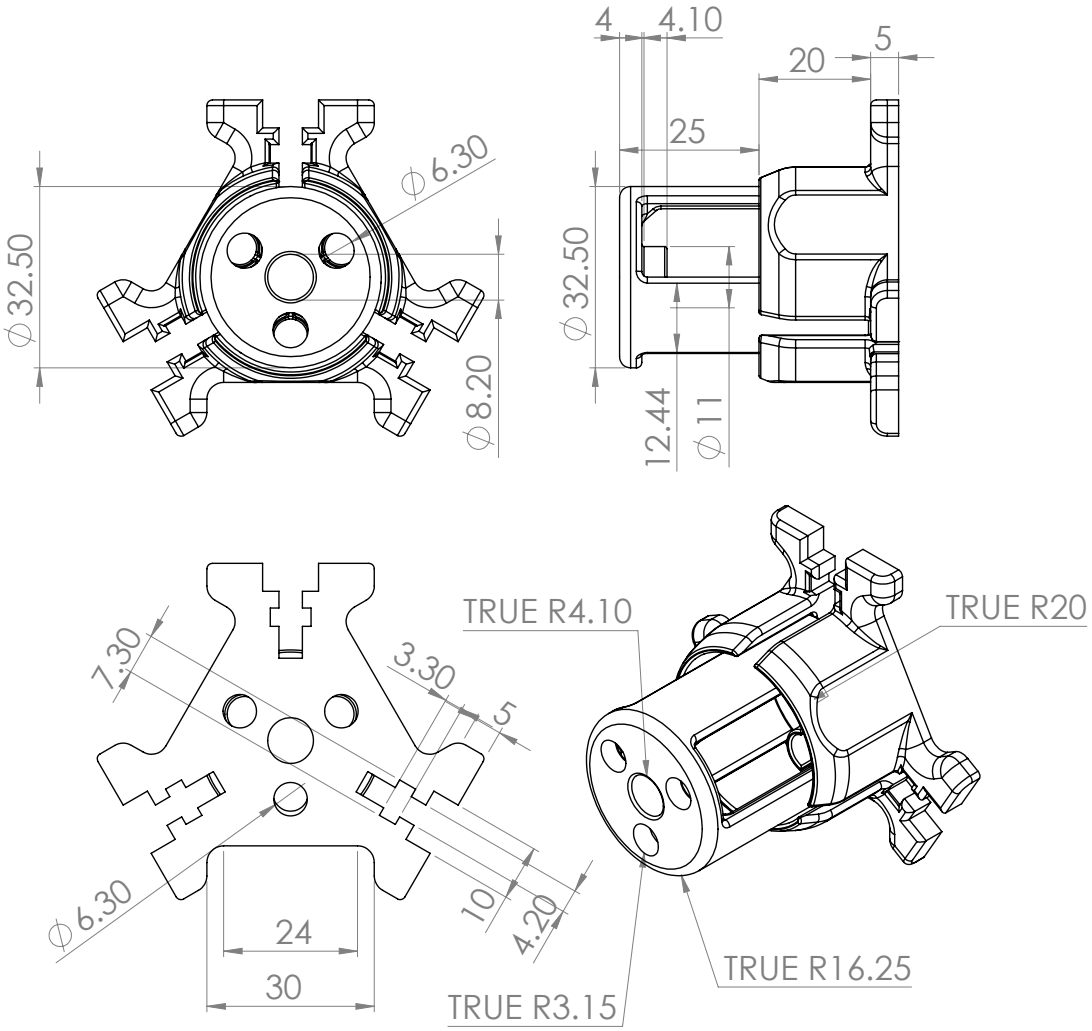

Figure B.9. Technical drawing of the 3D printed inner sheath reservoir in the FU (mm). Final prototype.

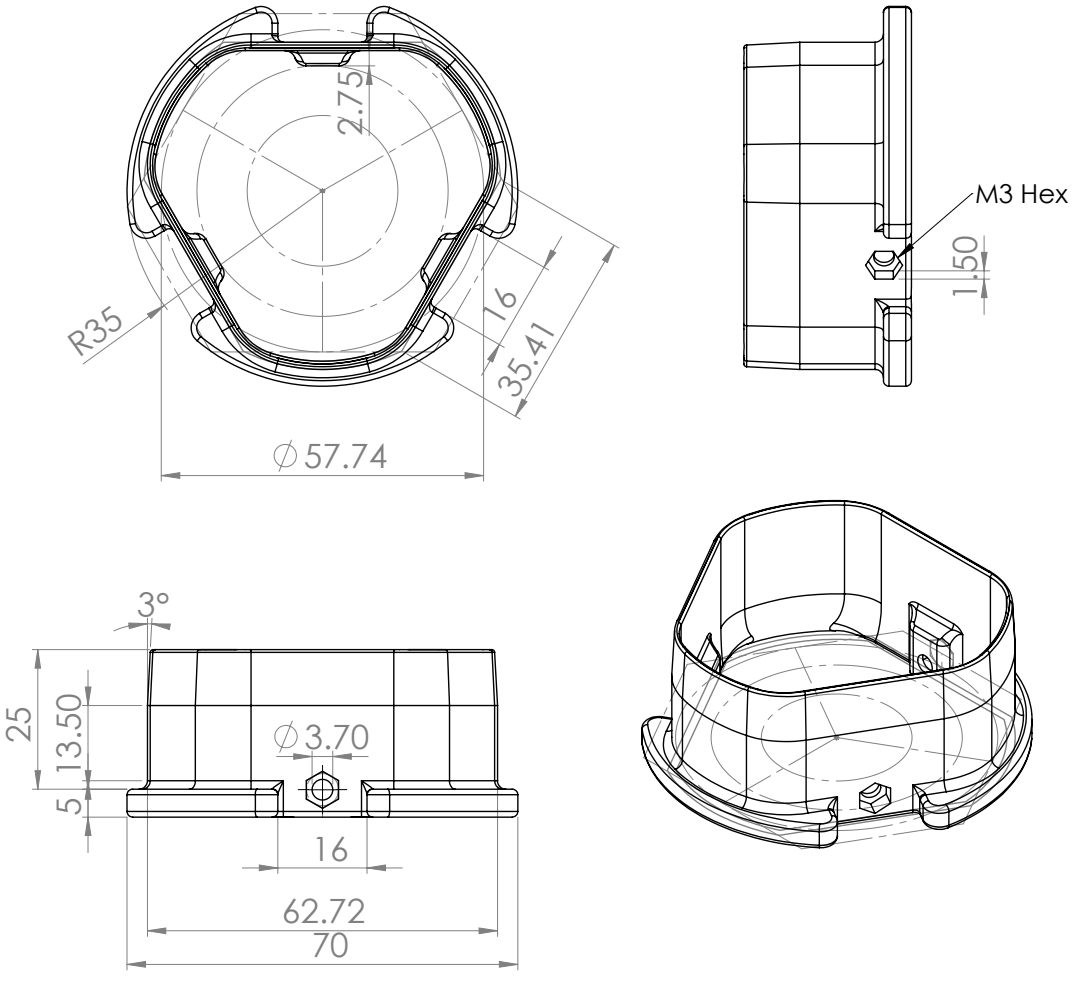

Figure B.10. Technical drawing of the 3D printed outer sheath reservoir in the FU (mm). Final prototype.

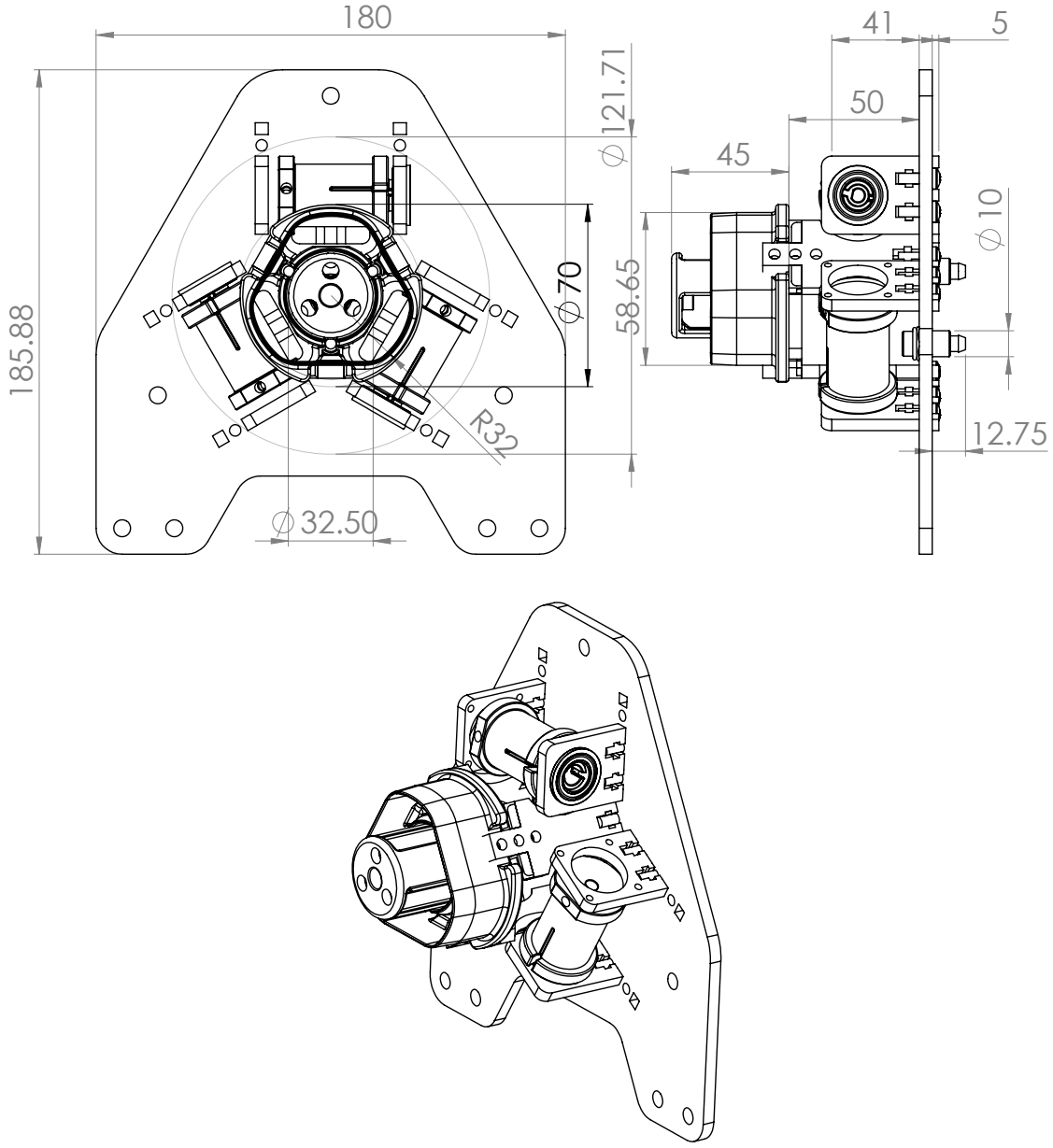

Figure B.11. Dimensions of the assembled FU with all manufactured parts (mm). Final prototype.